40

email: julius.schoop@uky.edu

A Review of Constitutive Models and 1 **Thermal Properties for Nickel-Based** 2 **Superalloys Across Machining-Specific** 3 **Regimes** 4 5 E-Lexus Thornton, first author 6 7 Institute for Sustainable Manufacturing 8 Department of Mechanical & Aerospace Engineering 9 University of Kentucky 10 143 Graham Ave, Lexington KY, 40506 11 email: eth231@uky.edu 12 13 Hamzah Zannoun, second author 14 Institute for Sustainable Manufacturing 15 Department of Mechanical & Aerospace Engineering 16 University of Kentucky 17 143 Graham Ave, Lexington KY, 40506 18 email: hmza222@uky.edu 19 20 Connor Vomero, third author 21 Institute for Sustainable Manufacturing 22 Department of Mechanical & Aerospace Engineering 23 University of Kentucky 24 143 Graham Ave, Lexington KY, 40506 25 email: cmvo225@uky.edu 26 27 **Daniel Caudill, fourth author** 28 Institute for Sustainable Manufacturing 29 Department of Mechanical & Aerospace Engineering 30 University of Kentucky 31 143 Graham Ave, Lexington KY, 40506 32 email: dwca223@uky.edu 33 34 Julius Schoop, fifth author, corresponding author 35 Institute for Sustainable Manufacturing 36 Department of Mechanical & Aerospace Engineering 37 University of Kentucky 38 143 Graham Ave, Lexington KY, 40506

ABSTRACT

41 42

43

44

45

46

47

48

49

50

51

52

53

54

55

56

57

58

59

Nickel-based superalloys (Ni-alloys) are widely used in flight-critical aeroengine components because of their excellent material properties at high temperatures such as yield strength, ductility, and creep resistance. However, these desirable high-temperature properties also make Ni-alloys very difficult to machine. This manuscript provides an overview and benchmarking of various constitutive models to provide the process modeling community with an objective comparison between various calibrated material models to increase the accuracy of process model predictions for machining of Ni-alloys. Various studies involving the Johnson-Cook model and the calibration of its constants in finite element simulations are discussed. It was found that significant discrepancies exist between researchers' approaches to calibrating constitutive models. To this end, various 'physics-based' models are discussed as an alternative to widely used 'phenomenological' models like the Johnson-Cook model, supplemented by a discussion on the more precise inverse method for constitutive model calibration. This manuscript also provides a comprehensive overview of pedigreed physical material properties for a range of Ni-alloys—the variation of thermal properties and thermally induced stresses over machining temperature regimes are modeled for a variety of Ni-alloys. The chemical compositions and applications for a range of relevant Ni-alloys are also explored. Overall, this manuscript identifies the need for more comprehensive analysis and process-specific (e.g., in-situ) characterization of thermomechanical properties for difficult-to-machine Ni-alloys to improve machining performance and aeroengine component quality.

60

61

62

63

64

65

66

1. INTRODUCTION

Nickel-based superalloys (Ni-alloys) such as Inconel 718 are widely used in the aerospace industry because of their exceptional mechanical and physical properties at elevated service temperatures [1]. Many Ni-alloys can operate at temperatures beyond 600 °C, which requires exceptional yield strength (YS) and creep resistance, as well as oxidation and wear resistance properties [2]. One of the most commonly utilized Ni-

alloys, Inconel 718, has great weldability, an exceptional YS of up to 1125 MPa, heat resistance above 1200 °C, etc. [3]. Ni-alloys derive their exceptional properties from their microstructure, which typically features a face-centered cubic (FCC) lattice and a variety of strengthening phases including gamma (γ), gamma prime (γ), and gamma double prime (γ) [4].

The behavior of Ni-alloys has been studied across a broad range of 'service-specific' thermomechanical regimes (i.e., stresses, strain rates, and temperatures representative of the service environment of gas turbine engines). For example, Czyrska-Filemonowicz et al. [5] measured creep, oxidation, and fatigue resistance at various stress and temperature levels to measure the increase in creep strength, oxidation resistance, and thermomechanical fatigue resistance per material. Wang et al. [6] employed similar techniques such as the tensile test to measure strain rates over a wide range of temperatures to understand the behaviors and performance of Ni-alloys under service-specific regimes.

1.1. Summary of Common Ni-alloys

The thermomechanical properties of Ni-alloys are based on their alloying elements (chemical composition) and microstructure [7]. The chemical composition and the effect it has on thermomechanical properties in machining has been researched for several Ni-alloys and the findings are presented in Table 1. The chemical composition of most Ni-alloys is chosen based on their corrosion/creep resistance, strength, and fatigue performance [2, 8]. Mo is added for increasing solid solution strengthening, copper (Cu)

- 88 for increasing thermal conductivity, and Al, Co, W, and Ti for increasing precipitation
- hardness [9]. Al and Cr increase oxidation and creep resistance [9, 10].

Table 1. Overview of common Ni-alloys. Adapted from Thakur and Gangopadhyay [11].

Different grades and corresponding machining operations	Composition [%]	Properties
Inconel 100	Ni 60, Co 15, Cr 10, Al	Precipitation hardenable with a high rupture strength
Turning [12, 13]	5.5, Ti 4.7, Mo 3, C 0.18, Zr 0.06, B 0.014	through 870 °C. The high percentages of Ti, Al, and low refractory metals increase the strength to density ratio.
Inconel 718 Turning [14-20] Milling [21-24] Drilling [25-27] Face turning [28, 29] Broaching [30, 31]	Ni 54.48, Fe 22.3, Cr 17.5, Nb 4.9, Ti 0.96, Al 0.66	Precipitation hardenable, high creep-rupture strength at high temperatures to about 700 °C and excellent strength. Precipitates of primary niobium carbide (NbC), titanium carbide (TiC), disc-shaped gamma double prime (γ "), and needle-like precipitates of δ (Ni ₃ Nb) present.
Inconel 713 LC Drilling [32]	Ni 74.2, Cr 12.6, Mo 4.9, Al 5.7, Nb 1.96, Ti 0.63, Zr 0.1, C 0.047, B 0.007	Good combination of tensile and creep-rupture properties because of gamma-prime strengthening enhanced by solid solution and grain-boundary strengthening. Good castability.
Inconel 825 Turning [33]	Ni 37.1, Fe 32.2, Cr 22.8, Mo 3.24, Cu 2.07, Ti 0.859, C 0.0155	Good resistance to pitting, inter-granular corrosion, chloride-ion stress-corrosion cracking, and general corrosion in a wide range of oxidizing and reducing environments.
Udimet 720 LI Turning [34]	Ni 57.4, Cr 16, Co 15, Ti 5, Mo 3, Al 2.5, W 1, C 0.1	Solid solution strengthened with W and Mo and precipitation-hardened with Ti and Al. High strength, excellent impact strength retention at elevated temperatures, good oxidation and corrosion resistance, and high degree of work hardening.
FGH 95 Milling [35]	Ni 62.5, Cr 12.98, Co 8.00, Nb 3.5, Al 3.48, Mo 3.4, W 3.4, Ti 2.55, C 0.060, B 0.012	Precipitation-hardened with a higher tensile and YS at 650 °C. Compact structure after hot isostatic pressing consisting of coarse gamma prime phase (γ') precipitated along previous particle boundaries (PPB) appear in the grain.
ME-16 Turning [36]	Ni 56.3, Co 20.5, Cr 10.4, Al 3.1, W 3, Ti 2.6, Ta 1.4, Nb 1.4, Mo 1.3	Good strength and creep resistance at high temperatures (600-800 °C). Good resistance to fatigue crack initiation at lower temperatures (300-600 °C). Can maintain strength and lower density at elevated temperatures.

RR 1000	Ni 52.4, Co 18.5, Cr	Solid solution strengthened with Co, Cr, and Mo. Good
Turning [37]	15, Mo 5, Ti 3.6, Al 3,	strength, toughness, creep resistance, oxidation
Milling [38]	Ta 2, Hf 0.5, C 0.03	resistance, and corrosion resistance at high
Drilling [39, 40]		temperatures.
Reaming [41]		
Broaching [42]		
Nimonic 75	Ni 80.5, Cr 19.5	Good corrosion and heat resistance, high-temperature
Turning [32]		strength and outstanding oxidation-resistance.
Nimonic 80A	Ni 76, Cr 19.5, Ti 2.4,	Age-hardenable creep-resistant alloy for service at
Turning [43]	Al 1.4	temperatures up to ~815 °C.
Nimonic 105	Ni 54, Co 20, Cr 15,	Age-hardenable superalloy with increased Al for
Turning [44]	Mo 5, Al 4.7, Ti 1.3	improved oxidation-resistance and strength, and high
		creep-rupture properties up to ~950 °C. Strengthened
		by additions of Al, Mo, and Ti.
Nimonic C-263	Ni 51, Co 20, Cr 20,	Readily weldable, age-hardenable superalloy with
Turning [45]	Mo 5.8, Ti 2.2, Al 0.5	excellent strength, ductility, and corrosion resistance
Milling [46]		up to ~850 °C. Solid-solution strengthened by Mo.
Hastelloy C-2000	Ni 47, Cr 22, Fe 18,	Localized corrosion resistance, good resistance to hot
Milling [47]	Mo 9, Co 1.5, W 0.6	acids and excellent resistance to stress-corrosion
		cracking.
Haynes 282	Ni 57, Cr 20, Co 10,	γ' precipitation strengthened Ni-alloy with excellent
Twist drill [48]	Mo 8.5, Ti 2.1, Al 1.5,	creep properties, fabricability and thermal stability.
Milling [49]	Fe 1.5, Mn 0.3, Si	
	0.15, C 0.06, B 0.005	
Waspaloy	Ni 57.59, Cr 19.4, Co	Precipitates of NbC and TiC and γ'/γ" phases cause
Turning [50, 51]	13.2, Fe 1.2, C 0.03,	precipitation hardening, adhesion, and extreme heat
	Mo 4.1, Al 1.3, Ti 3.1,	generation. There are also significantly less carbides
	Nb ~0, B 0.005, Mn	present in Waspaloy than in Inconel 718, resulting in
	0.03, Si 0.05	less tool-wear during turning.
Alvac 718+ [52]	Ni 52.07, Cr 18, Co	Low Fe and higher Al, W, and Co content yields better
Broaching [53]	9.1, 2.7 Mo, W 1, Nb	high temperature properties. Has higher hardness than
Milling [53]	5.4, Al 1.45, Ti 0.75,	Inconel and exhibits less thermal softening during
	Fe 9.5, C 0.02, P	machining.
_	0.006, B 0.005	

Increasing the percentage of an alloying element such as Ti and/or Al during material processing (e.g., from molten until cooling, aging, and heat treatment) allows for the alloy to enter the γ , γ' , and γ'' phases where the strength increases with each phase [4]. The γ phase, also known as the alloy matrix, is an FCC austenitic phase that is based in nickel. Ni-alloys also contain significant percentages of other elements such as tungsten, Co, Cr, and molybdenum (Mo) [54, 55].

The γ' phase contains Ti and Al within the precipitate and exhibits increased strength at high temperatures and creep resistance over the γ phase [54, 55]. Additionally, the γ' phase develops a film at the grain boundary under heat treatments that improves rupture properties [54-56]. Due to the excellent strengthening properties at higher temperatures, greater amounts of γ' were added to superalloys over time, with earlier alloys containing 25% by volume and more modern superalloys containing up to 45% [54, 57].

The γ' and γ'' phases precipitate with each other in some alloys such as Inconel 718, from iron acting as a catalyst for the formation of γ'' [54]. Compared to the γ' phase, the γ'' phase does increase the strength of these alloys at lower temperatures but γ'' rapidly loses strength at temperatures above 650 °C [54]. The γ'' phase has a combination of Ni and niobium (Nb) and has good strength at lower temperatures but has less strength at higher temperatures above 650 °C [56]. This phase still sees use in high temperature turbines that take advantage of excellent lower temperature properties due to transpiration cooling [58]. The dislocation generation of γ , γ' , and γ'' precipitates during plastic deformation is what causes the material to continue to strengthen at room temperature (RT) [4].

Davies and Stoloff [59] studied these phases and how dislocation-precipitate interactions affect flow stress in a Ni-based superalloy. They showed that the size of the γ' grains as well as dislocations caused by aging and heat treatment have a strong effect on the YS of the alloy, particularly at elevated temperatures. Ni-alloys have properties that allow them to continue to increase their YS as temperature increases—there can be

continual increases in YS until 800 °C for most of these superalloys [60]. However, the YS sharply decreases at temperatures above 800 °C, where it is only a fraction of the peak YS when the temperature reaches 1200 °C [60]. Piearcey et al. [61] found that the γ ' phase continued to increase the strength of Mar-M200 alloy as temperatures increased, highlighting the strong influence of this phase on high temperature properties.

1.2. Applications of Ni-alloys in Jet Engines

Jet engines are extremely sophisticated pieces of equipment whose components require specific tolerances, complex geometries, and special materials. Materials used should be lightweight yet sufficiently strong to resist the significant forces and temperatures encountered at high altitudes; these come in the form of superalloy metals. Figure 1 is a schematic of the major components of a jet engine.

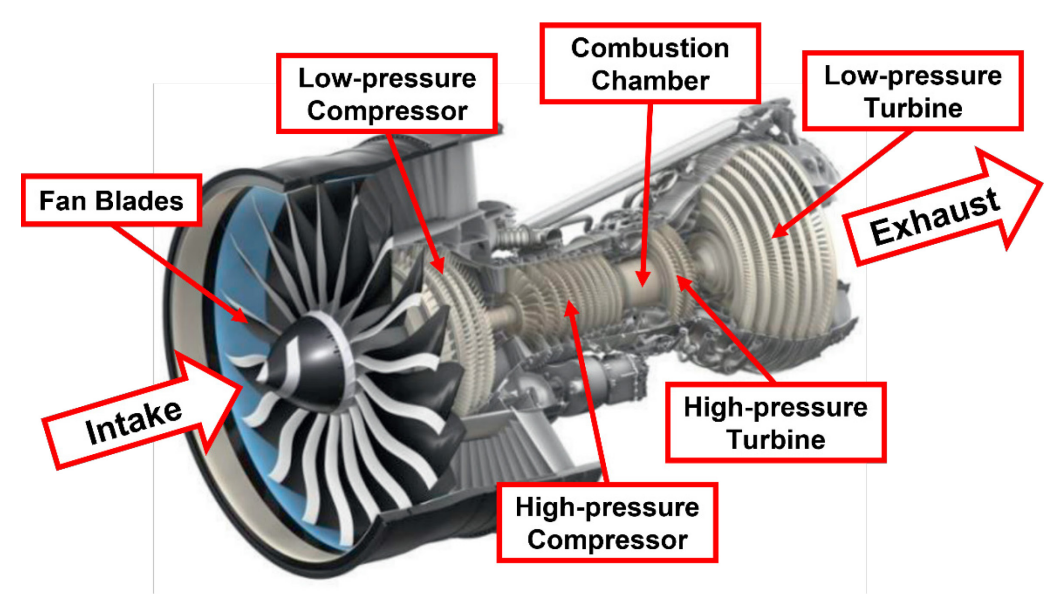


Fig. 1. Major components of a jet engine. Adapted from Eickemeyer et al. [62].

As can be seen in Fig. 1, the cold section is where frigid air enters—the fan sucks air in towards the hot section where it is compressed through the low and high-pressure

136

137

138

139

140

141

142

143

144

145

146

147

148

149

150

151

152

153

154

155

156

compressors. It is then funneled into the combustion chamber where it combusts with fuel. Lastly, the heated air is expanded and discharged via the high and low-pressure turbines: the hot air turns the turbine blades, where it is pushed out the exhaust nozzle, generating thrust that propels the aircraft. The components for these different sections are constructed from high-grade, durable metals. The fan blades are typically made of several materials including aluminum (AI), titanium (Ti), and stainless steel. The compressor is typically made of nickel (Ni), cobalt (Co), or iron (Fe) alloys, with Al, Ti, and chromium (Cr) as additives. The combustion chamber can reach temperatures above 1900 °C, which is above the melting point of most materials [63]. Thus, the properties of materials in this section are especially crucial. Commonly used metals include tungsten (W), molybdenum silicide, niobium silicide, and carbon silicide [64]. High-pressure turbine components will generally be made of nickel-based superalloys and the low-pressure turbine is usually made of iron-based superalloys, stainless steel, or titanium alloys. The exhaust nozzle is commonly comprised of Inconel alloys and stainless steel [65]. Lightweight materials such as Al are used for the shell.

Before a Ni-alloy component goes into service, it must be machined to the desired geometry and surface integrity [66]. Ever since early pioneering work by Kahles and Field [67] dealing with the impact of surface integrity characteristics like residual stress and surface roughness on the performance of Ni-alloy components, a wide range of studies have further established that machining-induced near-surface damage can lead to premature component failure with potentially catastrophic consequences [68-70].

Tool and workpiece geometry play a key role in the development of machining-induced surface integrity and fatigue performance. The high strength of Ni-alloys results in poor machinability due to high cutting forces, temperatures, and rapid tool wear, which in turn presents poor surface integrity such as deformed grains and tensile residual stresses [55, 71-73]. The machining of Ni-alloys has been widely researched, with most studies being empirical and describing relationships between process parameters ('feeds and speeds') and the resulting performance metrics (e.g., cutting forces [2, 74, 75], tool-life [76], surface integrity [77], etc.).

1.3. Scope of Manuscript

Modeling approaches are widely employed to predict the response of workpiece materials to thermomechanical loads during machining. Constitutive models that predict thermomechanical responses such as the Johnson-Cook (JC) model [78] return results for variables such as the flow stress. Modern process modeling is typically carried out with the help of software such as MATLAB, using finite element (FE) software, or physics-based analytical models [79, 80]. This study is primarily concerned with the use of constitutive models in FE simulations, where the validation of the numerical results from FE simulations for the prediction of material behavior during machining is one of the biggest hurdles in the research field of manufacturing [81].

Modeling of machining processes with numerical simulations is difficult because it requires inputs of process-specific constitutive and friction response [79, 82], neither of which are well understood. Melkote et al. [79] explained that the flow stress of the temperature at the tool-chip interface is overestimated by models due to the inability of

180

181

182

183

184

185

186

187

188

189

190

191

192

193

194

195

196

197

198

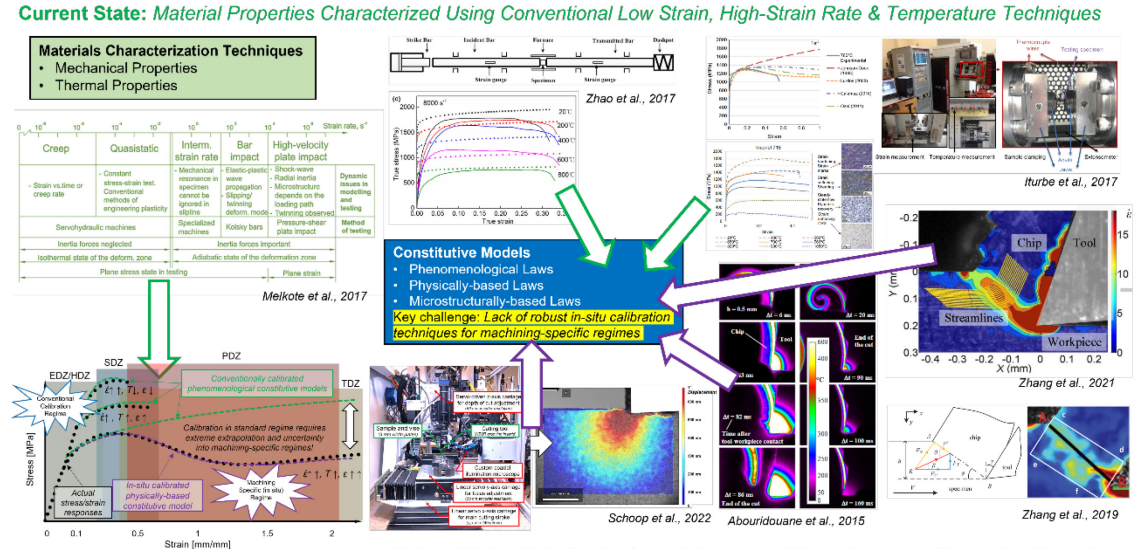
199

200

dynamic mechanical tests to replicate the higher strains and temperature in the shear zone. Astakhov et al. [83] compared friction data from orthogonal tests with numerical modeling and there was a discrepancy of 50-100% for the friction coefficient. Industry models like this are unreliable because they are not 'physics-based', of which there is a large demand [84]. A physics-based model is founded on 'first principles' such as activation energies, fundamental constants, and physics-based variables. This stands in contrast of phenomenological models, which model specific phenomena (e.g., strain hardening, thermal softening) by including a set of functions and constants that are calibrated through empirical trials and curve fitting techniques. Liu et al. [85] give a good explanation on the difference between the two types of constitutive models. They state that phenomenological models use functions that incorporate the strains, strain rates, and temperatures but neglect physics at the microscale (i.e., microstructural effects). Physics-based models do account for these microscale physics, using characteristics like dislocation density, twinning, and phase transformations for computing the flow stress [85, 86].

A fundamental problem limiting the adoption of physics-based models is that the behavior of materials in extreme regimes is unknown and cannot be accurately predicted without significant extrapolation [79]. This is problematic because predictions determine the machining parameters, which ultimately dictate component quality [87]. Furthermore, there are issues with the current standard of calibrating the material constants in constitutive models with mechanical tests, which are not representative of machining conditions [81]. Thus, there is a need for direct measurement of calibration

data via orthogonal machining tests, which will also be discussed later in this manuscript. Fig. 2 summarizes the current and future state of constitutive modeling and serves as a graphical abstract for this manuscript.



Future State: High Strain Material Response Characterized In-Situ Under Machining Specific Thermomechanical Regimes for More Physics-Based Modeling

Fig. 2. Current and future state of constitutive modeling for machining processes. Compiled figures from [79, 88-93].

Accurate model predictions require thorough analysis and characterization of the way material properties change due to the thermomechanical loads of machining process and their effect on defects [79, 87]. A recent review [84] shows that considerable progress has been made toward the development of constitutive models, but there remain several key shortcomings, namely the response of metals under the extreme stress, strain, and temperature gradients. While 'handbook' data exists for many alloys [54, 56, 94], there is currently no comprehensive resource for constitutive model parameters and physical properties of common Ni-alloys. Thus, academia and industry continue to use an empirical approach that is time and cost intensive.

218

219

220

221

222

223

224

225

226

227

228

229

230

231

232

233

234

235

236

237

238

reviewing suitable constitutive models and calibration regimes used in literature as well as characterizing the behavior of material properties under increasing temperature. While much effort has been focused on the constitutive response of Ni-alloys, little work has addressed the impact of physical properties (density, thermal conductivity, emissivity, etc.), which are essential to understanding the behavior of the material. Material properties, both physical and mechanical, are often co-dependent on each other. For instance, increasing ductility will cause a decrease in strength; increasing thermal conductivity will cause an increase in thermal diffusivity. Modeling then becomes important because it uses this knowledge of physical property behaviors to predict the performance of materials in an array of service settings. Without knowledge of physical property behaviors, it would not be possible to comprehend how the material performs in different regimes. Many studies treat these properties as either constant [95-97] or not mutually interconnected, when literature clearly shows that they are temperature sensitive [98-100]. Since physical properties have a direct influence on mechanical properties, this manuscript aims to explore the effect of temperature on said physical properties.

2. OVERVIEW OF CONSTITUTIVE MODELING

This section introduces the two most used constitutive models (Johnson-Cook and Zerilli-Armstrong), as well as some of the notable modified versions of the Johnson-Cook model. The key differences between the Johnson-Cook and Zerilli-Armstrong models are discussed, as well as modeling efforts using other models like the Mechanical Threshold Stress. Notably, this section addresses the lacking availability of

calibration techniques for material constants, as well as the influence and importance of constitutive model selection in FE simulations.

2.1. Summary of Common Constitutive Models

Constitutive models serve the purpose of predicting the constitutive behavior of ductile materials. According to Zhang et al. [101], they "describe the material responses to the different mechanical and/or thermal loading conditions, which provide the stress-strain relations to formulate the governing equations, together with the conservation laws and kinematic relations." The most widely used constitutive model is the JC model because of its simplistic nature [78, 102]. The basic form of the JC model is shown below:

$$\sigma = [A + B\varepsilon^n] \left[1 + C \ln \left(\frac{\varepsilon}{\varepsilon_0} \right) \right] \left[1 - \left(\frac{T - T_0}{T_m - T_0} \right)^m \right] \tag{1}$$

where σ is the equivalent von Mises flow stress, ε^n is the equivalent plastic strain, $\dot{\varepsilon}$ is the plastic strain rate, $\dot{\varepsilon}_0$ is the reference plastic strain rate, T is the absolute temperature, T_0 is the RT, T_m is the absolute melting temperature, and T_0 , and T_0 are material constants that are unique to each model [78]. Each set of brackets utilizes various parameters: the first set considers stress as it relates to strain, the second set considers the strain rates of the material, and the third set considers the temperature of the material [78]. The material constants translate as follows: T_0 represents yield stress, T_0 and T_0 represent strain hardening, and T_0 represents the strain rate effect. These constants can be identified through isothermal tension or torsion tests [78]. The final

constant, *m*, represents the thermal softening effect and is found through averaging the
 data previously found in the tension or torsion tests [78].

Since the basic version of the JC model is purely phenomenological, many authors have modified it to account for microstructural effects which are known to have a major effect on the behavior of the flow stress [103-106]. Calamaz et al. [103] were the first to introduce a modified JC (MJC) model that accounts for flow softening at high strains due to dynamic recovery (DRV) and dynamic recrystallization (DRX) by the addition of the hyperbolic tangent function, which is strain and temperature dependent. This MJC is given below [79]:

$$\sigma = \left[A + \frac{B\varepsilon^n}{\exp(\varepsilon^a)} \right] \left[1 + C \frac{\dot{\varepsilon}}{\dot{\varepsilon}_0} \right] \left[1 - \left(\frac{T - T_0}{T_m - T_0} \right)^m \right] h(\varepsilon_p, T)$$
 (2)

$$h(\varepsilon_p, T) = D + (1 - D) \tanh[(\varepsilon_p + S)^{-c}]$$
 (3)

$$D = 1 - \left(\frac{T}{T_m}\right)^d \tag{4}$$

$$S = \left(\frac{T}{T_m}\right)^b \tag{5}$$

where a, b, c, and d are additional material constants and $\sigma, \varepsilon^n, \dot{\varepsilon}, \dot{\varepsilon}_0, T, T_0$, and T_m are the same as in equation 1 and can be determined empirically [102]. Rotella and Umbrello [104] also developed a MJC using the hyperbolic tangent function to account for flow softening, but their model also calculates the initial YS based on the lamella thickness. The MJC by Denguir et al. [105] utilizes an additional term to account for DRV and DRX, but they also incorporate the stress triaxiality (ratio between the hydrostatic stress and the von Mises stress) to reflect the influence of hydrostatic pressure on grain

dislocations [107]. In addition to the stress triaxiality, Cheng et al. [106] added the Lode angle to their MJC to describe the state of stress at the microscale [85].

While both the basic JC and MJC models are widely used, there is a tradeoff between them. The basic JC is simple to calibrate, but MJC models are much more difficult to calibrate because of the added variables. The addition of the hyperbolic tangent function (equation 3), for example, accounts for the strain softening of the material and also allows for second-order interactions [103], neither of which are possible in the basic version. The biggest problem with the basic JC is that it has often been shown to be inaccurate at higher strain rates (> 10^3 s^{-1}) [79].

The second most widely used constitutive model is the Zerilli-Armstrong (ZA) model. Like the JC, it has a simpler form based off assumptions for summations of thermal and non-thermal stresses [84] which has worked well for materials such as AISI 1045 steel [108] and some carbon steels [109]. Alongside the JC, the ZA has successfully been used to model the flow stress of materials; Lin et al. [110] used the JC and ZA models in tandem to model strain rate and temperature with respect to the deformation of high strength steels, which revealed how these coupled effects interact. This breakthrough led to both models becoming commonplace. The ZA model consists of smaller equations with few variables, so it is simple to use and calibrate. It uses strain rate and temperature to analyze how thermal effects influence the flow stress, and it also accommodates second-order interactions. Although unlike the JC models, the ZA models implicitly account for the material's microstructure and its effect on flow stress [111]. However, the ZA model has its shortcomings; the biggest being that it does not

consider material softening under large strains or temperatures [79]. The ZA model will be discussed further in Section 4.1.

Besides the JC and ZA, there are numerous other models for predicting the response of metals to cutting operations. Regarding phenomenological models, this manuscript will focus on the JC, as it is by far the most widely used for FE simulations and can be readily benchmarked because of the quantity of works on it. However, numerous notable physics-based models will be discussed in Section 4.1. Other more niche models will not be discussed in detail in the present work, but other authors have already compared the JC and ZA with such models.

Bobbili et al. [112] studied Ti-alloy IMI 834 at various strain rates with ballistic tests to understand material behavior under varying strain rates, temperatures, and stress triaxialities. They compared the basic JC, basic ZA, and Cowper-Symonds (CS) models. All were in good agreement with experimental results, but the JC was most accurate. Kotkunde et al. [113] investigated how strain, strain rate, and temperature affect flow behavior of Ti-6Al-4V. The models used were the basic JC, Khan-Huang-Liang, Fields-Backofen, and Mechanical Threshold Stress (MTS)—all models gave satisfactory results, but the MTS was preferred because it is physics-based (the MTS model will be discussed in detail in Section 4.1). On the same material, Kotkunde et al. [114] later used a variety of hardening models (basic JC, modified Zerilli-Armstrong (MZA), and modified Arrhenius) when looking at principal strain limits for forming limit diagrams, and the modified Arrhenius model showed the best results.

 Melkote et al. [84] reviewed several popular models such as the JC, ZA, Strain Path Dependance, Power Viscosity Law, Bammann-Chiesa-Johnson, and MTS for pure titanium. They concluded that there is a need for a testing technique for determining which model is most suitable for a specific material—this could be used to create a comprehensive database to assist in selecting the most appropriate model for a given alloy. Indeed, the present work identifies using the machining process as its own material characterization technique, e.g., using in-situ techniques, as key for more reliable constitutive models. They also call for the development of new fracturing models. Liu et al. [85] present an excellent timeline for the evolution of constitutive models, both phenomenological and physics-based, over the decades. Notably, they identify the ZA model as phenomenological, while others have characterized ZA as physics-based due to consideration of microstructure and second order interactions [79].

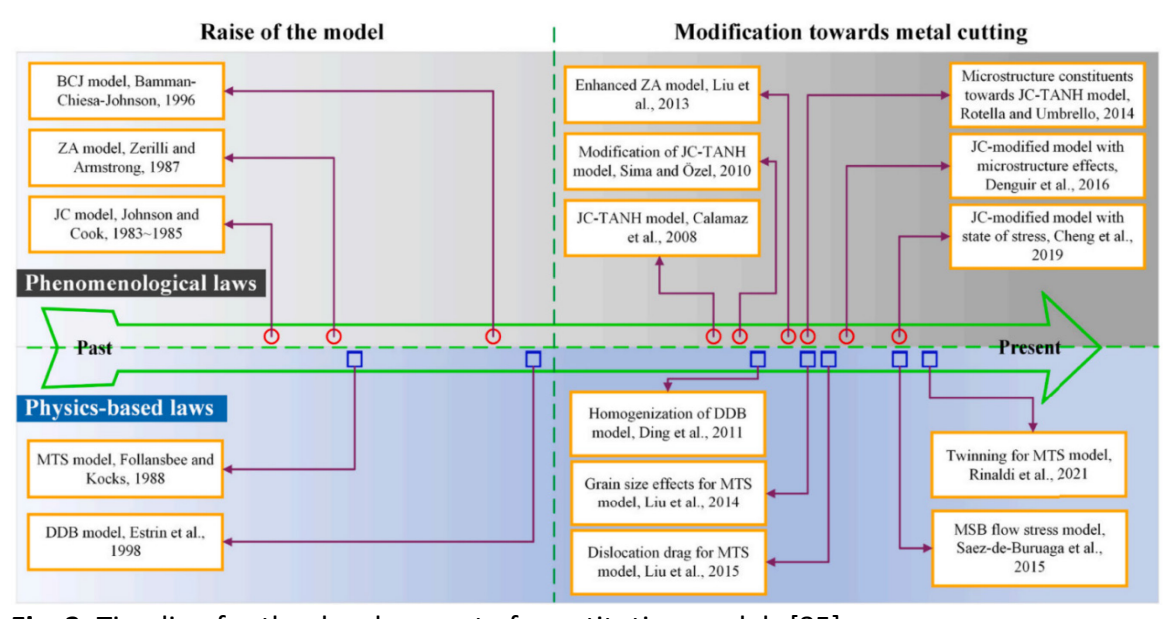


Fig. 3. Timeline for the development of constitutive models [85]

While more complicated models can prove to be preferable to the JC or ZA in certain circumstances, the JC and ZA are consistently agreeable under a wide variety of machining conditions. Thus, it is difficult to make broad assessments about the suitability of a particular constitutive model for a specific machining operation. It is therefore of chief importance to ensure that a chosen model is well-calibrated for the material and machining operation [84].

Both phenomenological (e.g., JC and its variants) and physics-based (e.g., ZA, MTS, etc.) constitutive models are fundamentally limited in their predictive abilities based on the availability of high strain rate, large strain, and high temperature stress/strain calibration data. This results in inaccurate models at higher strain rates that are not useful for metal cutting [89, 91]. The thermomechanical regimes of machining differ from that of conventional materials characterization techniques, including high strain rate techniques such as the Split-Hopkinson Pressure Bar (SHPB) test and similar mechanical tests. Strains in machining may be on the order of 10, while most ductile metals will fail at strains on the order of 10^{-1} when subjected to high strain rate tensile, compression, or shear testing. This order of magnitude of differences clearly indicates the state of triaxial stress and path history of metals being deformed during cutting differs significantly from that of more simplified geometries.

Based on the limitations of conventional high strain rate materials characterization techniques, the authors of the present work propose that the most effective means for characterizing the constitutive behavior of materials during machining-specific thermomechanical regimes must be the cutting process itself. This is

by no means a novel insight or proposal, as the origins of this approach can be traced back to early work by Oxley [115, 116] and many other researchers since. More recently, the availability of ultra-high speed in-situ optical and thermal techniques has enabled more efficient analysis of strain, strain rate, and temperatures during cutting. A recent in-situ characterization and inverse constitutive material property identification study by Zhang et al. [92] concisely summarizes the challenges and motivation for such efforts: "A direct measurement of the strain and strain rate in metal cutting and thus describe the material behavior remains still a challenge. This paper is motivated by the requirements to provide the material constitutive models for metal cutting process, in which the strain may reach 1–2 and the strain rate up to 10⁵ s⁻¹. Unfortunately, this task cannot be fulfilled by the conventional SHPB tests, because the strain and strain rates covered by SHPB are lower to those usually found in metal cutting process." Further discussion of the use of in-situ methods for model calibration is provided in Section 4.2.

2.2. Influence of Constitutive Model Selection on Output Values

Tool-chip interface parameters like contact pressure, friction coefficient, and thermal resistance are simultaneously being influenced by the machining process while also changing the thermomechanical effects. Because of this, numerical modeling is the only suitable avenue for accurately predicting machining behavior [117]. For a constitutive model to be ideal for computational software, it should contain few material constants and require minimal experimental data for calibration [118]. However, besides selecting the optimal material constants for a given model, the selection of the constitutive model itself is also crucial. Depending on the cutting conditions and material,

various models will yield different results [79]. For instance, Jaspers et al. [119] assessed the results obtained using the JC and ZA models and found that the JC model provided more accurate results for aluminum alloy AA 6082-T6 whereas the ZA model was the better choice for steel alloy AISI 1045.

In terms of output values, Adibi-Sedeh et al. [120] studied the variation between FE simulations of the JC model, the Oxley model [121], and the strain history model [122]. They observed that the JC model produced the best chip thickness predictions whereas the Oxley model produced the best thrust force predictions—however, none of the models performed the best in all categories of output values. Liu et al. [123] benchmarked several constitutive models to evaluate their efficacy in the FE modeling of machining titanium alloy Ti-6Al-4V. Among the models that were compared are the JC and ZA models, where they found that the JC underestimated whereas the ZA overestimated the peak temperature in the cutting zone.

Models that do not account for thermal softening will have difficulty predicting the chip temperature, as was shown by Styger et al. [124], who compared the basic JC model and a MJC model that both do not include thermal softening with a MJC model that does account for it. Results showed that the models that did not encompass the softening effect overestimated the chip temperature when compared to experimental data. However, important to note is that the lack of thermal softening in a constitutive model may not necessarily impact the ability for the FE simulation to predict the chip formation, as both MJC models in the study by Styger et al. [124] were able to accurately predict the onset of adiabatic shear banding (which drives the chip formation). To

399

400

401

402

403

404

405

406

407

408

409

410

411

412

413

414

415

416

417

418

accurately capture adiabatic shear band development, constitutive models must include a damage evolution model to accurately capture the adiabatic shear band formation (i.e., accounting for the inverse Hall-Petch effect) [79, 84]. Moreover, the type of constitutive model has a significant influence on the chip morphology because it affects the thermoplastic shear and hot mechanical properties [123].

In addition to identifying an adequate constitutive model, it must be able to accurately characterize the friction and heat transfer at the tool-chip interface, as this will dictate the results of output values such as chip thickness and temperature [117]. For example, Styger et al. [124] cite that the poor accuracy of feed force predictions obtained with various versions of the JC model could be attributed to the chosen friction law and coefficient of friction. Shi and Attia [125] proposed an approach to characterize behavior at the tool-chip interface using a friction model based on the empirical model by Shirakashi and Usui [126] and the thermal constriction model by Attia and Kops [127]. In their modified model, they formulated the shear friction factor (m) to be variable and compared it to other works that assumed this parameter to be constant. Simulated results in DEFORM-2D for the cutting forces, chip thicknesses, and cutting temperature showed that the errors for the model with a variable m were considerably smaller than the models where it was constant. The approach laid out by Shi and Attia [125] is advantageous because m is calculated as a function of the rake face's normal contact pressure, so it only requires minimal experimental data for calibration and the same coefficients can be used for the same cutting tool and workpiece material. Alternatively, the common approach

used in literature for the Usui model involves calculating a new m each time to match the experimental data, which is of course inefficient [125].

To summarize, the main output value of interest must be considered before selecting a model. Some output values are more sensitive to the constitutive model chosen than others, such as the cutting force, which has been shown to be more dependent on the type of model than any other output value, making it ideal for comparison and validation [118, 128]. Similarly, speaking to the importance of the formulation technique, FE programs are known to struggle with simulating chip formation, relying on unrealistic "artificial" chip separation methods—the Lagrangian and ALE formulations are beneficial in this respect because of their remeshing technique [96]. Thus, the formulation method is also very impactful on modeling results. All these factors must be considered when attempting to model machining processes, especially using numerical approaches such as the finite element method.

2.3. Thermomechanical Regimes & Deformation Zones of Machining Processes

Machining processes are characterized by extreme stresses, strains/strain rates, and temperatures, so an adequate model should consider the behavior of workpiece material under these conditions. The operating temperature of jet engines can surpass 900 °C [129], resulting in significant potential for high-temperature creep and thermomechanical cyclical loading. While jet turbine materials need to exhibit high creep resistance, hot hardness/strength, corrosion resistance, and fatigue strength, these properties are characterized at low strain rates—most material 'handbook data' (i.e., tensile and compressive test data) is obtained under quasi-static conditions (strain

442

443

444

445

446

447

448

449

450

451

452

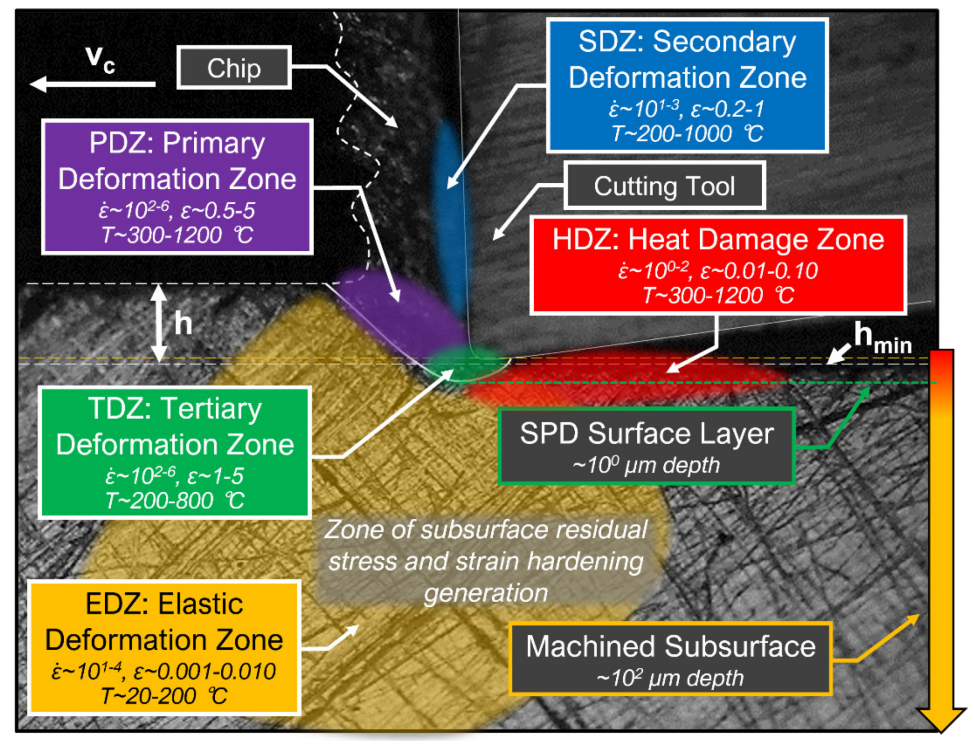
453

454

455

456

rates on the order of 10^{-2} s⁻¹). In contrast, the strain rates of most machining processes may exceed 10³ s⁻¹, which results in significantly altered material behavior. Thus, the difference between operation-specific and machining-specific regimes cannot be ignored when formulating a material model. Figure 4 shows the key deformation zones in machining processes outlined by Warnecke [130]: plastic deformation zone (PDZ), secondary deformation zone (SDZ), and tertiary deformation zone (TDZ), as well as two additional zones identified by the authors: the heat damage zone (HDZ) and elastic deformation zone (EDZ). Notably, while elastic deformations in the EDZ are on the order of 0.010 s⁻¹, accumulation of infinitesimal/elastic strains as the tool slides over a given point in the subsurface results in total strains that can be up to an order of magnitude larger (e.g., 0.010 as shown in Fig. 4). Indeed, incremental accumulation of miniscule local strains in the EDZ is the physical mechanism responsible for the development of residual stress and strain hardening, both of which are plastic deformation phenomena that occur far below the TDZ [90]. In this sense, the EDZ may more accurately be referred to as the 'Infinitesimal Strain Domain', while the PDZ, SDZ, and TDZ occur in the 'Finite Strain Domain'.



of the results.

Fig. 4. Deformation zones in cutting processes illustrated qualitatively on an in-situ micrograph of the orthogonal cutting process. Micrograph taken at $v_c = 60$ m/min, h = 50 µm for orthogonal cutting of Inconel 718 at 60,000 fps and 10X objective magnification.

Each zone shown in Fig. 4 endures different levels of stress and strain. Because of this, a machined part will have varied properties in different areas. Besides the geometry, machining changes the material in other ways, like the layer of plastic deformation and embedded residual stresses. As discussed in Section 2.1, there are several models that are commonly used in the industry, but there is no universal model that can account for all these machining byproducts. Some models are effective with certain materials based on the inputs into the model; this manuscript examines studies using these models to gain a better understanding of how inputs can affect the validity

3. BENCHMARKING OF THE JOHNSON-COOK PHENOMONELOGICAL MODEL

473

474

475

476

477

478

479

480

481

482

483

484

485

486

487

488

489

490

491

492

This section will discuss the state of the art in using the most famous constitutive model, the JC model, in FE simulations. The approaches for numerous authors are compared (i.e., their methods for calibrating the material constants, the FE software used, the formulation, etc.). Finally, a number of these models were analyzed by the authors of the present work and compared to experimental data for validation.

3.1. Ni-Based Superalloy Inconel 718

Inconel 718 is the most widely utilized Ni-alloy for aeroengine components because of its exceptional strength at high temperatures. It is used for the discs, casing, shafts, and many other components. The alloy is also used in other high heat applications such as reciprocating engines (i.e., turbochargers, metal processing tools, exhaust parts, and space vehicles components) [131]. The chemical composition of Inconel 718 was shown in Table 1. Other elements can be added to enhance the material (e.g., increased creep resistance) such as carbon (C), Co, Cu, phosphorus (P), and sulfur (S) [132]. Inconel 718 is expensive, costing over 50 USD per kilogram, so machining it requires expertise to avoid significant losses [133]. Acceptable surface integrity for materials that experience cyclical mechanical loading and substantial thermal loads (like Inconel 718) is imperative because microstructural flaws become more prominent at elevated temperatures and act as stress risers and crack initiation sites [134]. Inconel 718 is difficult to machine due to its poor thermal conductivity, high toughness, pronounced work hardening, and chemical affinity for most tools [96]. It was chosen as the focal point for this study because it is the most widely used Ni-alloy and

serves as a baseline for other similar alloys. Moreover, there is an abundance of work on this material, making it an ideal focus for literature review.

3.2. Formulations for Finite Element Simulations

Besides choosing a commercial FE software package for machining simulations, there are also different options for the formulation method. The three main types are Eulerian, Lagrangian, Arbitrary Lagrangian Eulerian (ALE), and Coupled Eulerian Lagrangian (CEL). Eulerian has a much lower computation time because it uses a fixed mesh, eliminating distortion—however, Eulerian does not consider material elasticity; this makes it so that the chip shape must be predefined, and it cannot predict residual stress [81]. Eulerian allows for the steady-state flow of the chip to be obtained; this involves computing the material flow through a fixed region in space, which is problematic because it requires the geometry of the chip to be predefined [135, 136].

Pure and updated Lagrangian formulations do not require the chip shape to be predefined, and allow for the entire process to be simulated, including unsteady flows [81, 135]. Although it should be noted that the Lagrangian formulation struggles with simulating severe plastic deformation because of mesh element distortion [137]. ALE was introduced to capitalize on the benefits of both approaches, where ALE can simulate unconstrained flow at high deformation rates by eliminating the need for a mesh on the workpiece, which is difficult if not impossible for Eulerian or Lagrangian [138, 139]. However, ALE cannot simulate serrated chips [137]. Finally, with the CEL formulation, the tool is a fixed Lagrangian body and the chip is simulated via a cross-sectional Eulerian mesh [140]. The workpiece is mesh-free, which allows for large plastic

deformation to be calculated since no remeshing is required [140]. Additionally, CEL has been shown to minimize computational times to 4 hours, as opposed to several days for ALE [141]. Furthermore, the formulation being used in the FE simulation is crucial, as improper choice of formulation based on the cutting conditions could drastically skew the results.

3.3. State of the Art for Constitutive Modeling with the Johnson-Cook Model

As discussed previously, the machining of Inconel 718 is most modeled with the JC model—especially for FE simulations. Thus, this section will aim at presenting an analysis of many recent approaches to using the JC model in FE software packages. The JC model can be calibrated in two ways: values can be obtained via experiment (which is costly and time consuming, typically by the SHPB test), or via FEM. Constants for the constitutive model such as A, B, C, m, and n are found via quasi-static tensile tests because this test examines the strain hardening behavior. Meanwhile, FEM simulates cutting processes to obtain values for thermal and mechanical properties. Many researchers use DEFORM 2D/3D or ABAQUS to attain values for constitutive models. FE simulations can be validated and calibrated via experimental methods, and literature review revealed this to be the preference.

Da Silva et al. [142] proposed a plasticity model based on JC and the model by Algarni et al. [143] that encompasses strain rate, strain hardening, thermal softening, stress triaxiality, and lode angle to predict residual stress. ABAQUS 2D with Lagrangian formulation was used for the simulations. Numerical results showed good accuracy when compared to the experimental results. Jafarian et al. [144] articulated a JC model

in DEFORM 2D in orthogonal turning of Inconel 718 by identifying one of seven models found in literature and calibrating it using an iterative process that utilized experimental and simulation methods. They emphasize that FEM was deliberately chosen to present the pros and cons in the approach. The authors incorporated the constant shear friction factor (m), global heat transfer coefficient (h_{ht}) , and the Coulomb constant (μ_c) to emulate the friction and heat transfer between tool and chip contact. Due to Inconel 718 chips forming adiabatic shear bands, the Cockroft and Latham criterion was also included to predict chip segmentation [144]. Each of the seven models were simulated under three testing conditions and compared with experimental data to select the most accurate model. For the chosen model, the thermal, frictional, and fracture criterion were calibrated and validated with experimental data. Once a sufficient JC model was derived, the FE software was mended to account for microstructural and microhardness changes using the Zener-Hollomon parameter and Hall-Petch equation [144].

The following paragraphs relate to the seven JC models discussed by Jafarian et al. [144], the first of which being by DeMange et al. [95], who used the SHPB test to identify new material constants for annealed and aged Inconel 718 (although Jafarian et al. [144] were only concerned with aged Inconel 718). The sampled Inconel 718 was induced to strain rates up to $1000 \, \text{s}^{-1}$ and temperatures ranging from 72-400 °C. Wang et al. [145] also obtained results via the SHPB test with strain rates in the range of 5000-11000 s⁻¹ and temperatures in the range of 500-800 °C. They proposed that C, the strain rate softening effect, was dependent on temperature and stain rate:

$$C = 0.0232 - \left[0.00372 + 0.0021\sin\left(\frac{\varepsilon - 5000}{3000}\pi\right)\right]\sin\left(\frac{T - 500}{150}\pi\right) \tag{6}$$

Again by the SHPB test, Pereira et al. [146] studied annealed and aged Inconel 718 at strain rates of 1600-5000 s⁻¹ while at RT. However, they neglected the thermal softening effect in their JC model. This may have impacted the work done by Mitrofanov et al. [98], as they utilized constants C and R from Pereira et al., but they calculated constants R and R from material property data. Lorentzon et al. [147] formulated a JC model that accounted for the thermal softening effect, R. This is analogous to the work done by Sievert et al. [148], although Sievert et al. [148] developed the thermal softening effect using annealed Inconel 718 whereas the proposed JC model was for aged Inconel 718.

Jafarian et al. [144] then discuss the work done by Özel et al. [96], who created a MJC model that incorporates the dynamic behavior of Inconel 718. This model also included the effect of temperature-dependent flow softening in addition to the standard parameters [96], and can be seen as equation 7:

$$\sigma = [A + B\varepsilon^{n}] \left[1 + C \ln \left(\frac{\dot{\varepsilon}}{\varepsilon_{0}} \right) \right] \left[1 - \left(\frac{T - T_{room}}{T_{melt} - T_{room}} \right)^{m} \right] \left[D + (1 - D) \left[\tanh \left(\frac{1}{(\varepsilon + S)^{r}} \right) \right] \dot{s} \right]$$
(7)

573 Del Prete et al. [149] introduced a hardness-based flow stress model. The initial workpiece hardness was accounted for by adding two functions, *F* and *G*:

$$\sigma = \left[A + (F + 200) + G\varepsilon + B\varepsilon^{n}\right] \left[1 + C \ln\left(\frac{\dot{\varepsilon}}{\varepsilon_{0}}\right)\right] \left[1 - \left(\frac{T - T_{0}}{T_{m} - T_{0}}\right)^{m}\right] \tag{8}$$

Jafarian et al. [144] then graphed the discussed JC models using DEFORM 2D in Fig. 5. The results from the models were then compared with experimental results to yield the optimal flow stress for the simulation. The curves were graphed at RT and at a strain rate equal to the quasi-static tensile test. Table 2 shows the corresponding

optimal constants to the curves in Fig. 5; the M1 model by DeMange et al. [95] was identified as the best for orthogonal cutting [144].

Table 2. Corresponding optimal material constants for flow stress curves shown in Fig. 5. Adapted from Jafarian et al. [144].

Model	A [MPa]	<i>B</i> [MPa]	С	n	m	$\dot{arepsilon}_0[\mathrm{s}^{\text{-}1}]$	Other constants
M1	1290	895	0.016	0.526	1.55	0.03	N/A
M2	963	937	Variable	0.33	1.3	0.001	C = Equation 6
M3	1485	904	0.0134	0.777	1.589	0.001	N/A
M4	1241	622	0.0134	0.6522	1.3	1	N/A
M5	1241	622	0.0134	0.6522	1.3	1	D = 0.6, S = 0, \$ = 5, r = 1
M6	1562	300	0.0164	0.25	1.7	1	N/A
M7	1241	622	0.0134	0.6522	1.3	1	F = 18 & G = 1.36

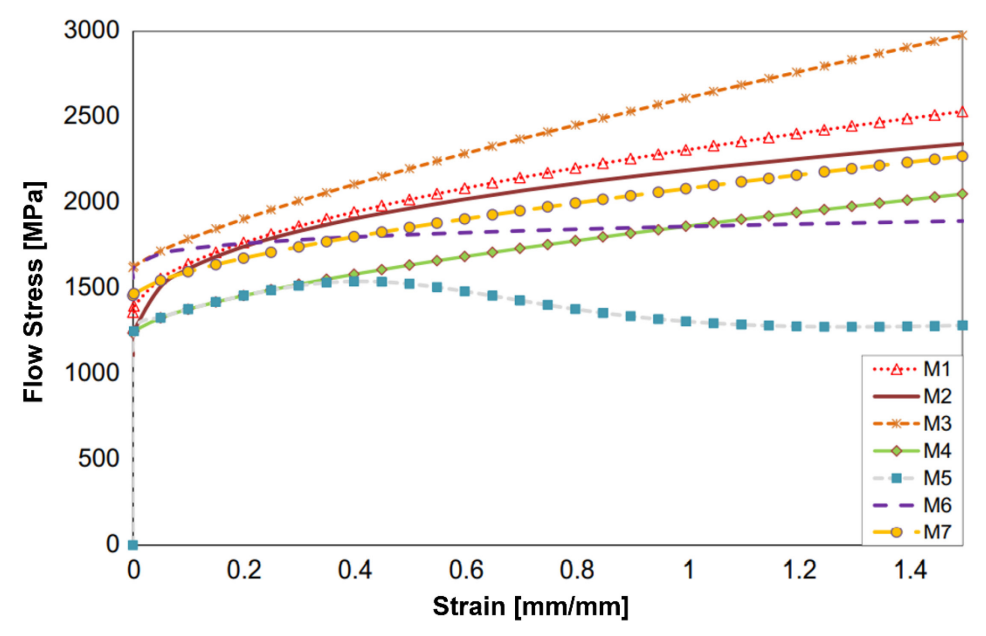


Fig. 5. Flow stress curves in relation to strain for various JC models [144]

Uhlmann et al. [150] used FEM (DEFORM 2D and ABAQUS) to produce turning simulations of annealed Inconel 718 under dry conditions. They used model parameters from Sievert et al. [148] (Table 3) to calibrate the FE simulations, except that B and C were slightly modified. The numerical specific and calculated cutting forces were graphed after integrating the data.

Table 3. Model parameters proposed by [148, 150]

A [MPa]	<i>B</i> [MPa]	С	n	m	$\dot{\varepsilon}_0$ [s ⁻¹]
450	1700	0.017	0.65	1.3	1.001

Since most FE software uses 2D orthogonal plane strain assumptions, arbitrary damage criterion, or remeshing techniques for simulating the chip, Özel et al. [96] argue that only 3D FE software can accurately simulate machining. They used ABAQUS 3D and DEFORM 3D to derive a JC model for Inconel 718. Temperature, strain, and stress values were obtained via simulation and compared with experimental data. They highlight that Pereira et al. [146] neglected to include thermal softening effects, whose model was used as reference in the work by [147, 150-153]. For instance, Özel et al. [96] reason that the model proposed by Sievert et al. [148] incorporates ductile damage and uses a combination of annealed and aged Inconel 718, but that they fail to provide the source of the parameters and the conditions of their dynamic tests.

First, Özel et al. [96] used ABAQUS 3D with ALE formulation. It should be noted that this approach only affects the mechanical solution which is directly influenced by mass scaling—the thermal solution is not affected. Mass scaling will however influence the accuracy of the mechanical solution. Since Özel et al. [96] chose the Coulomb friction law to model contact friction, they used parameters obtained by Lorentzon et al. [147], which are listed under M7 in Table 2. They also used a friction coefficient of μ = 0.6, which Lorentzon et al. [147] found using the Coulomb friction model in FEM.

Next, Özel et al. [96] used DEFORM 3D with updated Lagrangian formulation, which allows for the modeling of deformation and heat transfer using implicit integration. They used the JC model proposed by Lorentzon et al. [147] to model the

behavior of the workpiece. However, Özel et al. [96] modified the model to account for the flow softening phenomenon that occurs at high stress and strain rates by using the hyperbolic tangent function and additional parameters. Strain hardening, strain rate sensitivity, and temperature softening were also accounted for. The model can be seen in equation 9 and the parameters are listed in Table 4. The authors plotted the results of the model across various temperature and strain rate regimes to compare it with the basic JC, which can be seen in Fig. 6.

$$\sigma = \left[A + B(\bar{\varepsilon})^n\right] \left[1 + C \ln\left(\frac{\dot{\varepsilon}}{\dot{\varepsilon}_0}\right)\right] \left[1 - \left(\frac{T - T_0}{T_{melt} - T_0}\right)^m\right] \left[D + (1 - D) \left[\tanh\left(\frac{1}{(\varepsilon + S)^r}\right)\right]^s\right]$$
(9)

Table 4. MJC material constants proposed by Özel et al. [96]

Parameter	A [MPa]	<i>B</i> [MPa]	С	n	m	D	S	S	r	μ
Value	1241	622	0.0134	0.6522	1.3	0.6	0	5	1	0.6
mod JC	200°C 10/s 600°C 10/s 1000°C 10/s	→ mo	0.0134 od JC 200°C od JC 600°C od JC 1000°C 0600°C 1000	1000/s 1000/s C 1000/s	→ n	nod JC nod JC nod JC	200° 600° 1000	C 10 C 10	0000/s	's
200 -	· · · · ·						•		-	1
(0	0.5	1 strain [r	1.5 nm/mm]	l	2			2	.5

Fig. 6. Comparison of basic and MJC model at three different regimes Özel et al. [96]

The authors then compared the cutting forces obtained from both the ABAQUS and DEFORM simulations to the experimental trials, which are shown in Table 5. Each

trial used a new tool, and conditions were wet, which caused severe tool wear. The percentages shown in Table 5 refer to the prediction error for the simulated trials. It was found that DEFORM 3D with the MJC yielded the best results.

Table 5. Comparison of simulated and experimental results for cutting forces by Özel et al. [96]

Trial		F_c [N]	F_f [N]	F_p [N]
Francisco contol	V = 30 m/min	175	37	180
Experimental	<i>V</i> = 70 m/min	173	30	182
ABAQUS	V = 30 m/min, JC	306 (75%)	29 (22%)	204 (13%)
ABAQUS	V = 70 m/min, JC	274 (58%)	24 (20%)	189 (4%)
DEFORM	V = 30 m/min, JC	349 (99%)	34 (8%)	249 (38%)
	V = 70 m/min, JC		27 (1%)	200 (10%)
	V = 30 m/min, MJC	222 (27%)	23 (38%)	173 (4%)
	V = 70 m/min, MJC	188 (9%)	21 (30%)	157 (14%)

Jafarian et al. [134] used DEFORM 2D with updated Lagrangian code to achieve optimal parameters for the JC model in orthogonal turning of Inconel 718. The results were compared to the SHPB test conducted by Del Prete et al. [149] to assess accuracy. Jafarian et al. [134] used the Genetic Algorithm, which is a new technique based on the evolutionary optimization algorithm, to determine new material constants for the seven models analyzed in their previous work, Ref. [144]. They extracted experimental values for temperature, strain, and strain rate from literature; the difference between numerical and experimental flow stress was defined as the objective function to be optimized. When applying the Genetic Algorithm, the variables were updated for each iteration over several iterations. It should be noted that the specific range for each respective variable was accounted for. The optimized flow stress from the experimental

data is plotted in Fig. 7, and the sets of constants obtained from optimization for each of the seven models are shown in Table 6.

Table 6. JC material constants obtained via optimization by Jafarian et al. [134]

Model	A [MPa]	<i>B</i> [MPa]	С	n	m
M1	1016	899.1	0.0152	0.477	1.43
M2	964	937	0.016	0.444	1.5
M3	963	735.7	0.014	0.258	1.3
M4	900	752.1	0.023	0.561	1.65
M5	921.1	998.9	0.02	0.519	2.7
M6	906.7	999	0.017	0.290	1.24
M7	900	1054	0.017	0.460	2.1

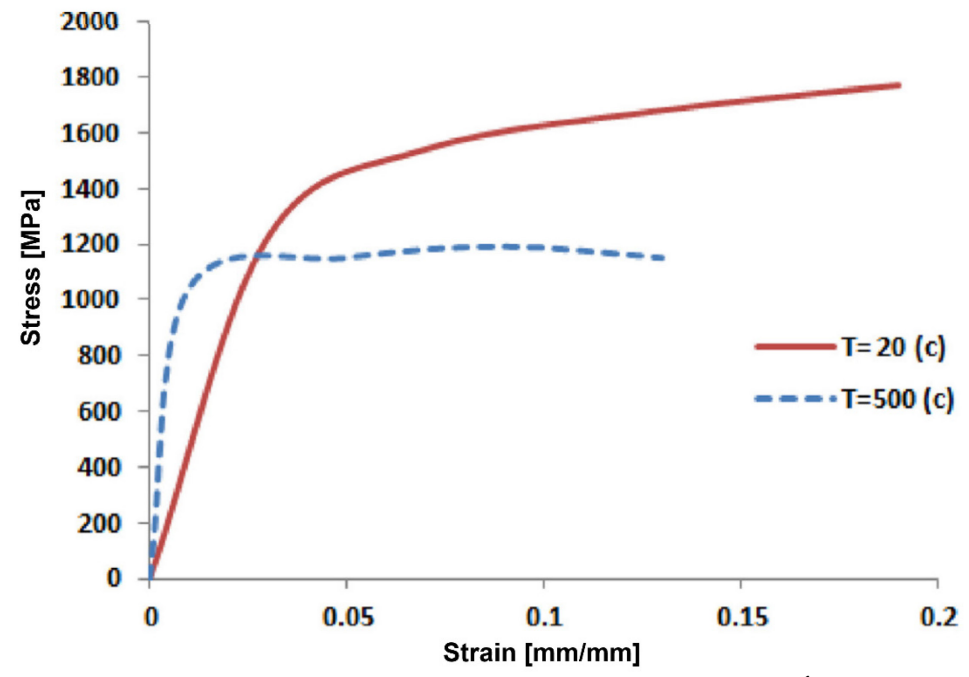


Fig. 7. Flow stress from experimental data at a strain rate of $0.001 \, \text{s}^{-1}$ [134]

The authors then tested each model in Table 6 using DEFORM 2D to determine the best one. It is important to note that they considered the Coulomb friction constant and the Cockroft and Latham damage criterion in the simulations to model chip segmentation. They also assumed the hybrid friction model variables to be constant $(m = 1 \text{ and } \mu = 0.3)$. The hardness-based flow stress model that dictated the FE

650

651

652

653

654

655

656

657

658

659

660

661

662

663

664

665

666

simulations are shown as equations 10-12. When comparing the numerical results to experimental data, Jafarian et al. [134] found that M7 yielded the lowest error at 12.8%, whereas M3 had the highest error at 24.1%.

$$\sigma_{eq} = \left[A + F + G\varepsilon + B\varepsilon^n\right] \left[1 + C\ln\left(\frac{\dot{\varepsilon}^p}{\dot{\varepsilon}_0}\right)\right] \left[1 - \left(\frac{T - T_0}{T_m - T_0}\right)^m\right]$$

$$F(HRC) = 2.008 \times HRC^2 - 141.97 \times HRC + 2305.4$$
(11)

$$F(HRC) = 2.008 \times HRC^2 - 141.97 \times HRC + 2305.4 \tag{11}$$

$$G(HRC) = -0.292 \times HRC^2 + 28.72 \times HRC - 700.3 \tag{12}$$

Wang et al. [145] used the SHPB test experimental approach to determine constants for the JC model. Their experiments tested the dynamic behavior of Inconel 718 at elevated temperatures (500-800 °C) and high strain rates (5000-11000 s⁻¹). They reason that many modeling attempts are subject to strain rates below 5000 s⁻¹, despite industrial machining processes occurring at 10^4 - 10^5 s⁻¹. In their work, experiments were supplemented with Third Wave FE simulations for efficiency. The power-law model was utilized, but the parameters are unknown. The highest strain rates observed from the software were 9500 s⁻¹ and 16000 s⁻¹, and the highest temperatures were 700 °C and 900 °C. To account for strain rate not being constant, the simulation was repeated three times and the values with good repeatability were used. Additionally, Wang et al. [145] conducted quasi-static compression tests at RT and a strain rate of 0.001 s⁻¹ to obtain quasi-static stress-strain data, which allowed for true stress and strain values to be calculated. Since instantaneous strain rate was found to not be constant during the SHPB test (which started at 800 °C), the stable part was averaged and used as the actual strain rate. The results of the compression and SHPB tests are shown in Fig. 8.

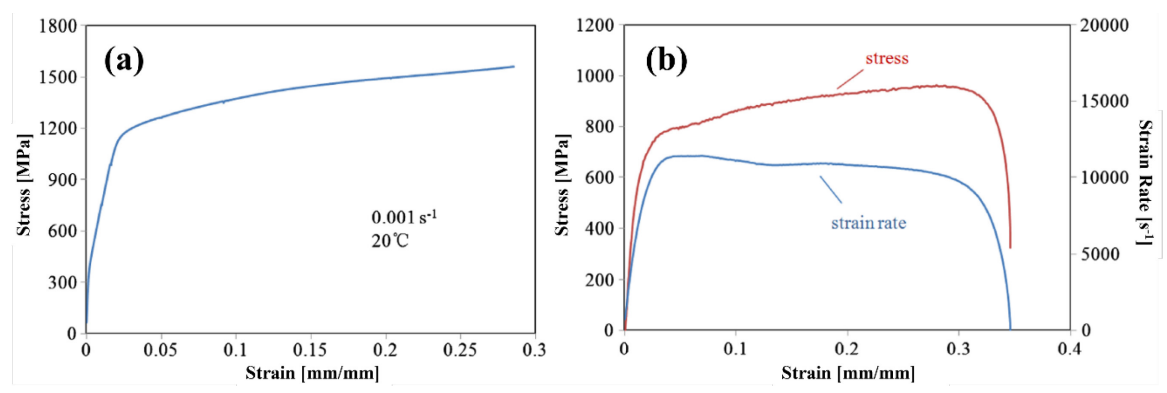


Fig. 8. Stress-strain curve for (a) compression test; (b) SHPB test [145]

Wang et al. [145] state that since the SHPB test is an adiabatic process, temperature could not be neglected. Therefore, the change in temperature was calculated using the following equation:

$$\Delta T = \int_0^\varepsilon \frac{\eta}{\rho c_v} \sigma d\varepsilon \tag{13}$$

The standard form of the JC (equation 1) was used with a plastic strain rate of $0.001 \, \mathrm{s}^{-1}$, $T_0 = 20 \, ^{\circ}\mathrm{C}$, and $T_m = 1320 \, ^{\circ}\mathrm{C}$. It was found that the basic JC model considers strain hardening, strain rate hardening, and the thermal softening effect as independent, but the SHPB test data revealed that they are not. The test also revealed that the effect of strain rate is dependent on temperature and there exists strain rate hardening and softening. Therefore, the authors suggested that the second bracketed term of the JC model should be modified to account for said variables, and this was done by deriving equation 6 for C since it was found to be strain rate and temperature sensitive. Figure 9 shows the flow stress curves for different strain rates at various temperatures and Figure 10 is a plot of the numerical results against the experimental results. Using this data and equation 6, the authors derived a series of constants for the

JC model, which are listed in Table 7. The percent error found between the numerical and experimental results was less than 8.5%, which the authors deemed as accurate.

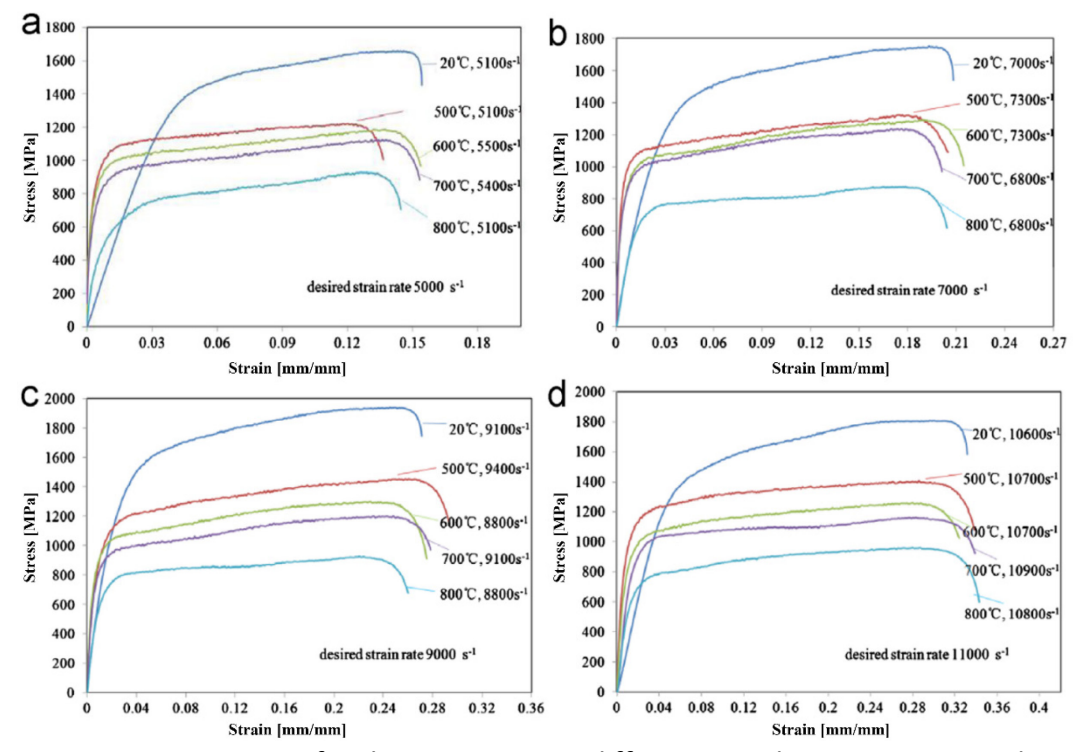
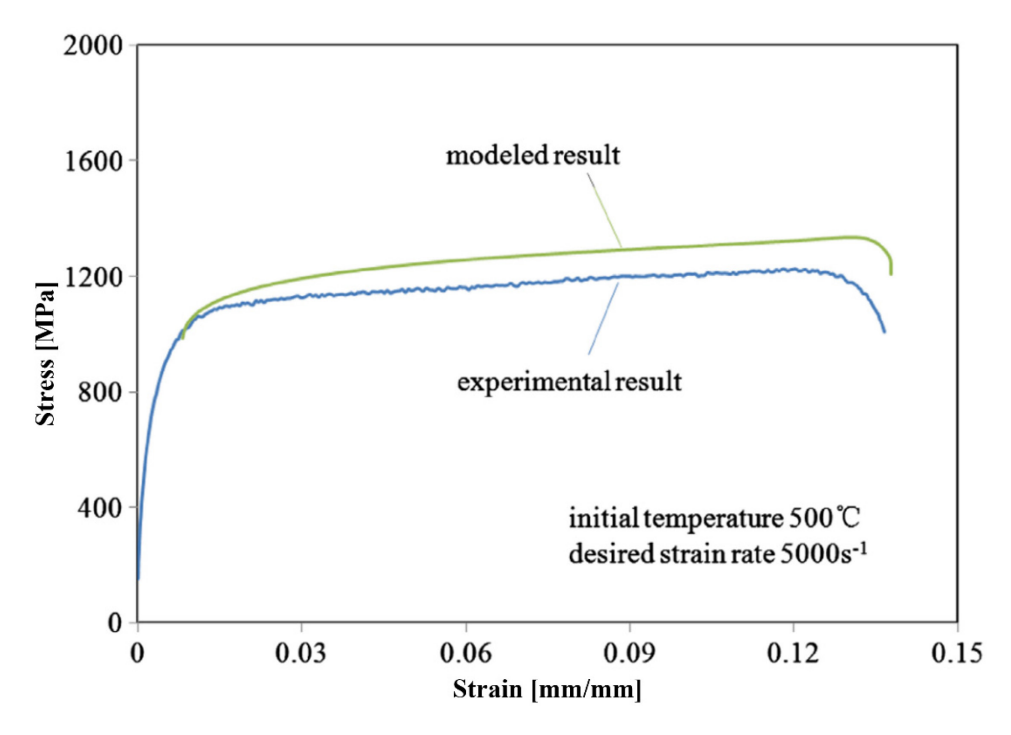


Fig. 9. Stress-strain curves for the SHPB tests at different initial temperatures and desired strain rates of (a) 5000 s^{-1} ; (b) 7000 s^{-1} ; (c) 9000 s^{-1} ; (d) 11000 s^{-1} [145]



690

691

692

693

694

695

696

697

698

699

700

701

702

703

704

705

706

707

708

709

Fig. 10. Comparison between numerical and experimental results [145]

Table 7. JC material constants parameters proposed by Wang et al. [145]

A [MPa]	<i>B</i> [MPa]	С	n	m
963	937	variable	0.333	1.3

Klocke et al. [154] used DEFORM 2D to attain values for their JC model. They reason that an accurate friction model is necessary for attaining values given that calculated forces are used to calibrate material constants. Further, they explain that friction has a considerable influence on the calculated cutting forces and chip parameters. They analyzed orthogonal cutting for AISI 1045 and Inconel 718 (for the purposes of this study, only the results for Inconel 718 will be discussed). They included the Cockcroft and Latham damage criterion because they mention that it affects chip geometry. The friction model used in this approach is hybrid, combining both simulation and experimental models and was developed by Puls et al. [155]. The purpose of this hybrid model was to develop the coulomb friction coefficients. Klocke et al. compared the material constants used in FEM models to those obtained experimentally. For constants A, B, and n of the JC model, the authors used values from an existing quasistatic flow stress curve: A = 1485 MPa, B = 904 MPa, n = 0.777 since they describe strain hardening behaviors. Constants C and m describe the impact of strain-rate and temperature. The cutting forces necessary for calculating the constants were obtained via broaching. Chip geometry values were analyzed by optical microscopy. To attain the true stress-strain curves, the method of least squares was used to fit constants A, B, and n. Relationships between material constants, predicted cutting forces, and chip parameters were used to interpolate values for C and m to decrease simulation error.

After 160 trials, the authors concluded that Trial 81 yielded the best solution, so they chose $\mathcal{C}=0.015$ and m=1.689.

Muthu et al. [131] used DEFORM 2D with updated Lagrangian formulation to attain data for the strain, temperature, and damage distributions in dry turning of Inconel 718. They highlight that while the JC model is widely used, it lacks the ability to predict flow stress at deformations below RT, as well as insight in the interaction between strain, strain rate, and temperature, and accounting for thermal softening phenomena. The parameters of their JC model are provided in Table 8:

Table 8. JC material constants parameters proposed by Muthu et al. [131]

A [MPa]	<i>B</i> [MPa]	С	n	m
1029.1	1477.5	0.06	0.33	1.44

The authors state that the material properties of the workpiece and tool materials, in addition to the flow stress data of Inconel 718, were incorporated into the simulations, although this data is not shown. Like the previous researchers discussed, they incorporated the Cockroft and Latham damage criterion to account for the fracture phenomena that causes serrated chips. They also included the Coulomb friction constant, as shown:

$$\tau = \mu \sigma_n \tag{14}$$

The authors chose μ = 0.6 and D = 100 for the friction coefficient and critical damage value, respectively. After performing simulations with tool nose radii of 0.6, 0.8, and 1 mm, it was found that a negative rake angle causes greater stress on the material, plastic strain is higher in the PDZ, and heat transfer primarily takes place in the shear

zone. It was also found that the damage distribution is dependent on the nose radius,
 and no chip serrations were observed.

Mahalle et al. [156] conducted a comparative analysis of the modified Cowper-Symonds (MCS), MJC, MZA, and integrated JC-ZA models. The material was hot-rolled Inconel 718, and the quasi-static hot tensile test was employed. Temperatures ranged from RT to 973 K, increasing in increments of 100 K. The strain rates tested are as follows: 0.0001, 0.001, 0.01 and 0.1 s⁻¹. By analyzing the experimental data from the stress-strain curves, Mahalle et al. [156] derived a formula for strain rate sensitivity based on the modified Hollomon equation:

$$m = \frac{\dot{\varepsilon}d\sigma}{\sigma d\dot{\varepsilon}} = \frac{\delta(\ln \sigma)}{\delta(\ln \dot{\varepsilon})} \tag{15}$$

The authors then assessed each constitutive model, starting with the MCS, which describes true stress using the uniaxial effective plastic strain and strain rate [156].

Equation 16 was then derived which gives the isothermal condition to the CS model. The values that optimize the MCS model for Inconel 718 are shown in equation 17. Mahalle et al. [156] also calculated the values for the material constants at various temperatures, as shown in Table 9.

$$\sigma_{y}\left(\varepsilon,\dot{\varepsilon}\right) = \sigma_{y}^{s}(\varepsilon) \left[1 + \left(\frac{\dot{\varepsilon}}{c}\right)^{\frac{1}{p}} \right] f(\varepsilon) \tag{16}$$

$$\sigma = (430.06 + 3.2325 \times 10^{3} \varepsilon^{0.9936}) \left(1 + 0.0078 \ln \frac{\dot{\varepsilon}}{0.01} \right) \left[1 - \frac{T - 298}{1302} \right]^{1.6221}$$
 (17)

Table 9. MCS material constants at various temperatures proposed by Mahalle et al.745 [156]

Temperature [K]	<i>K</i> [MPa]	С	P	n
RT	438.69	6.21	7.02	0.435
373	402.58	7.52	9.653	0.379

473	395.29	9.39	14.2	0.375
573	365.96	9.66	15.65	0.367
673	325.18	10.93	16.14	0.264
773	321.54	13.52	11.55	0.152
873	308.06	15.56	8.097	0.157
973	292.63	16.35	9.577	0.255

- The authors then discuss their MJC model. They note that the basic JC is
- incapable of defining material properties at high strain rates and temperatures, which is
- 748 why a MJC was proposed to rectify this:

$$\sigma = (A_1 + B_1 \varepsilon + B_2 \varepsilon^2) \left(1 + C_1 \ln \frac{\varepsilon}{\varepsilon_0} \right) e^{\left[\left(\lambda_1 + \lambda_2 \ln \frac{\varepsilon}{\varepsilon_0} \right) (T - T_0) \right]}$$
(18)

- where constants A_1 , B_1 , B_2 , λ_1 , and λ_2 were added to account for the coupled effects of
- 750 strain and strain rate with temperature. They then calculate values for the model:

$$\sigma = (444.95 + 3180.3\varepsilon + 187.29\varepsilon^{2}) \left(1 + 0.0036 \ln \frac{\dot{\varepsilon}}{0.01}\right) e^{\left[\left(-0.0002 + 0.0013 \ln \frac{\dot{\varepsilon}}{0.01}\right)(T - 298)\right]}$$
(19)

- The authors then discuss a MZA model, which is based on thermal activation by
- 752 dislocation:

$$\sigma = (C_1 + C_2 \varepsilon^n) e^{\left[(-C_3 + C_4 \varepsilon)(T - T_0) + \left[C_5 + C_6 (T - T_0) \ln \left(\frac{\dot{\varepsilon}}{\dot{\varepsilon}_0} \right) \right] \right]}$$
(20)

- 753 where C_1 is the YS of Inconel 718 at a strain rate and temperature, C_2 is the strain
- hardening coefficient, and n and C_3 - C_6 are the material constants that account for the
- influence of strain rate, temperature, and the coupled effects of temperature with strain
- and strain rate. The constants are then calculated:

$$\sigma = (260 + 1452.5\varepsilon^{0.884})e^{\left[-(7.7465\times10^{-4} - 7.533\times10^{-4}\varepsilon)(T - 298) + \left[0.0173 - 6.8605\times10^{-5}(T - 298)\ln\left(\frac{\varepsilon}{0.01}\right)\right]\right]}$$
(21)

Lastly, the authors address the integrated JC-ZA model, which combines the strain hardening term from the JC and the strain rate-temperature coupled term from the ZA. The authors modified the equation to account for the plastic deformation yielding:

$$\sigma = (A + B\varepsilon^n) \left[C_3(T + \Delta T) + C_4(T + \Delta T) \ln \left(\frac{\varepsilon}{\varepsilon_0} \right) \right]$$
 (22)

where A, B, C_3 , C_4 , and n are material constants at a strain rate of 0.01 s⁻¹ and ΔT is the average temperature rise because of deformation heat required to overcome plastic work. After comparing each model with experimental data, the JC-ZA exhibited the smallest error, and the MZA had the largest error.

Like many others, Grzesik et al. [157] used the SHPB test for obtaining experimental calibration data for the JC model. They looked at temperatures between 20-700 °C and strain rates at 10⁻³ and 10 s⁻¹. They used the FE software AdvantEdge to compare their three developed models applicable for different levels of strain rates to those found in literature as well experimental SHPB data. Their models had much lower prediction errors than the literature models, but they only tested low strain rates.

Hao et al. [99] studied the plastic behavior of Inconel 718 in the cutting zone with a JC model calibrated with the SHPB test in the regimes of 500-800 °C and 5000-10500 s⁻¹. They obtained A, B, and n through fitting of the experimentally derived stress-strain curves. The parameter m was determined by averaging the slopes of the stress-strain curves at different strain rates. Finally, C was calculated by simply rewriting the JC equation and solving using the other parameters while holding temperature constant—they observed good agreement when validating with ABAQUS simulations.

3.4. Benchmarking of Johnson-Cook Models for Inconel 718

Although FE analysis is more efficient, the relevant FE outputs such as cutting forces, chip morphology, and surface integrity (residual stress, hardness, microstructure, etc.) change based on process parameters such as cutting speed, uncut chip thickness/feed, and tool geometry, may include of the machined surface [79, 81, 85]. Occasionally, studies will omit the material chemical composition, whether it was aged or annealed, and what strain rates were present for Inconel 718. Furthermore, in some cases the thermal softening effect parameter, m, was assumed to be zero. This was the case for Mitrofanov et al. [153] and Pereira et al. [146]; studies that neglected the m parameter in their JC model could not be compared to other works that included it. Qiu et al. [158] showed that FE simulations are sensitive to changes in the JC parameters of A, B, m, and n, but unaffected by C. Additionally, they found that there were varying degrees of influence among the former four, with A being the most prevalent.

Although timely and more expensive, obtaining a constitutive model experimentally is more beneficial because it does not require input values and knowledge about the parameters for machining superalloys is accessible. Furthermore, it ensures that false information is not replicated by future authors, further escalating inaccuracies [96, 159]. It is crucial that authors explicitly outline the cutting parameters for their FE simulations to allow future researchers to understand how the constitutive model was obtained, as was done by Özel et al. [96], which was not always the case based on literature review. Predicted cutting forces presented by Refs. [98, 147, 148] showed mismatches when compared to experimental data, and various works used the

parameters presented by these authors which raises questions about their validity [96]. Özel et al. [96] asserts that 3D FE software is necessary to obtain accurate results, even though most of the authors discussed in Section 3.3 used 2D. In the literature reviewed, it is evident that FEM has high uncertainty given that all studies must compare numerical results to experimental data—this makes the success of several JC models questionable given that many were not compared to experimental results [144]. Nevertheless, FE parameters are typically calibrated with experimental data regardless.

Thus, a comparison between numerical and experimental results is necessary.

Flow stress curves for four of the deformation zones shown in Fig. 4 (PDZ, SDZ, TDZ, and EDZ) were created to compare the numerical methods for age hardened Inconel 718 to an expected curve. The plots assess models from authors discussed by Jafarian et al.

[144] as well as the one by Muthu et al. [131] and are shown in Fig. 11 (colored curves).

The temperature and strain rate were in accordance for each respective zone, although the strain rate of SDZ was taken at 5100 s⁻¹ to match the data from Wang et al. [145] (black curves), which is slightly outside the interval depicted in Fig. 4. Strain values were input ranging from 0.005-5.585 s⁻¹, but the graphs only display values from 0-2.5 s⁻¹.

Unless otherwise stated, a melting temperature of 1773 K was used. The methodology by Wang et al. [145] of calculating a different *C* parameter at each respective temperature and strain rate was accounted for in their model. Muthu et al. [131] does not provide an initial strain rate input, so a value of 0.001 s⁻¹ was assigned.

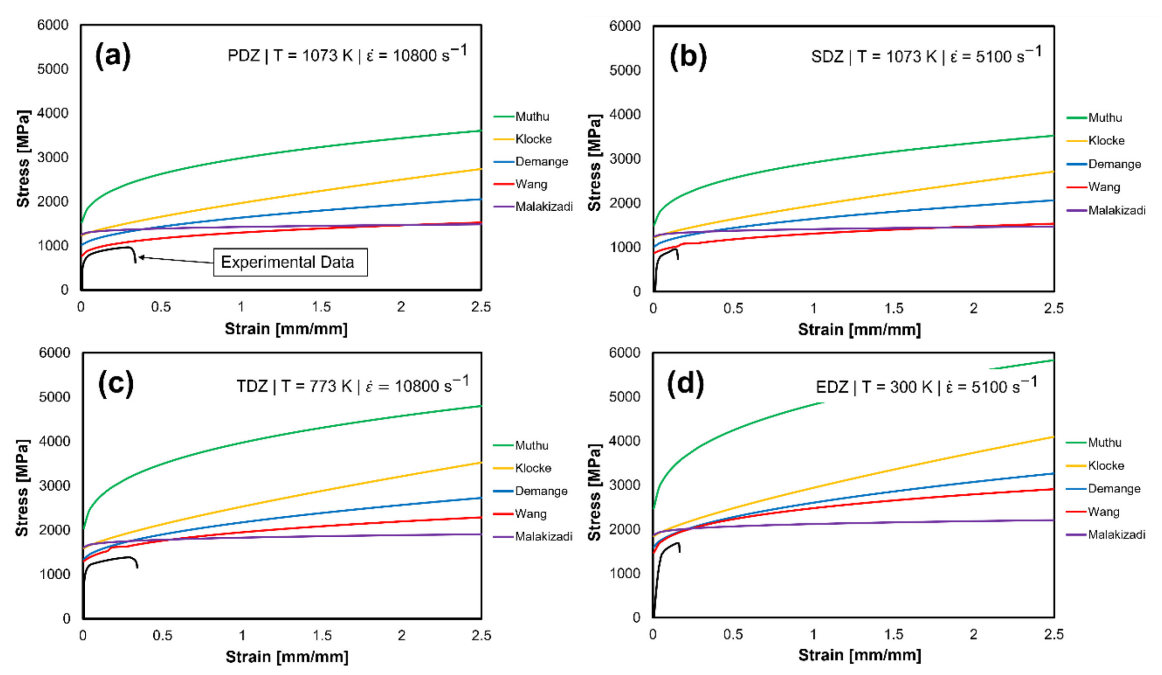


Fig. 11. Flow stress curves for aged Inconel 718 in the: (a) PDZ; (b) SDZ; (c) TDZ; (d) EDZ using models discussed by Jafarian et al. [144] (colored curves) as well as SHPB data from Wang et al. [145] (black curves) under similar thermomechanical regimes

As can be observed in Fig. 11, the models do not resemble a typical experimental stress-strain curve which are represented by the black curves, based on the data obtained by Wang et al. [145] in Fig. 9. This notable difference between models and calibration data is attributed to the method by which the authors attained the constants to their models, which is the SHPB test. The SHPB test does not represent the state of stress and other thermomechanical loading characteristics unique to machining, so it is proposed that SHPB data is not truly representative of the material behavior during machining. The SHPB test is only applicable for highly simplified tensile, compressive, and shear loading conditions, so the flow stress at extremely high strains cannot be extrapolated from SHPB data since fracture will occur at far lower strains due to the lack of extreme hydrostatic stress during deformation, as is typically the case during severe plastic deformation in machining.

4. FUTURE DIRECTIONS FOR MORE RELIABLE CONSTITUTIVE MODELING OF MATERIAL BEHAVIOR DURING MACHINING PROCESSES

This section discusses the future state of constitutive modeling, namely regarding physics-based models and direct calibration of material constants through machining experiments. First, several notable physics-based models are compared, including both their strengths and shortcomings. This is followed by a discussion of the important of boundary conditions and process parameters in FE simulations. Finally, the novel in-situ approach is analyzed in the context of constitutive modeling, and recent studies using in-situ techniques in this context are explained.

4.1. Physics-Based Modeling

Phenomenological models like the JC have their limits and cannot be relied upon to give the most accurate modeling results because they usually do not consider microstructural refinement mechanisms [160]. In the case of JC, the most widely used model, the parameters are uncoupled—that is, the effects due to strain and temperature are assumed to be independent of one another [161]. This is where physics-based models come in, because unlike phenomenological models, they model the behavior of temperature and strain with respect to grain dislocations, which allows them to describe deformation behavior due to plastic flow [162, 163]. Ni-alloys are crystalline materials where the microstructure is easily changed due to things like DRX, twinning, and phase transformations which occur at extreme levels of strain and temperature—understanding these mechanisms is necessary for accurate modeling [85]. This section will briefly

describe physics-based models to shed light on how they can capture effects not possible with phenomenological models.

Plasticity is attributed to the dislocations of crystals, and dislocation density (a measure of the length of dislocation per crystalline unit volume) is typically the basis for most physics-based constitutive models [162]. Strain hardening (the tendency of a material to strengthen with deformation) occurs because of rapidly increasing dislocation density with strain at high temperature compression, so it is a very relevant parameter in machining [160]. Dislocation density is also an indicator of the onset of DRX, which is the refinement in grain size due to permanent deformation. DRX nucleation is tied to the deformation temperature and strain rate: as the deformation temperature increases, the volume fraction of the DRX increases because the nucleation and growth rates increase [160]. DRX also increases with strain rate because strain rate raises the grain storage energy and subsequently the driving force of nucleation, resulting in a higher nucleation rate [160]. Zhu et al. [160] proposed a model based on the critical dislocation density where DRX occurs:

$$\sigma_{S} = k_{1} * \sinh^{-1} \left[n_{3} \left(\dot{\varepsilon} * e^{\frac{Q}{RT}} \right)^{n_{4}} \right]$$
 (23)

$$\sigma_{SS} = k_2 * \sinh^{-1} \left[n_5 \left(\dot{\varepsilon} * e^{\frac{Q}{RT}} \right)^{n_6} \right]$$
 (24)

$$\sigma = \sigma_{s} - (\sigma_{s} - \sigma_{ss}) \left[1 - \exp \left[-\beta_{d} \left(\frac{\varepsilon - \varepsilon_{c}}{\varepsilon_{0.5}} \right)^{k_{d}} \right] \right]$$
 (25)

where σ_s is the saturated stress, σ_{ss} is the steady stress, k_1 , k_2 , n_3 , n_4 , n_5 , n_6 , and β_d are the material constants to be calibrated, ε_c is the critical strain, $\varepsilon_{0.5}$ is the strain at a DRX volume fraction of 50%, Q is the activation energy, and σ is the flow stress. Physics-based

models such as this can then be coupled with dislocation density models, as was done by Zhu et al. [160] with the Laasroui-Jonas formulation to model dislocation density and the Goetz formulation to model dynamic recovery. This approach showed excellent agreement with experimental data.

The most widely used physics-based model is the ZA model, which was introduced earlier in Section 2.1 The ZA model has been famously utilized in FE simulations of Ni-alloys because it is based on a theory that specifies how thermal loads induce dislocation motion [164]. The ZA model specifically introduced a dislocation-mechanics based constitutive equation for the calculation of material flow stresses [118]. The ZA model is sometimes preferred to the JC model because it couples strain rate and temperature; the issue with the ZA model is that it cannot be used to predict flow stress at elevated temperatures (exceeding 70% of melting temperature) and lower strain rates [118]. The ZA model is unique in that it considers the crystal lattice type, differentiating between FCC and body-centered cubic (BCC) [81, 85]:

$$\sigma = C_0 + C_1 \exp\left[-C_3 T + C_4 T \ln\left(\frac{\varepsilon}{\varepsilon_0}\right)\right] + C_5 \varepsilon^n \qquad \text{for BCC}$$
 (26)

$$\sigma = C_0 + C_2 \varepsilon^n \exp\left[-C_3 T + C_4 T \ln\left(\frac{\dot{\varepsilon}}{\dot{\varepsilon}_0}\right)\right] \qquad \text{for FCC}$$
 (27)

where σ is the flow stress, ε^n is the equivalent plastic strain, $\dot{\varepsilon}$ is the plastic strain rate, $\dot{\varepsilon}_0$ is the reference plastic strain rate, T is the temperature. C_0 , C_1 , C_2 , C_3 , and C_4 are the strain-dependent, strain rate-dependent, and temperature-dependent constants based on the crystal structure [85].

Gurusamy et al. [118] modified the ZA and validated the flow stresses predicted by their proposed model with those calculated by the distributed primary zone deformation

896

897

898

899

900

901

902

903

904

905

906

907

908

909

910

911

912

913

914

915

916

model (DPZD), by comparing the FE predictions of cutting forces calculated from the ZA model with experimental data, and by comparing the flow stresses predicted by the ZA model with SHPB test data. The FE model was generated using the CEL formulation in ABAQUS/EXPLICIT. As was previously established in Section 3.4, the SHPB test is not adequate for calibrating material constants. Thus, Gurusamy et al. [118] used a semianalytical method where machining data was used in conjunction with models by Merchant [165] and Oxley [166] (this approach will be discussed further in Section 3.2). Excellent agreement was reached for the first two validation methods (comparison with values obtained from the DPZD model and values of experimental cutting force data), where the error was within 8% [118]. However, the stress-strain curves of the MZA model and the SHPB test data were only in agreement between 0.4 and 0.6, which is extremely low; this once again shows the shortcomings of the SHPB test in the context of machining. Other studies [167, 168] have reported similar findings with their ZA models, where agreement with mechanical tests like the SHPB but also tensile and hot compression tests was only shown for strain rates lower than 0.6.

The MTS model by Follansbee and Kocks [169] is a well-known physics-based constitutive model. In the MTS model, a single hardening function is used to describe forest dislocations by treating the thermal barriers in between dislocations as individual threshold stresses [170]. The output of the model is the yield stress (σ_y) at any state [171]—the MTS model is shown in Fig. 12. Liu et al. [172] modified the MTS model to include the contributions of grain size on the flow stress (green box in Fig. 12). Rinaldi et al. [173] modified the MTS model to include the contribution of twinning, which is

prominent at high strain rates, poor crystal symmetry, or low temperature (blue box inFig. 12).

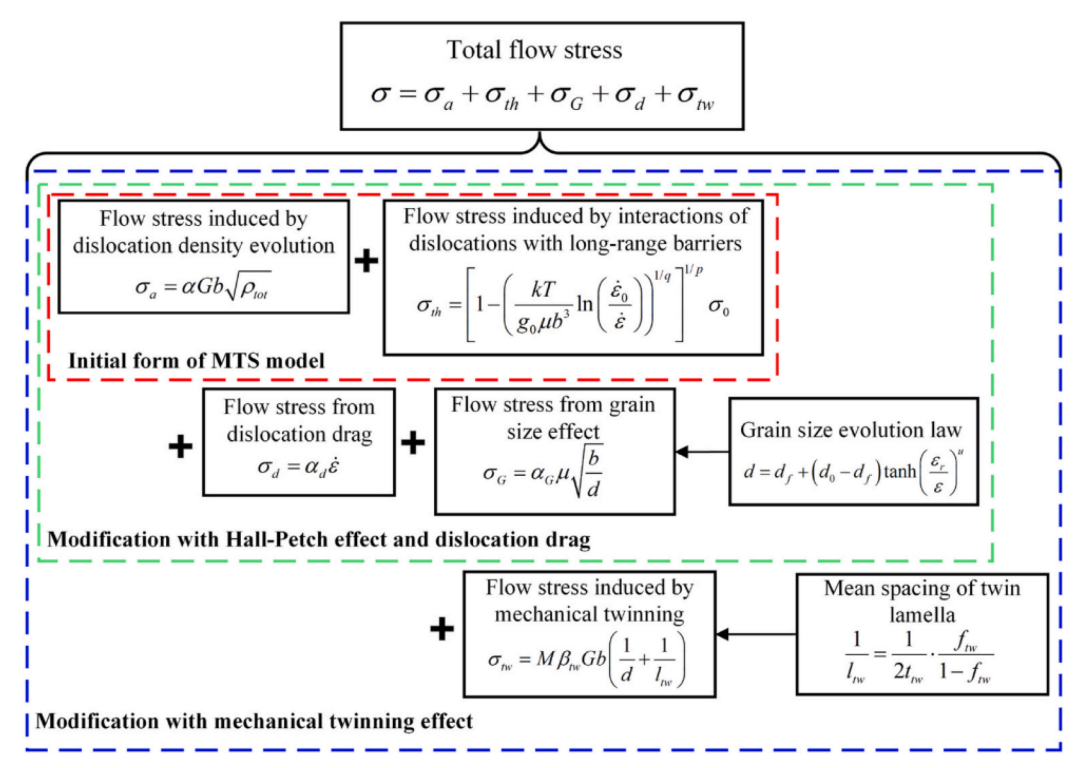


Fig. 12. Variations of the MTS model [85]

The nomenclature of all the variables in Fig. 12 is discussed by Liu et al. [85]. Like Zhu et al. [160], Atmani et al. [174] also coupled a physics-based model (MTS) a with dislocation density models for increased accuracy. Using this combined MTS-DD model, they simulated orthogonal cutting in ABAQUS 2D with ALE formulation. The dislocation density-based (DDB) model by Estrin et al. [175] describes the existence of a 'dislocation cell' during deformation that consists of dislocation cell walls and dislocation cell interiors—these each have their own dislocation densities. Besides the cell wall dislocation density (ρ_w) and cell interior dislocation density (ρ_c), there is the statistical dislocation density (ρ_w) and geometrically necessary dislocation density (ρ_w). However,

the big drawback of the DDB is that it is driven by a single deformation mechanism, so it cannot account for multi-deformation mechanisms and is also limited to single-phase materials [85]. MTS was used for modeling the cutting process and the DD model was used for predicting the grain size of the workpiece. Atmani et al. [174] compared the true stress-strain curves obtained using the combined MTS-DD model with the basic JC and the former showed much better results than the later, further illustrating the superiority of physics-based modeling:

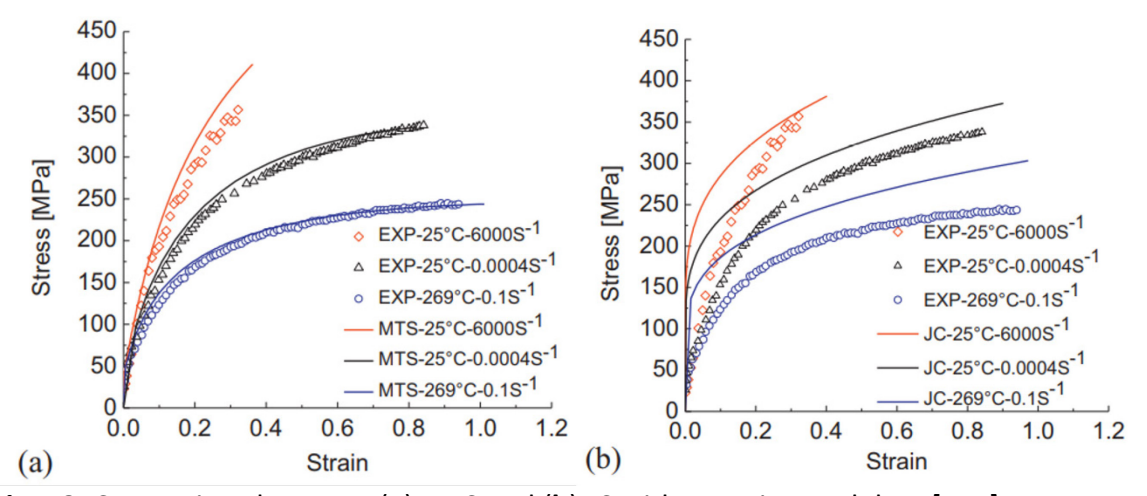


Fig. 13. Comparison between (a) MTS and (b) JC with experimental data [174]

Since Ni-alloys are usually poor thermal conductors, heat tends to accumulate in the PDZ, which results in shear localization and furthermore chip segmentation [84, 176]. Chip segmentation is an indicator of undesirable vibrations which cause oscillating cutting forces that can lead to more rapid tool wear and subsequently poor surface integrity [84, 177]. Additionally, microstructural behavior is more sensitive in the chip as opposed to the machined surface because the bulk of plastic strain occurring in the PDZ—microstructural effects can alter chip morphology, which then changes the thermomechanical loading [85, 174]. Thus, accounting for the chip formation mechanism

is imperative in physics-based modeling. Melkote et al. [84] also coupled a physics-based model with a grain refinement model to characterize the constitutive behavior of high DRX in the adiabatic shear bands. The model, based on thermal activation theory, states that the flow stress is given by superposition of three other stresses:

$$\sigma = \sigma_a + \sigma_{th} + \sigma_d \tag{28}$$

$$\sigma_a = \sigma_G + \sigma_\rho = \frac{\alpha_G G \sqrt{b}}{\sqrt{D}} + \alpha_\rho G b \sqrt{\rho}$$
 (29)

$$\sigma_{th} = \left[1 - \left[\frac{\kappa T}{g_0 G b^3} \ln\left(\frac{\dot{\varepsilon}_0}{\varepsilon}\right)\right]^{1/q}\right]^{1/p} \sigma_0 \tag{30}$$

$$\sigma_a = \alpha_d \dot{\varepsilon} \tag{31}$$

where σ_a is the athermal stress, σ_{th} is the thermal stress, and σ_d is the dislocation drag stress. The athermal stress is determined by summing, σ_G and σ_ρ , which represent the stresses due to resistance of grain dislocations (at the boundaries and in forests, respectively); α_G and α_ρ are parameters related to the strength of these interactions. Two particularly relevant parameters are D and ρ (grain size and dislocation density, respectively), which are internal state variables. σ_0 is the stress for "overcoming short range obstacles" and α_d is the dislocation drag coefficient [84]. K, T, $\dot{\varepsilon}_0$, $\dot{\varepsilon}$, g_0 , b, p and q are the same as in the MTS model (shown in Fig. 12).

Melkote et al. [84] then performed FE analysis in AdvantEdge 2D. Like Refs. [96, 131, 144, 154], they included the Coulomb friction law to account for contact at the tool-chip interface. In addition to analyzing cutting force data, they also simulated and compared the chip morphology to experimental data. They calculated the chip peaks, valleys, and segmentation frequency. The focus of this study was to model the microstructural changes in the chip, particularly along the adiabatic shear bands (see Fig. 14). At A there

is little grain refinement because of low plastic strain. Moderate grain refinement occurred at the periphery of the shear band (B), so there was large plastic strain here. Finally, C yielded an ultrafine grain size, meaning that there was severe plastic deformation. Small cracks were seen at D.

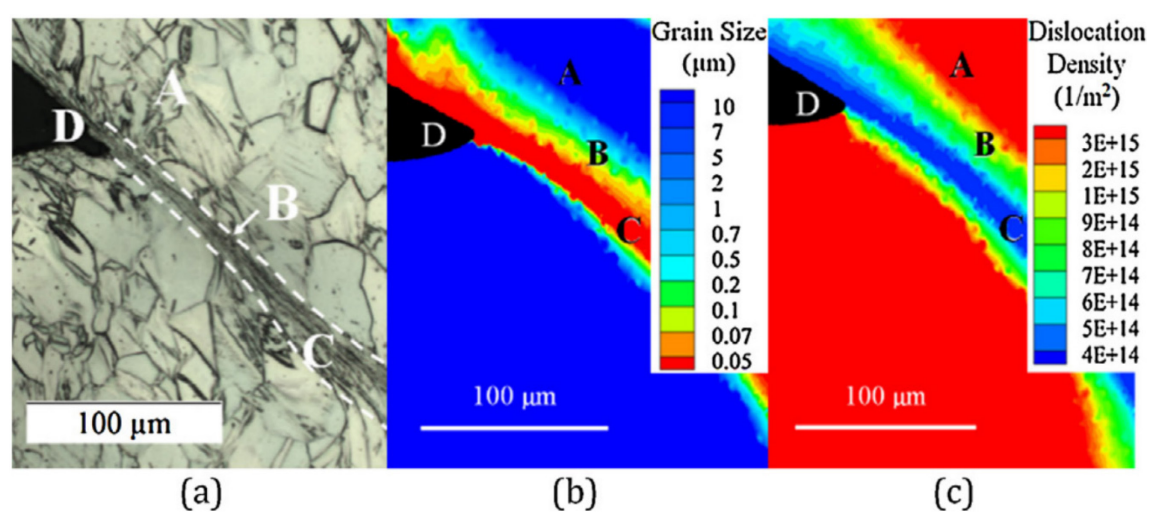


Fig. 14. (a) Micrograph of chip microstructure along adiabatic shear band; (b) grain size and (c) dislocation density distribution along the shear band [84]

When simulating machining processes, it is important to understand the effects of boundary conditions, as they can considerably affect the accuracy of modeling results. Arguably the most prominent of these boundary conditions is the rake angle, as it has significant effects output values like the cutting forces and chip size. For instance, a positive rake angle will yield lower forces because it reduces compression whereas a negative rake angle will yield higher forces because it increases compression [178]. In terms of chip formation, the rake angle is a critical parameter because of its effect on chip segmentation, which shifts from continuous to serrated when the rake angle is adjusted from positive to negative [179]. Additionally, it has been shown that a positive rake angle will create larger chips whereas a negative rake angle will create the smaller chips [178].

For the purposes of FE simulations, a neutral rake angle of 0° is preferred because it generates the largest thickness for the PDZ, which is desirable for calculating the physical quantities of flow stress, strain, strain rate, and temperature in the PDZ for analytical modeling [179, 180]. It has indeed been shown that the 0° rake angle yields the most accurate flow stress prediction [179, 181].

In terms of feeds and speeds, feed rate is not usually a controllable parameter in FE modeling, so its effects are not fully understood. Cutting speed, however, has been shown to have a strong influence on simulations. For instance, there is little to no sawtooth chip formation at low speed because of the low temperature and sufficient time for heat conduction (adiabatic shear banding happens once the tool tip reached a certain temperature) [182]. It has been shown that chips transitioned from continuous to serrated when the cutting speed was increased [177, 183]. Jomaa et al. [184] observed that chip curling and segmentation frequency increased with cutting speed.

At higher velocities, the cutting forces can also increase with cutting speed due to dominant strain (rate) hardening [178]. When cutting at low speeds, model configurations can be modified to exclude certain criterion that are not applicable in lower regimes. For example, Zhang et al. [185] omitted the sensitivity of flow stress to thermal and strain rate in their power law model because they held the cutting speed at 0.1 m/min. Ding and Shin [141] also performed cuts at 0.1 m/min and they disregarded DRX since it is not applicable at very low speeds. Boundary conditions have a significant effect on cutting temperature: it has been shown that cutting temperature increases with higher cutting speed, depth of cut, and edge radius [186-188]. The tool materials, like the coating, can

1005

1006

1007

1008

1009

1010

1011

1012

1013

1014

1015

1016

1017

1018

1019

1020

1021

1022

1023

1024

1025

also affect the simulation. Lower temperatures at the tool-chip interface have been obtained with coating carbide tools than uncoated [189, 190].

Other physics-based modeling efforts include Yuan et al. [191], who studied the influence of heat treatment on the plastic flow behavior of laser metal deposited Inconel 718 in the regimes of 25-1000 °C and 500-12000 s⁻¹. They proposed a microstructuralbased constitutive model to determine true stress and true strain. Variations in plastic flow behavior were determined based on the amplitude of the flow stress, the strain hardening component and temperature strain rate dependence. The differences in plastic flow behavior were assumed to be because of changes in grain geometry, volume fraction and y'' precipitates during heat treatments [191], which is supported by Ghorbanpour et al. [192]. The proposed microstructural constitutive model was accurate based on the experimental results. Tan et al. [193] analyzed the behavior of fine-grained Inconel 718 at low strain rates and high temperatures during compression tests. They observed that the flow stress would rapidly rise to a peak value, then decrease because of flow softening due to DRX. They compared the true stress-strain curves with curves predicted using the hyperbolic-sine Arrhenius model, which gives the relationship between strain rate and peak flow stress and temperature. They calibrated their constants through linear fitting of experimental data; numerical and experimental results were in excellent agreement. Another important aspect is dynamic strain aging, as observed by Voyiadjis et al. [194]. They looked at the inadequacies of various constitutive models that do not consider dynamic strain aging and developed a model that does consider these effects. After comparing modeled results to values obtained from experimentation, they saw that

values predicted by considering dynamic strain aging were much more accurate than those that did not.

This section has demonstrated the ability of physics-based models to capture features not possible with phenomenological models. There are however, limitations to physics-based models, as outlined by Liu et al. [85]:

- They assume the material has a single-crystal microstructure, which means they
 cannot be applied to materials with dual-phase grains and in scenarios where
 there are phase transformations, with the latter being an especially limiting factor.
- The sheer quantity of material constants in physics-based models makes calibration difficult. Some of the variables must be identified by fitting phenomenological models, which obviously defeats the purpose of using physicsbased models.

Liu et al. [85] further reason that physics-based laws cannot be the definitive replacement to phenomenological laws, as most modeling approaches typically require aspects of both. For instance, phenomenological laws can still be used in numerical simulations by adding microstructure models as state variables. For materials like Ni and Ti-based alloys that typically have a multi-crystal microstructure, phenomenological models would be more practical [85].

4.2. Direct Calibration of Material Constants

The SHPB test is the most widely used method for determining material constants in constitutive models, however it has already been established that it cannot reach the stresses and strains present in machining [81, 85, 92]. In machining operations, maximum

1049

1050

1051

1052

1053

1054

1055

1056

1057

1058

1059

1060

1061

1062

1063

1064

1065

1066

1067

1068

1069

strains in the PDZ, SDZ, and TDZ can reach values of 1, 4, and 4, respectively—meanwhile, the strains for tensile and compression tests only reach values of 0.2 and 1, respectively [161, 185]. The SHPB test can reach strain rates of up to 10^4 s⁻¹, which is not representative of high-speed machining conditions [161, 195]. Another reason the SHPB test is an outdated calibration method is because it carries high equipment costs and its heavily reliant on user expertise [196].

The alternative to conventional mechanical methods like SHPB is the inverse approach based on response surface methodology. The inverse method is performed by measuring cutting forces and chip thicknesses from orthogonal machining tests and used to analytically calculate the flow stress, strains, and temperatures in the PDZ; material constants are then determined via nonlinear regression [179, 197]. In the context of machining, the inverse method is synonymous with the term in-situ, which connotes direct and real-time observation of the cutting process by multiple sensor modalities, most commonly optical microscopy techniques [198]. By observing the complex process of chip formation and thermomechanical loading of the chip, tool, and workpiece in realtime, valuable data not previously possible with the SHPB test can be obtained. Namely, digital image correlation (DIC) can be used to analyze grain displacement by capturing high speed video of the cutting process—by comparing images between the loaded and unloaded condition, the displacement field of the material can be generated. This section will discuss works that have used in-situ techniques like DIC to calibrate constitutive models, which has proven to yield more accurate material constants than conventional means [179, 197].

1071

1072

1073

1074

1075

1076

1077

1078

1079

1080

1081

1082

1083

1084

1085

1086

1087

1088

1089

1090

1091

Tian et al. [97] used the reverse identification method to calibrate JC parameters for Inconel 718 in the solutioned annealed and precipitation hardened state with an analytical-experimental approach. The parameters of A, B, and n were determined by fitting the true stress-strain curve from quasi-static compression tests but constants \mathcal{C} and m were found by comparing with orthogonal cutting test data. Cutting force and chip morphology data as inputs into Oxley's [166] parallel shear zone model but also substituted in the Waldorf [199] slip line model to account for the ploughing force, which is neglected in the Oxley [166] model since it assumes a sharp edge. The equivalent stress, strain, and strain rate in the PDZ could then be calculated and used as the optimization parameters in the least-squares method based on the Genetic Algorithm. However, it is important to note that the tests were conducted at ambient conditions, where the temperature was only 20 °C and the strain rate was 0.001 s⁻¹, which is not representative of machining regimes. The C and m parameters were inversely identified with the least squares method which is based on the Genetic Algorithm. They verified their calibrated parameters by comparing experimental results to numerical results in DEFORM 2D, based on the Lagrangian formulation. While the authors obtained very good accuracy in this regard, they make clear that their model may only be suitable for low-speed cutting. They also highlight that there was a distinction in the behavior of Inconel 718 in the solution annealed state versus the precipitation hardened state, which resulted in significantly different constitutive parameters.

Similarly, Thimm et al. [161] also used quasi-static compression tests for constants A, B, and n but the inverse method for constants C and m. However, they used Oxley and

Welsh's [200] procedure to calculate the cutting forces and shear strain rate in the PDZ based on initially chosen values for C and m. These calculated values would be compared to the measured values and optimized over several iterations to find the constants that yielded the minimum deviation with experimental data, where the optimization algorithm would change C and m with every iteration [161]. While the cutting forces were captured with a dynamometer, the shear strain rate was captured optically via DIC, which was not employed by Tian et al. [97] The constants obtained by Thimm et al. [161] are shown in Table 10.

Table 10 JC material constants proposed by Thimm et al. [161]

A [MPa]	<i>B</i> [MPa]	С	n	m	$\dot{arepsilon}_0$ [s ⁻¹]
492	585	0.0088	0.1677	1.2162	0.001

Zhang et al. [92] also used an analytical-experimental approach for identifying the material constants in the JC model. In their study, experiments were conducted on an orthogonal cutting in-situ setup capable of high-speed imaging. Then like Thimm et al. [161], they performed DIC to generate the strain field in the PDZ in the x and y-directions. After normalizing the displacement data using the least-squares method, the equivalent strain rate was calculated, which was determined by integrating the equivalent strain rate. The authors used quasi-static compression tests to determine constants A, B, and n, but C and m were obtained via in-situ data of the orthogonal machining tests. C and C and C are determined using least-squares optimization, where the inputs are the predicted and measured forces along the primary shear plane. The predicted shear force C is given by the integral of the stress in the PDZ, which is assumed to be pure shear according

to Oxley and Shaw [166]—this shear stress can be derived to be a function of $\mathcal C$ and m. The true shear force is simply calculated using the measured cutting and thrust forces (F_c and F_t , respectively) and the shear angle (φ), observed from DIC. Their final constants for the nickel aluminum bronze alloy studied are shown in Table 11. Using the known JC model constants, simulations for the strain, strain rate, and temperature fields were performed in DEFORM and compared with the DIC data—results were found to be consistent [92].

Table 11 JC material constants proposed by Zhang et al. [92]

A [MPa]	<i>B</i> [MPa]	С	n	m
295	795.5	0.0217	0.4757	0.7775

Furthermore, studies like Zhang et al. [92] and Thimm et al. [161] show that mechanical tests can be used successfully in conjunction with the inverse method, as well as demonstrate the value of also harnessing the untapped potential of DIC. Bergs et al. [140] used DIC to calculate the strain rate in the PDZ. The results were validated against analytical predictions using the parallel-sided shear zone model by Oxley [166] and FE simulations in ABAQUS with CEL formulation. The DIC values were shown to match Oxley's [166] model far better than the numerical values. Recently, the authors of the present study have developed another direct approach for calibration of physics-informed models of process-induced surface integrity in Inconel 718 by using in-situ characterized subsurface displacement fields, which are proportional to the state of stress within the elastic limit. By comparing the measured displacement fields with model-generated stress fields,

Schoop et al. [90] demonstrated the ability to accurately predict subsurface residual stress profiles in turning of Inconel 718:

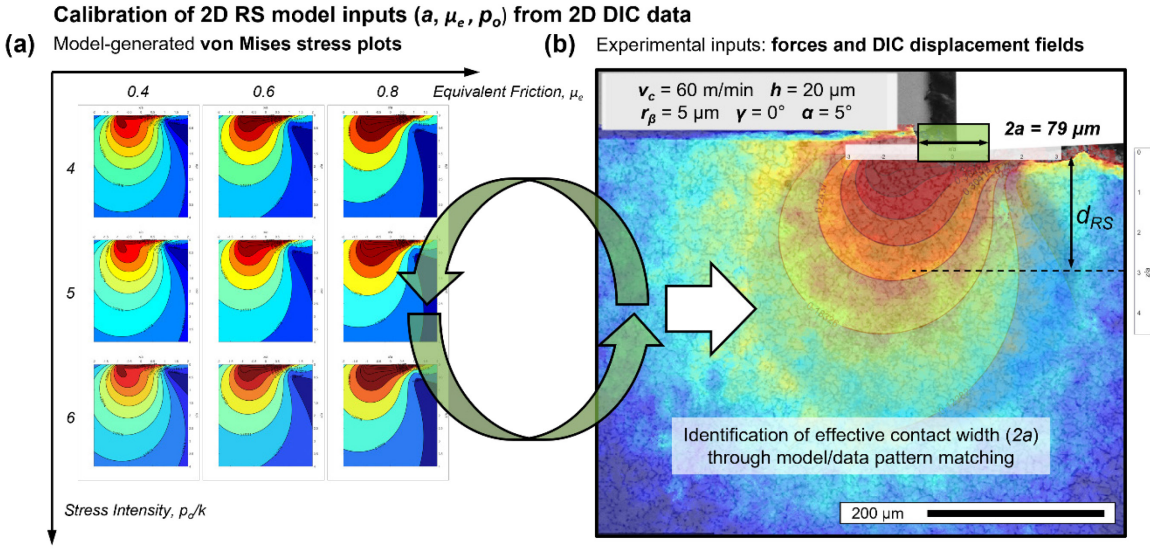


Fig. 15. Schematic illustration of the process for calibrating contact width: (a) modeling results of von Mises stress; (b) calibrating contact width from DIC displacement field [90]

Jomaa et al. [197] took a hybrid approach similar to Refs. [92, 97, 161], where both mechanical and machining data was utilized for calibrating constants of the Marusich's constitutive equation (MCE)—the MCE (shown as equations 32-34) has shown promising results but has seldom been explored or tested because material constants have not been published in literature [138, 197]. While the MCE is not microstructure based, it does account for dynamic effects like heat conduction and mesh-on-mesh frictional contact [138]. For the MCE model, Jomaa et al. [197] proposed a two-step approach, where constants would be calibrated via different methods depending on the regime. For the low strain rate regime, material constants would be attained via tensile/compression experiments (tensile tests, radial collapse of thick-walled cylinder, SHPB, etc.) and for the

high strain rate regime, material constants would be attained via the inverse method (orthogonal machining tests) [197].

$$\left(1 + \frac{\dot{\varepsilon}_p}{\dot{\varepsilon}_0}\right) = \left(\frac{\sigma}{g(\varepsilon_p)}\right)^{m_1} \text{ for } \dot{\varepsilon}_p < \dot{\varepsilon}_t \text{ (low strain rate)}$$
 (32)

$$\left(1 + \frac{\dot{\varepsilon}_p}{\dot{\varepsilon}_0}\right) \left(1 + \frac{\dot{\varepsilon}_t}{\dot{\varepsilon}_0}\right)^{\frac{m_2}{m_1} - 1} = \left(\frac{\sigma}{g(\varepsilon_p)}\right)^{m_2} \text{ for } \dot{\varepsilon}_p > \dot{\varepsilon}_t \text{ (high strain rate)}$$
 (33)

$$g(\varepsilon_p) = [1 - \alpha_{NL}(T - T_0)]\sigma_0 \left(1 + \frac{\varepsilon_p}{\varepsilon_0}\right)^{\frac{1}{n_{NL}}}$$
(34)

In the above equations of the MCE: σ is the equivalent von Mises stress, σ_0 is the yield stress, ε_p is the equivalent plastic strain rate, n_{NL} is the strain hardening exponent, α_{NL} is the thermal softening coefficient, m_1 and m_2 are low and high strain rate sensitivity coefficients, and T is the temperature. σ_0 , n_{NL} , and m_1 are the low strain rate parameters, calibrated with dynamic tests. m_2 and α_{NL} are the high strain rate parameters, calibrated with machining tests. Also for the high strain rate regime, two different temperature models from Oxley [201] and Loewen and Shaw [202] were each used to inversely calculate the constants from the machining data. Two sets of constants (one for each model) were generated and compared to determine the temperature sensitivity of each respective model.

Finally, DEFORM 2D was used to simulate the cutting process for three different alloys using the MCE with the Oxley temperature model (M1), the MCE with the Loewen and Shaw temperature model (M2), as well as the JC model with the Cockroft and Latham criterion for chip segmentation. These three models were analyzed with respect to the cutting forces, chip thickness, and tool-chip contact length. Tool-chip contact length is an output that is traditionally overlooked in optimization models but has been

shown to improve results when included; it can even be measured using DIC [185].

Results showed that MCE hybrid model was found to be much more accurate than JC, particularly regarding the cutting forces, as the latter would underestimate with errors of up to 55% in some cases [197]. The study showed that the selection of the temperature model has a major impact on the sensitivity of predictions for not only the temperatures, but the predicted responses as well [197]. Material constants for M1 proved more accurate for certain materials whereas the material constants for M2 performed better for others [197].

5. MATERIAL PROPERTIES & RESIDUAL STRESS TEMPERATURE CHARACTERIZATION

This section shows the strong temperature dependence of physical and mechanical properties of Ni-alloys. Many profiles and models were generated via curve fitting of experimental/tabular data for many different materials. The applications and traits of said materials are also briefly discussed.

5.1. Thermophysical Properties of Ni-alloys

This section presents the thermal profiles for the physical properties of a plethora of Ni-alloys. These properties include the thermal conductivity, linear thermal expansion coefficient, specific heat, thermal diffusivity, and density.

5.1.1. Temperature Dependence of Various Thermophysical Properties

Figures 16-19 show the temperature dependence of several physical properties for numerous Ni-alloys. Thermophysical property values at RT and other key

temperatures were obtained for Ni-alloys from various data tables. Using the thermophysical property values, the plots were constructed using the lowest order polynomial regression that fit the experimental and model-generated data was used to create these profiles in MATLAB. In most cases, these were second and third order polynomials.

One of the reasons Ni-alloys are difficult to machine is because of their poor thermal conductivity (A), which leads to increased temperature at the tool rake face, resulting in work hardening and a strong tendency for adhesion and built-up-edge conditions [42]. Although the thermal conductivity of Ni-alloys increases with temperature (as seen in Fig. 16), it is still much lower than it is for pure Ni [203]. The alloys in Fig. 16 increased by an average of 115% (or 16 W/m*K) between RT (taken at 20 °C) and 810 °C. A higher thermal conductivity (i.e., higher heat removal rate) is desired because it mitigates thermally induced damage during machining [204]. Louzguine-Luzgin et al. [205] mentions that Ni-alloys have a lower glass formability because of their low thermal conductivity compared to copper-based alloys. The thermomechanical coupling effect of the chip sliding against the rake face of the tool lowers the thermal conductivity but increases electrical conductivity for both workpiece and tool, which may trigger adhesion [204].

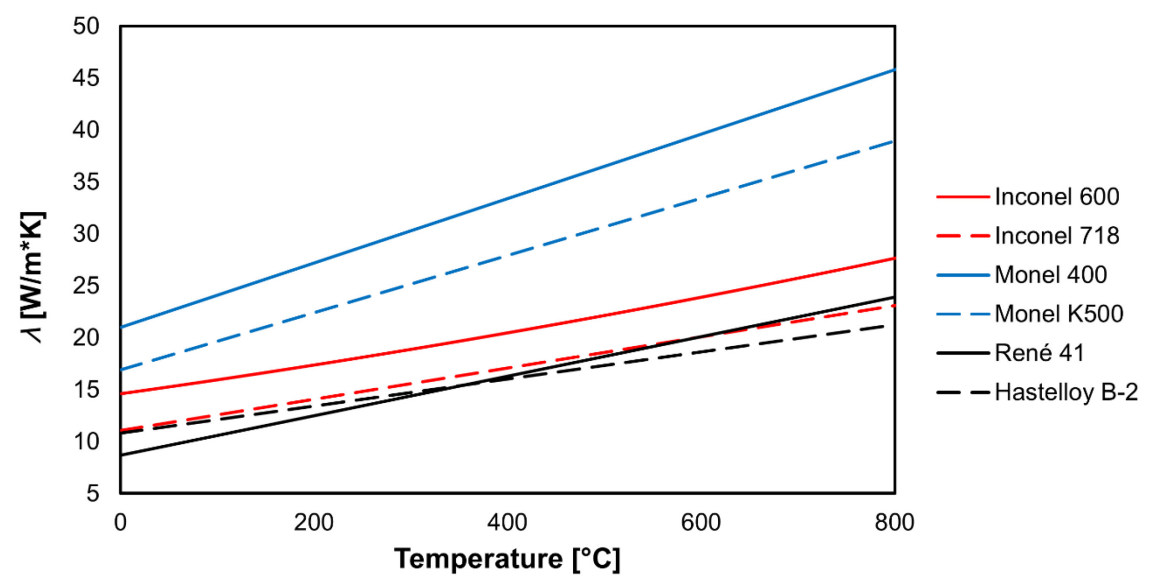


Fig. 16. Variation of thermal conductivity with temperature for several Ni-alloys. Curve fit data from [206-212].

The linear thermal expansion coefficient (α_L) corresponds to the rate at which a material expands or contracts due to changes in temperature. Materials with a low average thermal expansion coefficient develop fewer microcracks during machining applications [213]. Ni-alloys tend to have high thermal expansion coefficients, which leads to dimensional instability over a wide range of temperatures [214, 215]. Modifying a material's chemical compositions influences the thermal expansion coefficient, as reported by Karunaratne et al. [216]. They discovered that Ni-alloys with increased quantities of Mo exhibited lower coefficients values. Further investigation is needed to understand the correlation between the thermal expansion coefficient and microstructure. Figure 17 shows the variation of the linear thermal expansion coefficient with temperature for several Ni-alloys, which increased by an average of 25% (or 3.14×10^{-6} m/m) between RT and 810 °C.

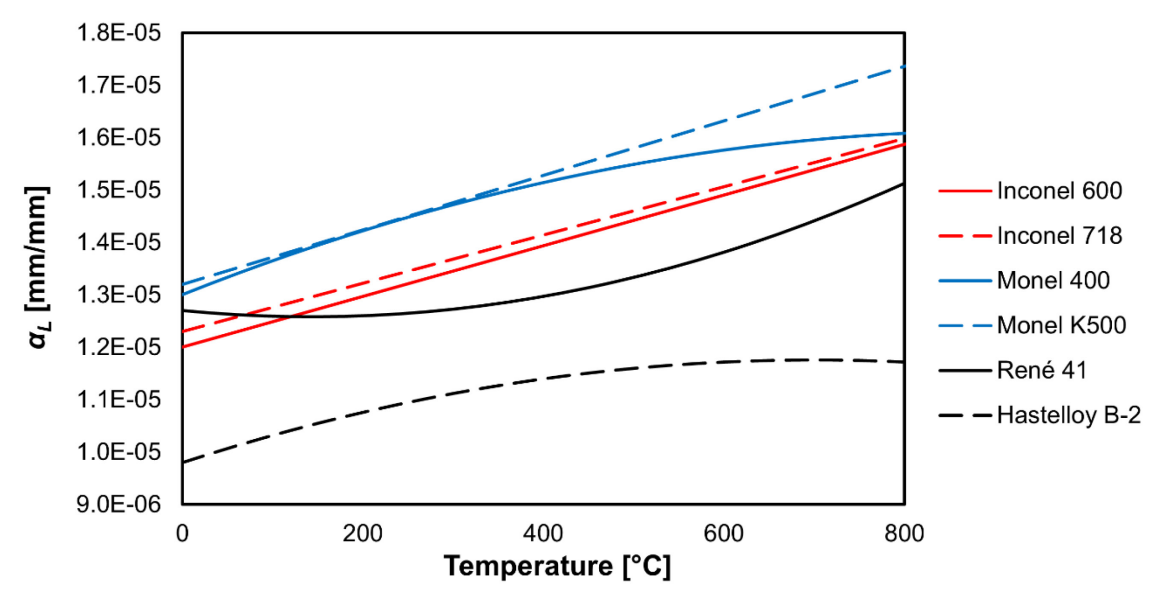


Fig. 17. Variation of the linear thermal expansion coefficient with temperature for several Ni-alloys. Curve fit data from [206-212].

The specific heat (c_p) of a material is the amount of heat energy per unit mass required to increase the temperature by one heat unit [217]. Like most other physical properties, the specific heat is temperature dependent. The fluctuation of the specific heat can be detected in the solid-liquid ranges in metals during rapid cooling and heating, and thus can be used to partially determine the state of a material's microstructure [217]. However, this claim requires further validation. Figure 18 shows the variation of the specific heat with temperature for several Ni-alloys, which increased by an average of 46% (or 194 J/kg*K) between RT and 810 °C.

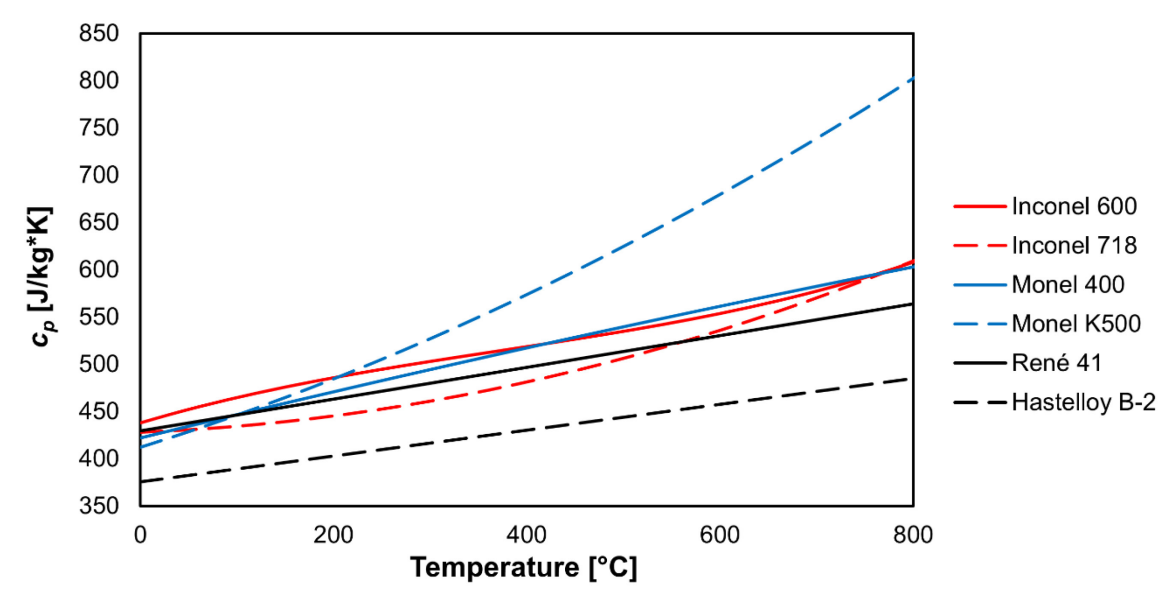


Fig. 18. Variation of specific heat with temperature for several Ni-alloys. Curve fit data from [206-212].

Thermal diffusivity (α_T) is the rate at which a material diffuses its thermal energy [217]. It is an important parameter because it serves as a ratio for most of a material's thermomechanical properties [218] and is given by:

$$\alpha_T = \frac{\lambda}{\rho c_p} \tag{35}$$

where λ is the thermal conductivity, ρ is the density, and c_p is the specific heat. By equation 35, it becomes obvious that the thermal diffusivity can be used to calculate other thermomechanical properties. Parker et al. [219] used this relation in their flash method experiment to obtain the thermal conductivity. The thermal diffusivity can be calculated experimentally, such as using the thermal-wave-mirage technique, which employs an optical beam to deflect the thermal features of a material to create a thermal deflection profile [220, 221]. Figure 19 shows the variation of the thermal diffusivity with temperature for several Ni-alloys, which increased by an average of 50% (or 1.79×10⁻⁶ m²/s) between RT and 810 °C.

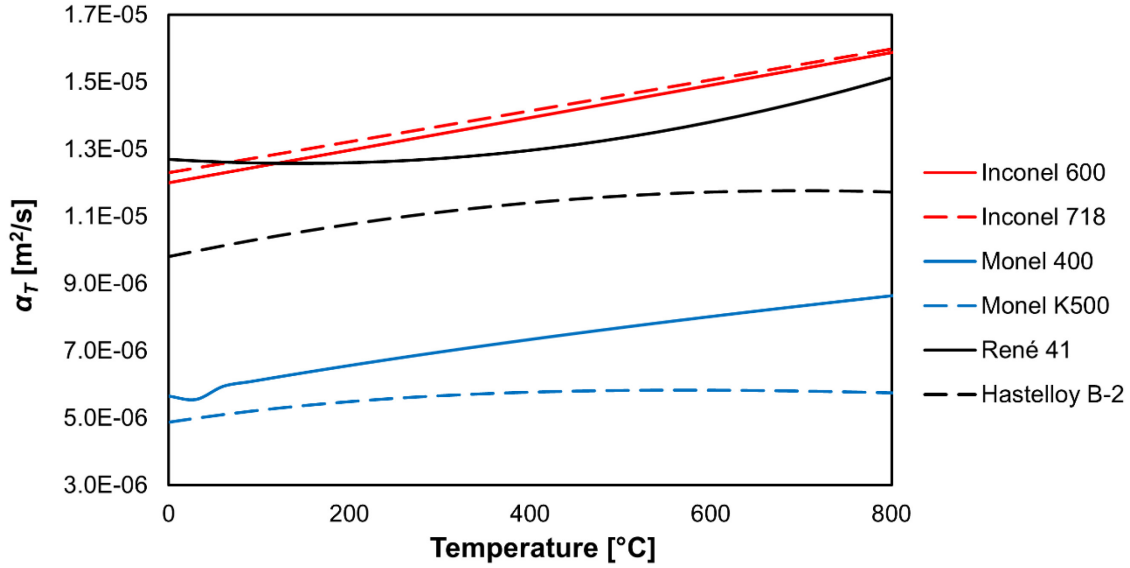


Fig. 19. Variation of thermal diffusivity with temperature for several Ni-alloys. Curve fit data from [206-212].

5.1.2. Temperature Dependence of Density

Temperature variance in Ni-alloys creates a notable change in the material density. In performing experiments on Inconel 600 using pushrod dilatometry, differential scanning calorimetry, and the laser-flashing technique, Blumm et al. [100] discovered a decrease in density because of an increase in volume due to a rise in temperature. Using the same curve fitting technique as in Section 4.1.1, the thermal density and volumetric expansion profiles for Inconel 600 were plotted in Fig. 20. The results coincide with the plot obtained by Blumm et al. [100].

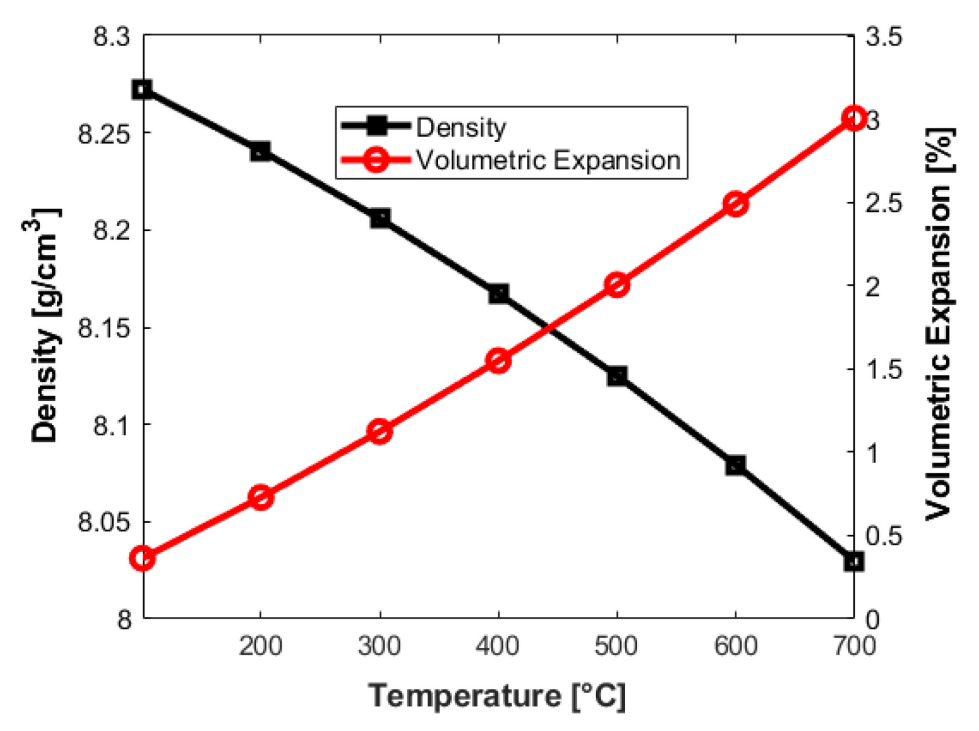


Fig. 20. Density and volume as a function of temperature for Inconel 600

To compute density as a function of temperature (as shown in the figure), the authors first developed an equation for the change in volume using the thermal expansion coefficient and temperature displacement:

$$\frac{\Delta V}{V} = 3(\alpha_L \Delta T) + 3(\alpha_L \Delta T)^2 + 3(\alpha_L \Delta T)^3$$
(36)

where $\frac{\Delta V}{V}$ is the volumetric expansion, α_L is the linear thermal expansion coefficient, and ΔT is the temperature displacement. The density as a function of temperature is then given by:

$$\rho = \frac{\rho_0}{\left(1 + \frac{\Delta V}{V}\right)} \tag{37}$$

where ρ is the density, ρ_0 is the density at RT, and $\frac{\Delta V}{V}$ is the volumetric expansion from equation 36. Valencia et al. [217] determined a similar equation, except the denominator is cubed in their formulation. By integrating equation 37, another relation

that allows for density displacement to be written as a function of temperature was developed:

$$\Delta \rho = \rho_0 \ln \left(1 + \frac{\Delta V}{V} \right) \tag{38}$$

where $\Delta \rho$ is the density displacement, and ρ_0 and $\frac{\Delta V}{V}$ are the same as before. Equation 38 is analogous to the computation of true strain.

When machining a material, the Péclet number (Pe) must be determined to fully understand the thermal behavior of the material. Density is proportionally linked to the Pe number and other thermal properties through equation 44 (The Pe number is discussed more in the following section). Using equation 37, the thermal diffusivity can be rewritten as equation 39, which can compute a slightly more precise value for the Pe number.

$$\alpha_T = \lambda \frac{1 + \frac{\Delta V}{V}}{\rho c_p} \tag{39}$$

Materials such as Inconel 718 can heat up to ~1000 °C in aeroengine applications. Since Inconel 718 has a high linear thermal expansion coefficient, it expands rapidly as the temperature increases. This in turn increases the volume, resulting in the density decreasing [100, 217]. Figure 21 displays density as a function of temperature for both Inconel 600 and Inconel 718, which was created by first computing the volumetric expansion via equation 36. Using the volumetric expansion, the density at each temperature was calculated via equation 37. By taking several iterations, the points were plotted with a curve-fit in MATLAB. This procedure was also partially repeated for the other seven Ni-alloys discussed in Section 5.2 to find the

average density change when going from RT to 800 °C, which was 4%. The change in density due to temperature also affects the Pe number and other thermal properties as well, so not considering this effect would have a major influence on constitutive model predictions.

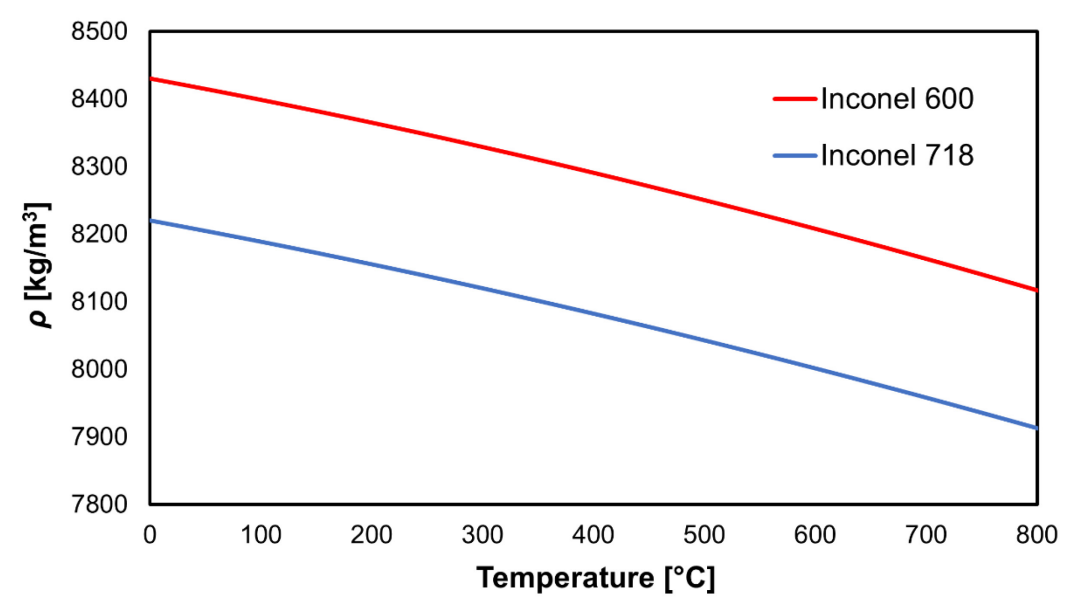


Fig. 21. Density of Inconel 600 and Inconel 718 as a function of temperature

5.1.3. Incorporating Thermophysical Properties in Constitutive Models

A clear drawback of not only phenomenological constitutive (mechanical response) laws like the JC model but also physics-based laws like the ZA model is that they do not explicitly consider thermophysical properties such as the thermal conductivity, density, specific heat, etc. as variables in their equations. As was just illustrated in Sections 5.1.1 and 5.1.2, thermophysical properties change considerably with temperature, and thus have a causal influence on the thermomechanical response of the material as well—it has been shown that these properties are just as influential with respect to temperature as the flow stress or friction between tool and chip [222].

For example, a reduced thermal number (i.e., the Pe number; a reduction in the ratio of cutting speed to thermal diffusivity) at elevated temperature would likely promote adiabatic shear localization, thus changing the mode of plastic deformation. The inability of the workpiece to dissipate heat at high speeds will localize the heat at the PDZ, which will generate serrated formation and create a considerably different constitutive response than with continuous chip formation. A higher linear thermal expansion coefficient at elevated temperature would mean that the material is more susceptible to thermal damage such as tensile residual stress, which is very harmful to fatigue life [223]. Effects such as these are what are lacking in conventional constitutive models that do not account for second order thermophysical property interactions.

Nieslony et al. [224] performed AdvantEdge simulations to analyze the influence of temperature dependence in thermophysical properties using the Power Law constitutive model. They compared the numerical results obtained using thermophysical values in the FE database (which are assumed to be constant) with the results obtained using constants by Kalhori [225], which were calibrated by modeling the temperature dependence of several thermophysical properties:

$$\lambda(T) = \lambda(\lambda_0 + \lambda_1 T + \dots + \lambda_5 T^5) \tag{40}$$

$$c_p(T) = c_p(c_{p_0} + c_{p_1}T + \dots + c_{p_5}T^5)$$
(41)

$$\alpha(T) = \alpha(\alpha_0 + \alpha_1 T + \dots + \alpha_5 T^5) \tag{42}$$

where compare $\lambda(T)$ is the thermal conductivity, $c_p(T)$ is the specific heat, and $\alpha(T)$ is the linear thermal expansion coefficient at different temperatures. The model by Kalhori [225] showed excellent agreement with measured cutting forces and temperature,

whereas the model utilizing constant physical properties was shown to greatly overestimate these values. Regarding the output of FE simulations, the changes in the thermal conductivity and specific heat in Kahlori's [225] caused significantly lower temperature distributions along the isotherms of the tool rake face [224]. Thus, future modeling efforts should consider incorporating thermophysical variables into their constitutive frameworks.

One such model that accounts for thermophysical properties is the semianalytical Eager-Tsai model. Hariharan et al. [226] studied the microstructural evolution during laser powder bed fusion (LPBF) of Ni-alloy Haynes 282, and they used the Eager-Tsai model to simulate the thermal field generated during LPBF, which can be seen below:

$$T(x, y, z) = T_0 + \frac{\eta_0 P}{\rho c_p \sqrt{4\pi^3 \alpha_T}} \int_{\tau_0 = 0}^{\tau_i = t} \frac{exp\left[-\frac{(x + v\tau)^2 + y^2}{2\sigma^2 + 4a\tau} - \frac{z^2}{4a\tau}\right]}{(\sigma^2 + 2a\tau)\tau^{1/2}} d\tau_i$$
(43)

where T_0 is the reference temperature, η_0 is the efficiency of energy absorption, P is the laser power, ρ is the density, c_p is the specific heat, α_T is the thermal diffusivity, v is the scan speed, x, y, z represent position with respect to the heat source, τ_i is the time integration variable, σ is the standard deviation of Gaussian profile, and τ represents the available time for conduction. Not only is the Eager-Tsai model significantly faster than FE thermal models, but it has the ability to re-use solutions without having to recalculate with each iteration [226]. Such a useful model integrates thermophysical properties to speak to the dynamic physics of a material and can result in more complete simulations. Since the model is semi-analytical, it can also be calibrated with experimental data.

5.2. Semi-Analytical Comparison of Thermal Damage Sensitivity in Ni-alloys

This section discusses thermomechanical properties related specifically to machining. A useful metric for comparing the thermal response of workpiece materials during cutting processes is provided by the Pe number, or thermal number, of the tool/workpiece contact. It is a dimensionless number that is given by the ratio between the flow and diffusion rates, which in cutting may be interpreted as the relative speed of thermal conduction compared to the cutting speed of the tool on the workpiece surface:

$$Pe = \frac{v_c a \rho c_p}{2\lambda} \tag{44}$$

where v_c is the cutting speed, a is the half-width of contact, and ρ , c_p , and λ are the same as before. The Pe number determines the shape of the thermal field within the workpiece material, which may be quasi-static (approximately symmetrical about the center of the thermal contact area) or transient (with the peak/flash temperature moving towards the trailing edge of the tool/workpiece contact on the tool's flank face) [227]; this concept is illustrated in Fig. 22.

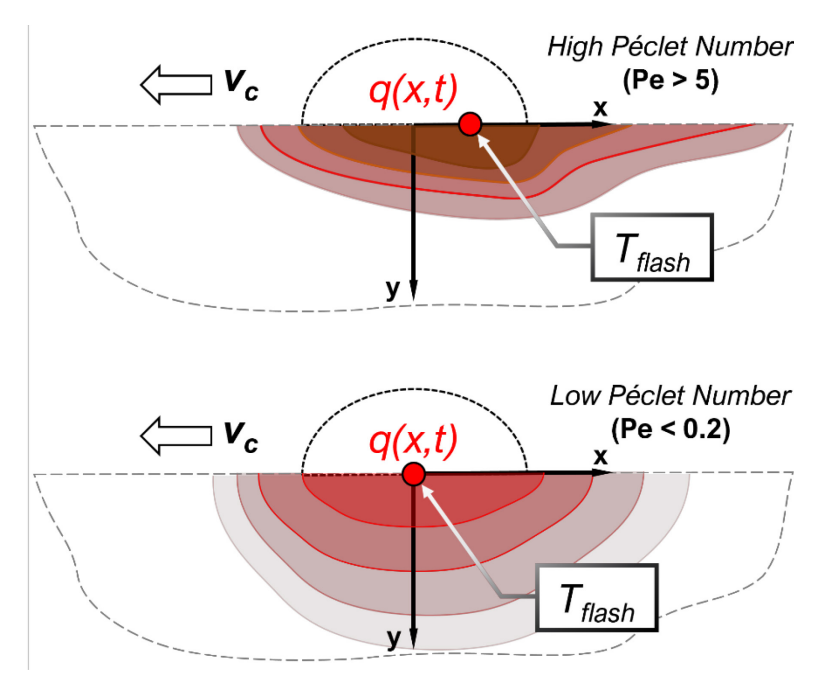


Fig. 22. Péclet number influence on thermal field [228]

In the context of machining, thermal damage due to thermal expansion stresses that exceed the YS of the workpiece material is an important consideration. Such thermal damage may exhibit itself as undesirable tensile residual stress, which may significantly reduce fatigue life, or the presence of thermal cracks, when the thermal expansion stress exceeds the ultimate tensile strength (TS). The critical temperature (CT) can be found by computing the equivalent thermal expansion stress and plotting it with the YS as a function of temperature.

The CT is the temperature at which the equivalent thermal expansion stress exceeds the YS (causing plastic deformation) and where a tensile residual stress begins to form. It is unique for each workpiece material, allowing for qualitative comparisons of sensitivity to localized thermal expansion. The tensile residual stress is approximately equal to the difference between the equivalent thermal expansion stress and the YS (once the equivalent thermal expansion stress has surpassed the YS; before this point,

the tensile residual stress is zero). Due to thermal softening, the YS decreases with increasing temperature while the equivalent thermal expansion stress increases with thermal loading. This process was used to characterize the thermal stress profile for various Ni-alloys (shown as Figs. 23-31) by plotting the evolution of YS, thermal expansion stress, and resulting thermally induced tensile residual stress.

The YS curves were created by curve fitting values from material datasets in MATLAB (the polynomial functions are shown on each respective figure). The equivalent thermal expansion and thermally induced tensile stresses were computed via the model by Schoop et al. [228] (shown in blue and red on the figures, respectively). This model implies that once the tensile residual stress surpasses the equivalent thermal stress, cracks and tears begin to nucleate on the surface of the component. It should be noted that the increase in temperature with increasing cutting speed is very complicated, due to the presence of various heat sources (primary and tertiary shear zones, tool/workpiece friction, etc.).

Inconel 600 is a popular Ni-alloy used in aero-engine, nuclear, and medical applications due to its creep resistance, corrosion resistance, high toughness, high strength, and high stiffness [229, 230]. Like Inconel 718, it is also difficult to machine, particularly because of the emergence of tensile residual stresses. As can be seen in Fig. 23, the CT is ~175 °C, which lends credence to the material being difficult to machine.

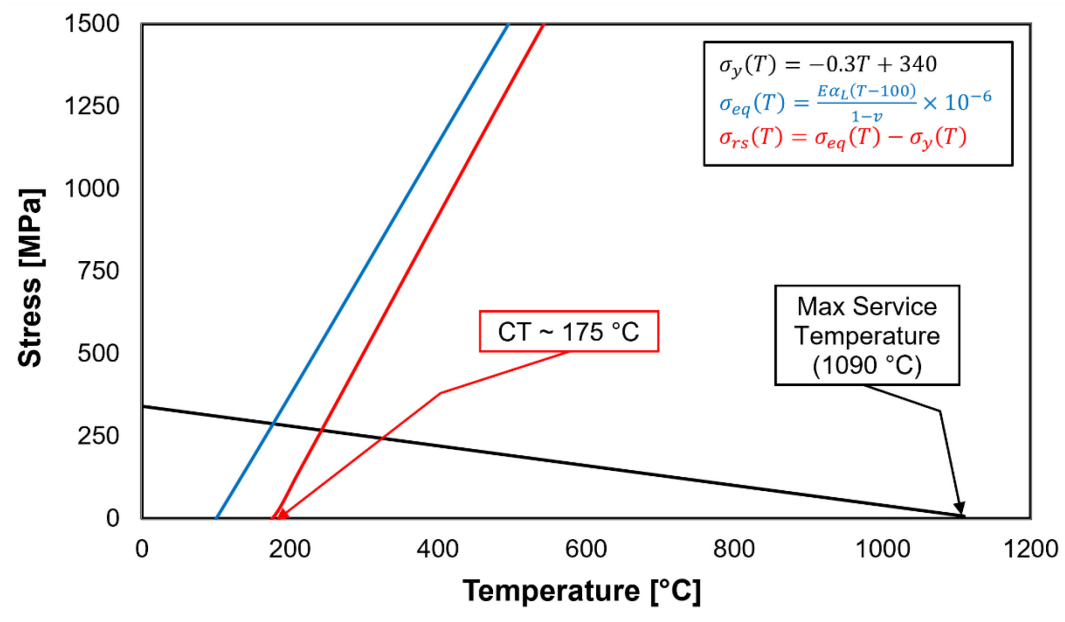


Fig. 23. Thermal residual stress profile for Inconel 600. YS curve fit data from [210].

Inconel 625 is another Ni-alloy with exceptional properties like high YS, creep strength, fatigue strength, oxidation resistance, and corrosion resistance [231]. Typical applications include heat shields, gas turbine engine ducting, and seawater applications [232, 233]. The CT for Inconel 625 is ~230 °C (see Fig. 24), signifying that it has a superior yield and TS to Inconel 600, and that it is slightly easier to cut.

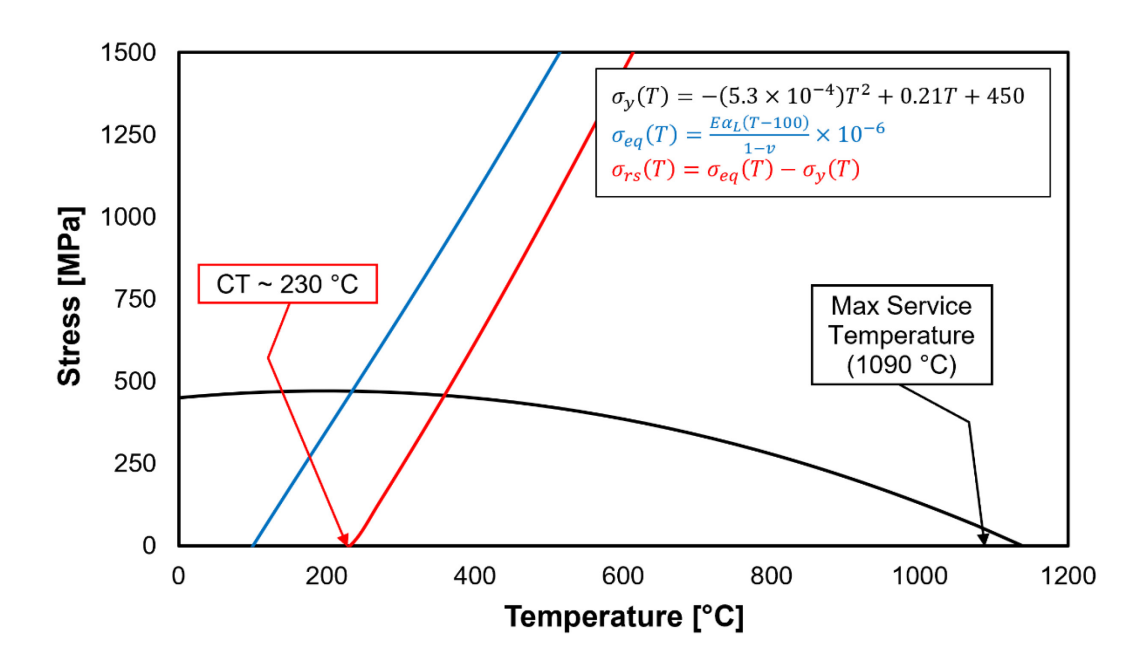


Fig. 24. Thermal stress profile for Inconel 625. YS curve fit data from [233].

Inconel 718 is by far the most utilized Ni-alloy for aerospace applications. Like Inconel 600 and 625, the Ni and Cr percentages provide great resistance to carburization, oxidation, and corrosion along with a high fatigue and TS [234]. Inconel 718 also has great mechanical properties at cryogenic temperatures [235], which is a rare characteristic. The CT for Inconel 718 is very high at approximately 400 °C (see Fig. 25), which translates to good thermal stress resistance [236]. This makes Inconel 718 relatively much easier to machine than Inconel 600 and 625. It has a low thermal conductivity [237] and is very adhesive, which causes significant tool wear. This especially becomes a problem at high cutting speeds and feed rates [238].

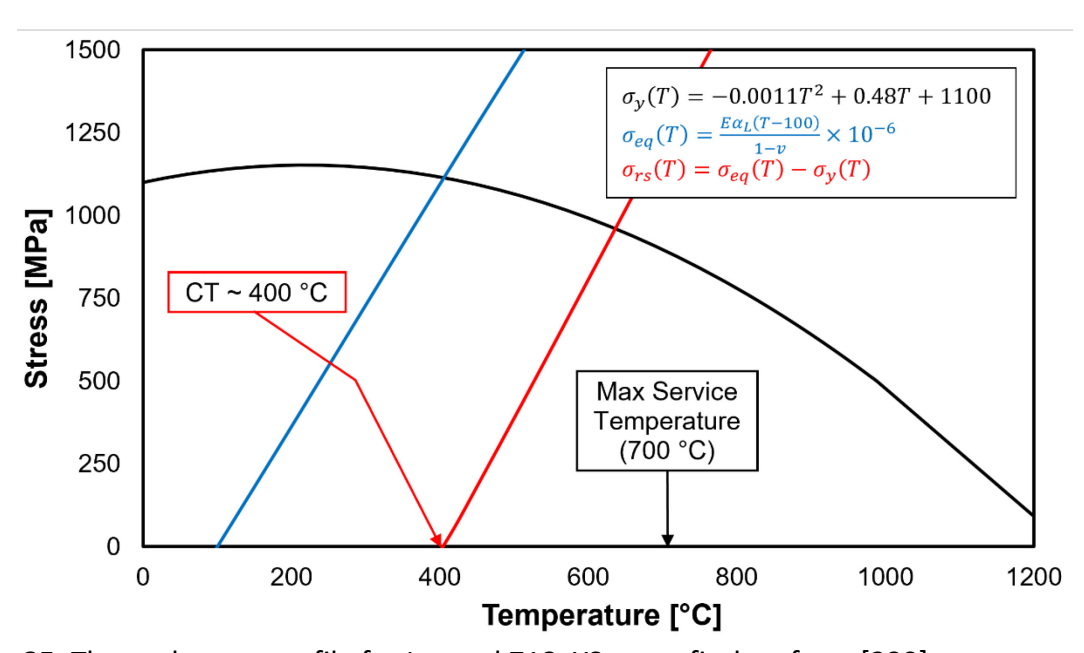


Fig. 25. Thermal stress profile for Inconel 718. YS curve fit data from [239].

Incoloy 825 is a Ni-alloy with high corrosion resistance but low strength and hardness [240]. It has many applications in the aerospace, oil, and power industries [241]. Typically, alloys with Ni, Cr, and Mo are costly, but Incoloy 825 is inexpensive due

to the decreased Ni content [242]. As can be seen in Fig. 26, the YS of Incoloy 825 is low, which contributes to its low CT. Despite this, its maximum service temperature remains high due to its high corrosion resistance at elevated temperatures [206]. When machining Incoloy 825, chemical vapor deposition (CVD) multilayer coated (TiN/TiCN/Al₂O₃/ZrCN) inserts have been found to produce a better surface finish at high cutting speeds and a decrease in work hardening at low-medium cutting speeds [33]. Use of an uncoated tool results in an increase of white layer formation and work hardening [33].

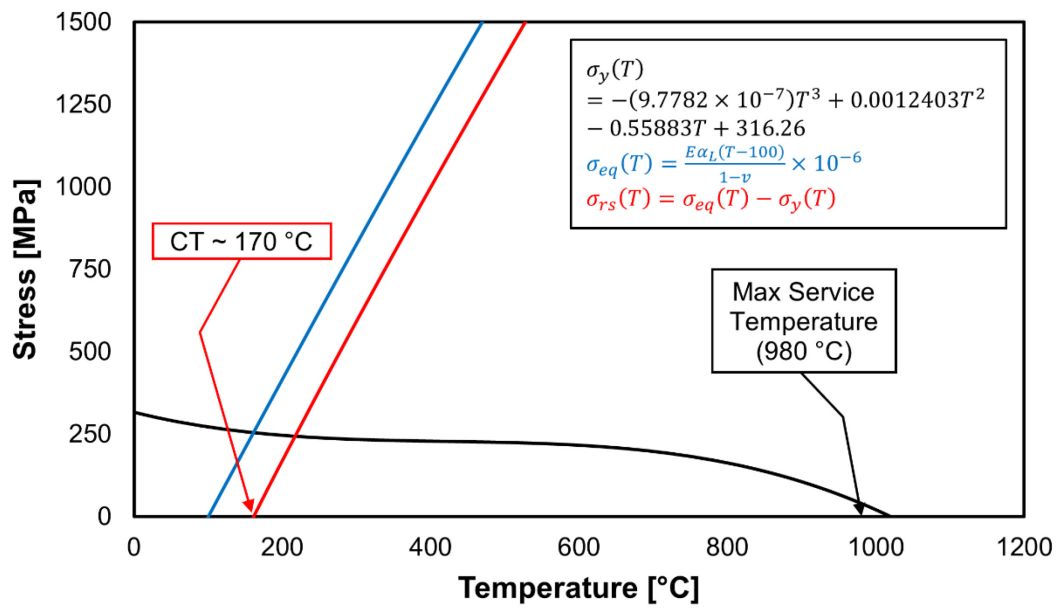


Fig. 26. Thermal stress profile for Incoloy 825. YS curve fit data from [243].

Monel K500 has a high thermal conductivity, specific heat, and thermal expansion coefficient, but low thermal diffusivity [56]. It has high strength, fracture toughness, and is corrosion resistant in marine environments, but is susceptible to hydrogen environment-assisted cracking [244, 245]. Research shows that machining Monel K500 at high cutting speeds gives a better surface finish and that a low to

moderate feed rate with a small nose radius minimizes tool wear [246]. Figure 27 shows that Monel K500 has an acceptable CT.

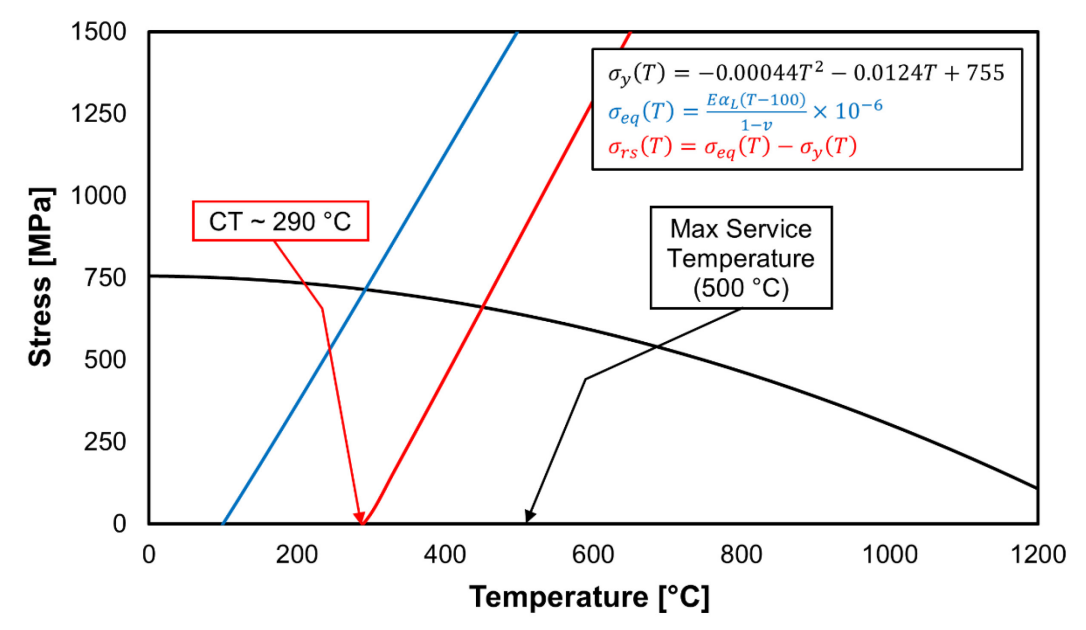


Fig. 27. Thermal stress profile for Monel K500. YS curve fit data from [208].

René 41 is an older Ni-alloy developed in the 1950s with high strength, great corrosion and oxidation resistance, great microstructural stability for up to 980 °C [247]. It has been used in nozzles, the hot sections of engines, and more [64]. However, the use of René 41 is limited due to strain age cracking during welding and heat treatment [248]. In welding, cracks form from weakened grain boundaries due to oxygen absorption, and there is decreased ductility [249]. As can be seen in Fig. 28, René 41 has a high and consistent YS, giving it a relatively high CT. There have since been developments for more effective René alloys such as René 180, but data on such alloys is not readily available.

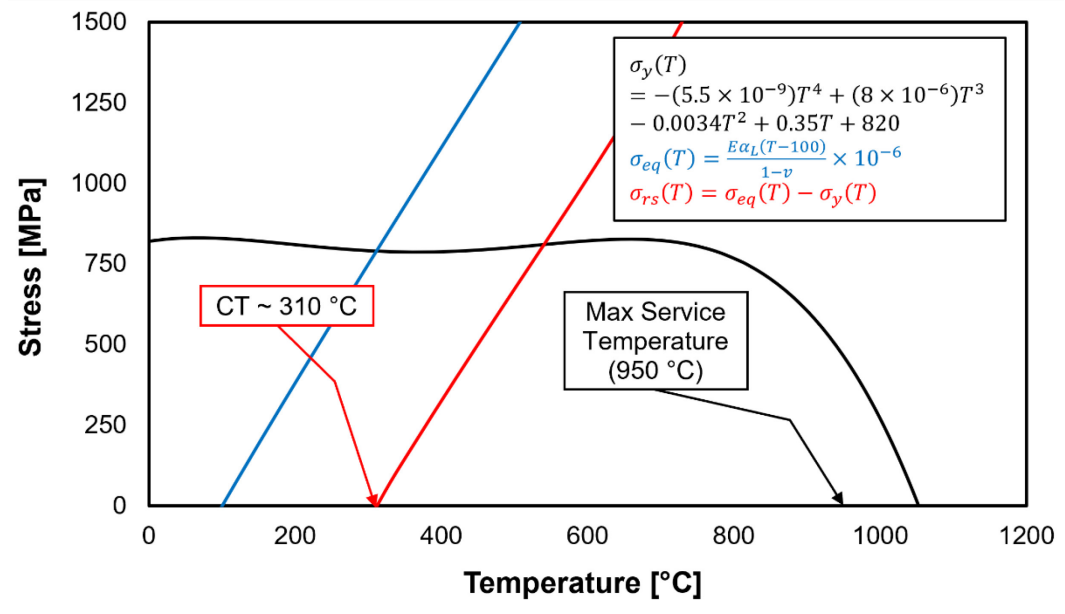


Fig. 28. Thermal stress profile for René 41. YS curve fit data from [209].

Hastelloy B-2 is an alloy with a particularly high Mo percentage and subsequently high corrosion resistance in acid environments. It is used in pipes, pumps, and reactors [250]. However, Hastelloy B-2 may become brittle if exposed to temperatures at 500-850 °C or while cooling from an elevated temperature [251]. This implies that as the temperature drops, the hardness/brittleness rises with the alloy's strength [252]. This embrittlement can be averted by avoiding prolonged heating in the material by cooling it rapidly after the annealing process to avoid additional phases [253]. The work hardening in Hastelloy B-2 is due to the high percentage of Mo, which means that quantities of this element should be limited [250]. From Fig. 29, it is shown that Hastelloy B-2 has a lower CT than René 41 and Inconel 718, but higher than Inconel 600, 625, and Incoloy 825. Nonetheless, Hastelloy B-2 is difficult-to-machine due to its excessive work hardening.

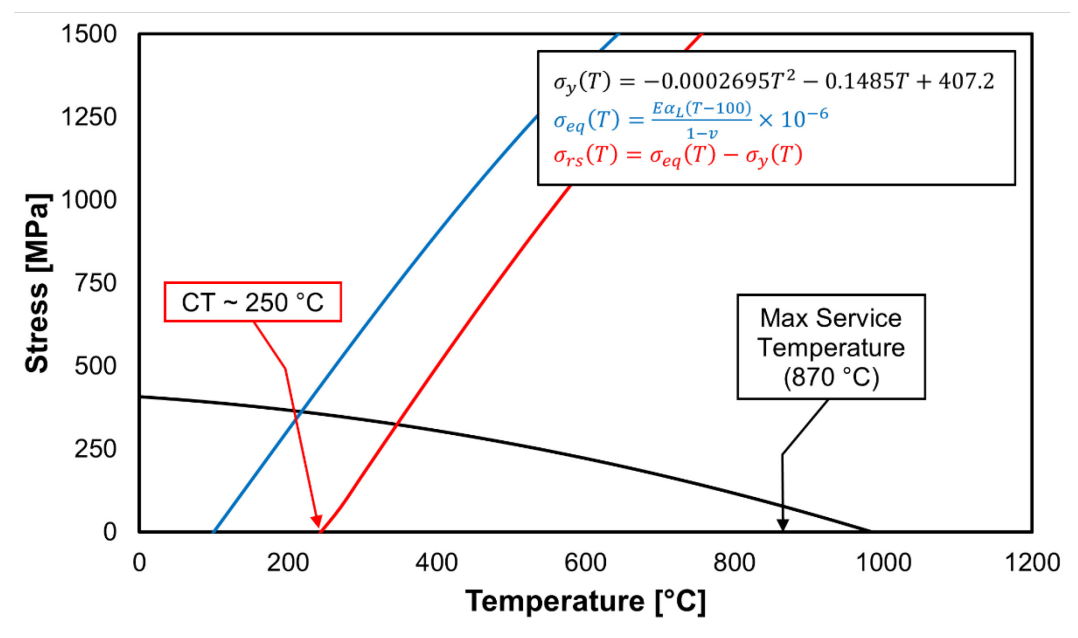


Fig. 29. Thermal stress profile for Hastelloy B-2. YS curve fit data from [254].

Hastelloy X has high fatigue strength, corrosion resistance, and oxidation resistance at elevated temperatures. It is used in jet engines, afterburners, and tailpipes [255]. However, Hastelloy X is difficult to weld and machine. For instance, the Cr precipitation produces dynamic strain aging [256]. Another problem is solidification and liquidation cracks due to the forced separation of Mo and Cr rich elements at the end of the solidification process [257]. As can be observed from Fig. 30, it has a low CT—thus, tensile stresses are more likely to occur. Moreover, low cutting speeds and feed rates should be employed.

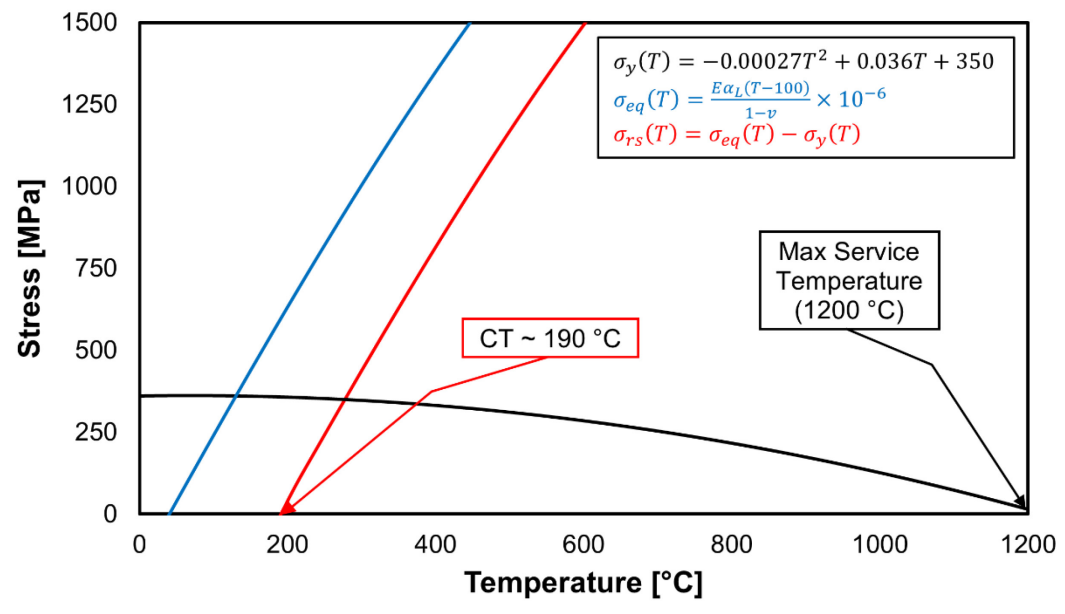


Fig. 30. Thermal stress profile for Hastelloy X. YS curve fit data from [258].

Haynes 230 is a high thermal strength, corrosion resistant alloy [259]. It is used in gas turbines and solid-oxide fuel cells [260]. It possesses elevated temperature strength, great oxidization and nitridation resistances, high formability, and weldability along with long-term thermal stability [261]. The carbon in Haynes 230 allows for it to have a solid-solution and be carbon-strengthened which, unlike other Ni-alloys, maintain its mechanical properties at exceedingly high temperatures [261]. Figure 31 shows that Haynes 230 has a low CT and YS, which makes it difficult to machine. Thus, low feed rates and high cutting speeds are recommended.

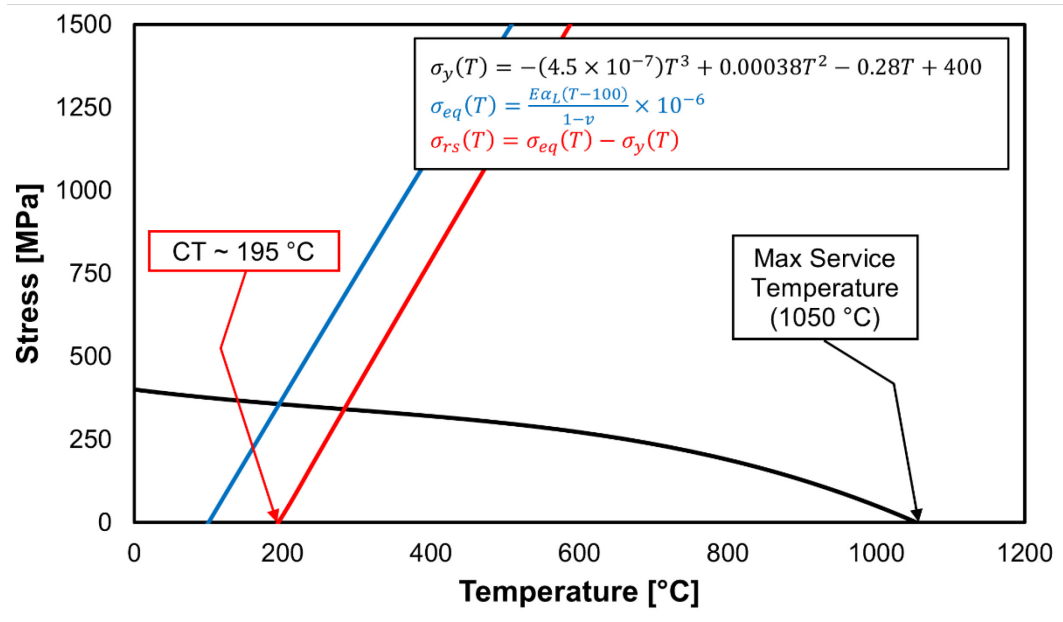


Fig. 31. Thermal stress profile for Haynes 230. YS curve fit data from [262].

As can be seen in the above plots, the tensile residual stress is induced when the equivalent thermal expansion stress surpasses the YS of the material—resulting in permanent deformation. This occurs at the CT, which is summarized for each alloy in Table 12. Not shown in Figs. 23-31 is the TS from RT to the maximum service temperature (MST), so this information is provided in Table 12 for each alloy alongside the CTs. The TS values were computed using the same technique for the YS in Figs. 23-31. The model used can explain the effects of thermal stress due to the thermal properties of the cutting speed, half-width of contact, tool width, and the thermal properties on a material being cut [227].

As can be seen, there are significant differences between the various Ni-alloys regarding their CT and TS at RT, implying unique machining responses. Notably, Inconel 718 has the highest CT at approximately 400 °C, while most other alloys feature CTs in the range between 170-310 °C. Thus, the data in Table 12 suggests that most Ni-alloys

are relatively susceptible to thermally induced damage (tensile stress and surface cracks), which is consistent with practical and experimental observations. Increasing the CT (e.g., via decreased thermal expansion coefficient or increased high-temperature YS) could offer improved resistance to 'abusive machining' and should be pursued in future integrated computational and experimental materials engineering (ICEME) efforts.

Table 12. CT and TS at key temperatures for various Ni-alloys

Ni-alloy	СТ [°С]	TS at RT [MPa]	TS at 600 °C [MPa]	TS at MST [MPa/°C]
Inconel 600	175	804	488	60/1090
Inconel 625	230	952	707	128/1090
Inconel 718	400	1555	1218	988/700
Incoloy 825	170	697	493	75/980
Monel K500	290	1075	501	696/500
René 41	310	1256	1251	893/950
Hastelloy B-2	250	966	725	605/870
Hastelloy X	190	788	569	28/1200
Haynes 230	195	865	700	43/1050

The MST represents the highest temperature at which a material can operate without significant changes to its material properties. For most of the Ni-alloys discussed, the MST falls around 1000 °C. The MST should not be mistaken for the CT, which represents the nucleation of thermally induced stress concentrations (tensile residual stresses) in a component. Rather, the MST is the resulting failure of said component via thermal stress concentrations. Another important observation is that for several of the Ni-alloys, the MST occurs when the YS becomes approximately zero. This implies that the reported MST values are likely not intended to be used for structural (e.g., turbine disc) service and components, but rather the maximum temperature at which the material could safely be used without suffering severe oxidation or creep.

Notably, the MST falls within the range of typical machining temperatures, particularly in the primary and secondary deformation zones. This again emphasizes that the unique high-temperature properties of Ni-alloys make them uniquely difficult-to-cut, and future work should investigate novel cutting tool materials that feature even greater resistance to temperatures (e.g., nanocrystalline ceramics and polycrystalline boron nitride materials).

5.2.1. Models for Capturing the Temperature Dependence of Stress

As can be seen from the thermal profiles in Section 5.2, temperature has a significant effect on the various stresses of Ni-alloys; not many models can accurately predict the flow stress at extremely high temperatures (1000 °C). This section will briefly discuss some of the more recent approaches for characterizing flow stress in this regime. One such method is the Garofalo-Arrhenius (G-A) creep model, which is used for predicting material behavior in the hot deformation of metals [263, 264]. The G-A is especially useful because it utilizes the hyperbolic sine function (equation 45) from Garofalo [265], which allows it to predict stress at all levels, unlike the power and exponential law versions of the Arrhenius model.

$$A[\sinh(\alpha\sigma)]^n \tag{45}$$

where A, α , and n are constants that are a function of strain to be calculated via linear regression analysis [263] and σ is the flow stress at any level, according to Garofalo [265]. Zener and Hollomon [266] introduced a stress-strain relation that could be established with one parameter considering the strain-rate and the diffusion-rate (which incorporates material properties):

$$Z = \dot{\varepsilon} \exp\left(\frac{Q}{RT}\right) \tag{46}$$

where R is the universal gas constant, T is the temperature, and Q is the deformation activation energy that characterizes the micro-movements influencing the strain hardening and thermal softening of a material. Equating equations 45 and 46 to each other and isolating σ gives the flow stress as a function of strain, strain rate, and temperature:

$$\sigma(\varepsilon, \dot{\varepsilon}, T) = \frac{1}{\alpha} \sinh^{-1} \left[\dot{\varepsilon} \left(\frac{\exp(\frac{Q}{RT})}{\exp\left[\ln\left(\frac{A}{S^{-1}}\right)\right]} \right)^{\frac{1}{n}} \right]$$
(47)

The G-A creep model is known for its accurate measurements of flow stress at elevated temperatures surpassing 70% of the material's melting temperature. Zuo et al. [263] compared the G-A model with an artificial neural network (ANN) to predict the flow stress of Ni-alloy N08028 between 1100 °C and 1200 °C. Since ANNs are used to predict patterns in human behavior and decision making, the case could be made for harnessing them to predict material behaviors such as the flow stress [267]. Backpropagation ANN (B-P ANN) methods are the most capable for engineering applications [268]. B-P ANN models have three layers: the input layer, the output layer, and other hidden layers [269]. The input layers predict the output layers and validated target data is then used to propagate the errors backwards to optimize the constants. The purpose of the study by Zuo et al. [263] was to determine whether changes to the initial microstructure, as the result of hot deformation testing, was a determinant of flow stress.

Zuo et al. [263] used strain, strain-rate, temperature, and the initial microstructure as the input layer and flow stress as the output layer. They were able to utilize the B-P ANN model to get a more accurate prediction of flow stress than the G-A creep model, namely because the BP-ANN model accounts for microstructural effects like the phase changes that come with the rise in temperature whereas the G-A does not incorporate microstructural effects. This once again points back to the advantages of physics-based models and shows the potential for using ANNs in the modeling of machining processes.

6. CONCLUSION

This review provides and summary of advances in the constitutive modeling and physical properties of Ni-alloys used in turbine applications, with a focus on machining-specific thermomechanical regimes. Some of the key findings of this study include:

- While the widely used JC model is simple to calibrate, MJC models can account
 for physically relevant factors like strain softening and second-order
 interactions. The biggest challenge with the basic JC model is that it is often
 inaccurate at higher strain rates, which tend to characterize cutting processes.
- While 2D FE software is most commonplace for machining simulations, some
 authors argue that the orthogonal plane strain assumptions of such 2D models
 do not represent the triaxiality of stress found in most industrial cutting
 processes. Thus, these researchers argue that only 3D FE is suited for physics-based modeling machining applications.

- When plotting various JC models from literature, the plots did not resemble a
 typical stress-strain curve on that strain domain, even when the models were
 calibrated using the SHPB test. Consequently, there is an urgent need for
 machining-specific materials characterization techniques that cover the strain,
 strain rate, and temperature regimes of machining.
- The alternative to using data from mechanical tests like tensile and quasi-static compression and SHPB experiments, is direct calibration using the inverse method with orthogonal machining tests. Unlike the SHPB tests, for instance, the inverse method relies on in-situ machining data where the strains and temperatures are representative of the actual process. Constants can then be calibrated with optimization algorithms by comparing measured cutting forces and chip thicknesses to those predicted by analytical models. A novel approach to the inverse method is DIC, which is allows for the strain and strain rates in the PDZ to be determined with high accuracy, which shows great potential for constitutive model calibration.
- Phenomenological models cannot be relied on exclusively given their lack of
 consideration for microstructural behavior. Physics-based models do address
 this, by incorporating phenomena like grain dislocations and phase
 transformations, which have a major effect on the material response in
 machining regimes. However, physics-based models come with their limitations,
 such as only accommodating single-crystal materials and difficult calibration due

- to the number of constants. Thus, it phenomenological models may prove to be more appropriate for certain materials.
- The boundary conditions of rake angle, cutting speed, and tool coating can all
 drastically change the output of FE simulations. It has been shown that the rake
 angle alters the chip morphology and yields better flow stress predictions when
 it is zero. Raising the cutting speed leads to serrated chip formation, higher
 cutting forces, and higher cutting temperature. Tool coating can also suppress
 the temperature at the cutting area.
- The chemical composition of Ni-alloys has a significant effect on their service
 performance. For instance, the high Ni and Cr percentages can provide great
 resistance carburization, oxidation, and corrosion. Most phenomenological
 models neglect chemical effects, and even physics-based material models often
 oversimplify the effects of chemistry and inclusions.
 - Little work has addressed the impact of physical properties on the constitutive response of Ni-alloys. Many studies treat these properties as either constant or not mutually interconnected when they are temperature-sensitive and codependent on each other. Furthermore, neither phenomenological nor physics-based models treat these properties as functions as temperature, which is undoubtedly affecting the accuracy of predictions. This study showed via regression modeling of material property data that a change from RT to a machining-specific regime of 810 °C, λ , α_L , c_p , and α_T were shown to increase by an average of 115%, 25%, 46%, and 50%, respectively.

- Of the Ni-alloys analyzed, the density was found to decrease by an average of 4%, which directly affects other properties such as the thermal diffusivity.
 Moreover, thermophysical properties also have a direct impact on aspects like work hardening, adhesion, and cracking, which is why their temperature dependence needs to be considered in constitutive modeling.
- As was observed from the modeled thermal stress profiles, the critical
 temperature CT of Ni-alloys, beyond which tensile residual stress is induced due
 to localized heating, is well below typical cutting temperatures experienced in
 machining or (bulk) service temperatures for these alloys. This finding implies
 that Ni-alloys require especially careful selection of feeds and speeds, as well as
 tailored cooling and lubrication strategies to avoid undesirable near-surface
 tensile residual stress.

7. OUTLOOK AND DIRECTIONS FOR FUTURE WORK

Modeling of the machining-specific material response of Ni-alloys is a highly challenging task. First, selecting a constitutive model and associated parameters from the plethora of available (previously calibrated) models requires a careful understanding of how each model was calibrated, and on what basis it was considered a reasonable representation of the 'true' constitutive response of a given Ni-alloy. This review shows that many, if not most, available JC models do not correlate well with experimentally measured stress/strain response of Ni-alloys. The key problem lies in the determining the value of flow stress at high values of strain, which occur in machining but cannot currently be replicated using available characterization techniques, such as the SHPB

test. By relying on substantial extrapolation, often over an order of magnitude beyond available data, the predicted flow stress at high strain, as well as high strain rates and elevated temperatures, often does not correlate with established experimental data.

In addition to adopting physics-based models, the experimental characterization method for determining the material constants (i.e., model calibration) is just as important. The SHPB has already been established to lack the ability to replicate the intensive thermomechanical regimes in machining. The authors of this work proposed that the emerging inverse method, also known as in-situ characterization, offers a promising way forward as it can capture the true thermomechanical conditions of machining processes. Recent developments towards higher resolution in-situ process characterization include high-speed optical microscopy via DIC and particle image velocimetry (PIV) techniques appear to be a promising path, perhaps realizing the longstanding vision to utilize 'machining as its own materials characterization technique'.

Notably, future work to characterize machining-specific material behavior should include the effects of microstructural factors, such as grain-scale anisotropy and effects such as DRX that have been widely incorporated in modeling research, but not yet directly observed to occur during cutting (in-situ)—there is a notable consensus in the machining community that DRX may hold the answer to the observed discrepancy between SHPB and observed SPD strain values in machining, future work should focus on addressing this scientific question. The authors also envision the development of a shared database of 'pedigreed' constitutive model parameters and

calibration/validation data for both process model performance and material properties to ensure the use of reliable and physically meaningful process model inputs. Such a database would furthermore require the utilization of in-situ characterization techniques that allow for severe plastic deformation (SPD) to be observed at high strain rate and temperature. This endeavor could be sponsored by the International Academy for Production Engineering (CIRP) to be used by academic researchers and industry practitioners [79].

Finally, this study highlights the needs for more careful consideration of temperature dependent physical properties, as these properties have a significant effect on the mode of deformation, and consequently machining performance. To date, few studies have managed to incorporate physically relevant thermal property models within machining process models. In this context, the response of Ni-alloys to localized heating (i.e., localized thermal expansion resulting in tensile yield and tensile residual stress upon cooling), will need to be explored further. Based on an improved fundamental understanding of the propensity of different Ni-alloys to be damaged and 'abused' during cutting, we envision the ability avoid these undesirable conditions through process modeling, which could ultimately enable more pro-active engineering of the surface quality of machined aeroengine components in the future.

FUNDING

The work presented in this paper was supported by the National Science Foundation under Award No. 2143806, project title "CAREER: Thermomechanical Response and Fatigue Performance of Surface Layers Engineered by Finish Machining: In-Situ Characterization and Digital Process Twin". Any opinions, findings and conclusions or recommendations expressed in this publication are those of the authors and do not necessarily reflect the views of the National Science Foundation.

1681 **NOMENCLATURE**

T Absolute temperature

 T_m Absolute melting temperature

ALE Arbitrary Lagrangian Eulerian

ANN Artificial neural network

 σ_a Athermal stress

au Available time for conduction

B-P ANN Back-propagation ANN

 σ_{th} Thermal stress

BCC Body-centered cubic

 ho_c Cell interior dislocation density

 ρ_w Cell wall dislocation density

m Constant shear friction factor

 μ_c Coulomb constant

CEL Coupled Eulerian Lagrangian

CS Cowper-Symonds

D Critical damage value

CT Critical temperature

 v_c Cutting speed

 F_c Cutting force

Q Deformation activation energy

 ρ Density

 ho_0 Density at RT

 $\Delta \rho$ Density displacement

DIC Digital image correlation

DDB Dislocation density-based

 α_d Dislocation drag coefficient

 σ_d Dislocation drag stress

DPZD Distributed primary zone deformation

Journal of Manufacturing Science and Engineering

DRV Dynamic recovery

DRX Dynamic recrystallization

 η_0 Efficiency of energy absorption

EDZ Elastic deformation zone

 ε^n Equivalent plastic strain

 σ_{eq} Equivalent thermal expansion stress

FCC Face-centered cubic

 F_t Thrust force

FE Finite element

FEM Finite element method

 μ Friction coefficient

γ Gamma

 γ' Gamma prime

 γ'' Gamma double prime

G-A Garofalo-Arrhenius

 ho_{wg} Geometrically necessary dislocation density

 h_{ht} Global heat transfer coefficient

D Grain size

a Half-width of contact

B Hardening modulus JC parameter

HDZ Heat damage zone

ICEME Integrated computational and experimental materials engineering

JC Johnson-Cook

LBPF Laser powder bed fusion

P Laser power

 α_L Linear thermal expansion coefficient

MCE Marusich's Constitutive Equation

MST Maximum service temperature

MTS Mechanical Threshold Stress

Journal of Manufacturing Science and Engineering

 h_{min} Minimum uncut chip thickness

MCS Modified Copwer-Symonds

MJC Modified Johnson-Cook

MZA Modified Zerilli-Armstrong

Pe Péclet number

PDZ Plastic deformation zone

 ε_p Plastic strain

 $\dot{\varepsilon}$ Plastic strain rate

f S Predicted shear force

h Programmed uncut chip thickness

 $\dot{arepsilon}_0$ Reference plastic strain rate

RT Room temperature

 T_0 Room temperature

v Scan speed

SDZ Secondary deformation zone

 φ Shear angle

 c_p Specific heat

SHPB Split-Hopkinson Pressure Bar

 ho_{ws} Statistical dislocation density

 σ Standard deviation of Gaussian profile

 C_2 Strain hardening coefficient

n Strain hardening JC parameter

C Strain rate sensitivity JC parameter

 σ_0 Stress for overcoming short range obstacles

 ΔT Temperature displacement

→ Thermal conductivity

TDZ Tertiary deformation zone

 α_T Thermal diffusivity

 σ_{rs} Thermally induced tensile residual stress

Journal of Manufacturing Science and Engineering

	m	Thermal softening JC parameter
	σ_G	Thermal stress
	$ au_i$	Time integration variable
	TS	Ultimate tensile strength
	R	Universal gas constant
	$\frac{\Delta V}{V}$	Volumetric expansion
	$\overset{\cdot}{\sigma}$	Equivalent von Mises flow stress
	YS	Yield strength
	$\sigma_{\!y}$	Yield strength
	Α	Yield Strength JC parameter
	C_1	YS MZA parameter
	ZA	Zerilli-Armstrong
1682		
1683		
1684		
1685		
1686		
1687		
1688		
1689		
1690		
1691		
1692		
1693		
1694		
1695		
1696		

1697	FERENCES	
1698 1699 1700 1701	1.	Furrer, D. and Fecht, H., 1999, "Ni-based superalloys for turbine discs," The Journal of The Minerals, Metals & Materials Society, 51 (1), pp. 14-17. DOI: 10.1007/s11837-999-0005-y
1702 1703 1704 1705	2.	Kuo, CM., Yang, YT., Bor, HY., Wei, CN., and Tai, CC., 2009, "Aging effects on the microstructure and creep behavior of Inconel 718 superalloy," Materials Science and Engineering: A, 510-511 , pp. 289-294. DOI: 10.1016/j.msea.2008.04.097
1706	3.	Nowotnik, A., 2016, "Nickel-based superalloys." DOI:
1707 1708 1709 1710	4.	Mignanelli, P. M., Jones, N. G., Pickering, E. J., Messé, O. M. D. M., Rae, C. M. F., Hardy, M. C., and Stone, H. J., 2017, "Gamma-gamma prime-gamma double prime dual-superlattice superalloys," Scripta Materialia, 136 , pp. 136-140. DOI: 10.1016/j.scriptamat.2017.04.029
1711 1712 1713	5.	Czyrska-Filemonowicz, A., Dubiel, B., Zietara, M., and Cetel, A., 2007, "Development of single crystal Ni-based superalloys for advanced aircraft turbine blades," Inżynieria Materiałowa, 28 (3-4), pp. 128-133. DOI:
1714 1715 1716 1717	6.	Wang, J., Guo, WG., Su, Y., Zhou, P., and Yuan, K., 2016, "Anomalous behaviors of a single-crystal Nickel-base superalloy over a wide range of temperatures and strain rates," Mechanics of Materials, 94 , pp. 79-90. DOI: 10.1016/j.mechmat.2015.11.015
1718 1719 1720 1721	7.	Lin, Ph., Tobushi, H., Tanaka, K., Hattori, T., and Ikai, A., 1996, "Influence of Strain Rate on Deformation Properties of TiNi Shape Memory Alloy," JSME International Journal. Ser. A, Mechanics and Material Engineering, 39 (1), pp. 117-123. DOI: 10.1299/jsmea1993.39.1 117
1722 1723 1724	8.	Knipling, K. E., Dunand, D. C., and Seidman, D. N., 2006, "Criteria for developing castable, creep-resistant aluminum-based alloys – A review," International Journal of Materials Research, 97 (3), pp. 246-265. DOI: <u>10.3139/ijmr-2006-0042</u>
1725 1726	9.	Shang, S. L., Zacherl, C. L., Fang, H. Z., Wang, Y., Du, Y., and Liu, Z. K., 2012, "Effects of alloying element and temperature on the stacking fault energies of dilute Ni-

1727 1728		base superalloys," Journal of Physics: Condensed Matter, 24 (50), pp. 505403. DOI: <u>10.1088/0953-8984/24/50/505403</u>
1729 1730	10.	Sims, C. T., Stoloff, N. S., and Hagel, W. C., Superalloys II, 1987, 8, John Wiley & Sons, Inc. ISBN: 0-471-01146-9
1731 1732 1733	11.	Thakur, A. and Gangopadhyay, S., 2016, "State-of-the-art in surface integrity in machining of nickel-based super alloys," International Journal of Machine Tools and Manufacture, 100 , pp. 25-54. DOI: <u>10.1016/j.ijmachtools.2015.10.001</u>
1734 1735 1736	12.	Ranganath, S., Guo, C., and Hegde, P., 2009, "A finite element modeling approach to predicting white layer formation in nickel superalloys," CIRP Annals - Manufacturing Technology, 58 (1), pp. 77-80. DOI: <u>10.1016/j.cirp.2009.03.109</u>
1737 1738 1739 1740	13.	Ulutan, D. and Özel, T., 2013, "Multiobjective Optimization of Experimental and Simulated Residual Stresses in Turning of Nickel-Alloy IN100," Materials and Manufacturing Processes, 28 (7), pp. 835-841. DOI: 10.1080/10426914.2012.718474
1741 1742 1743 1744	14.	Sharman, A. R. C., Hughes, J. I., and Ridgway, K., 2004, "Workpiece Surface Integrity and Tool Life Issues When Turning Inconel 718™ Nickel Based Superalloy," Machining Science and Technology, 8 (3), pp. 399-414. DOI: 10.1081/MST-200039865
1745 1746 1747	15.	Ezugwu, E., Wang, Z., and Okeke, C., 1999, "Tool life and surface integrity when machining Inconel 718 with PVD-and CVD-coated tools," Tribology transactions, 42 (2), pp. 353-360. DOI:
1748 1749 1750 1751	16.	Axinte, D. A. and Chiffre, L. D., 2008, "Effectiveness and resolution of tests for evaluating the performance of cutting fluids in machining aerospace alloys," CIRP Annals - Manufacturing Technology, 57 (1), pp. 129-132. DOI: 10.1016/j.cirp.2008.03.081
1752 1753 1754 1755	17.	Ulutan, D., Arisoy, Y. M., Özel, T., and Mears, L., 2014, "Empirical modeling of residual stress profile in machining nickel-based superalloys using the sinusoidal decay function," Procedia CIRP, 13 , pp. 365-370. DOI: 10.1016/j.procir.2014.04.062

1756 1757 1758 1759	18.	Fan, Y., Hao, Z., Zheng, M., Sun, F., and Yang, S., 2013, "Study of surface quality in machining nickel-based alloy Inconel 718," The International Journal of Advanced Manufacturing Technology, 69 (9), pp. 2659-2667. DOI: 10.1007/s00170-013-5225-1
1760 1761 1762	19.	Umbrello, D., 2013, "Investigation of surface integrity in dry machining of Inconel 718," The International Journal of Advanced Manufacturing Technology, 69 (9), pp. 2183-2190. DOI: 10.1007/s00170-013-5198-0
1763 1764 1765 1766	20.	Pawade, R., Joshi, S. S., and Brahmankar, P., 2008, "Effect of machining parameters and cutting edge geometry on surface integrity of high-speed turned Inconel 718," International Journal of Machine Tools and Manufacture, 48 (1), pp. 15-28. DOI:
1767 1768 1769 1770	21.	Shokrani, A., Dhokia, V., Newman, S. T., and Imani-Asrai, R., 2012, "An Initial Study of the Effect of Using Liquid Nitrogen Coolant on the Surface Roughness of Incone 718 Nickel-Based Alloy in CNC Milling," Procedia CIRP, 3 , pp. 121-125. DOI: 10.1016/j.procir.2012.07.022
1771 1772 1773	22.	Aramcharoen, A. and Chuan, S. K., 2014, "An experimental investigation on cryogenic milling of Inconel 718 and its sustainability assessment," Procedia CIRP, 14 , pp. 529-534. DOI: <u>10.1016/j.procir.2014.03.076</u>
1774 1775 1776	23.	Yildiz, Y. and Nalbant, M., 2008, "A review of cryogenic cooling in machining processes," International Journal of Machine Tools and Manufacture, 48 (9), pp. 947-964. DOI:
1777 1778 1779 1780 1781	24.	Aspinwall, D. K., Dewes, R. C., Ng, EG., Sage, C., and Soo, S. L., 2007, "The influence of cutter orientation and workpiece angle on machinability when high-speed milling Inconel 718 under finishing conditions," International Journal of Machine Tools and Manufacture, 47 (12-13), pp. 1839-1846. DOI: 10.1016/j.ijmachtools.2007.04.007
1782 1783 1784 1785	25.	Rahim, E. A. and Sasahara, H., 2011, "AN ANALYSIS OF SURFACE INTEGRITY WHEN DRILLING INCONEL 718 USING PALM OIL AND SYNTHETIC ESTER UNDER MQL CONDITION," Machining Science and Technology, 15 (1), pp. 76-90. DOI: 10.1080/10910344.2011.557967

1786 1787 1788 1789	26.	Farid, A. A., Sharif, S., and Namazi, H., 2009, "Effect of Machining Parameters and Cutting Edge Geometry on Surface Integrity when Drilling and Hole Making in Inconel 718," SAE International Journal of Materials and Manufacturing, 2 (1), pp. 564-569. DOI:
1790 1791 1792 1793	27.	M'Saoubi, R., Axinte, D., Herbert, C., Hardy, M., and Salmon, P., 2014, "Surface integrity of nickel-based alloys subjected to severe plastic deformation by abusive drilling," CIRP Annals - Manufacturing Technology, 63 (1), pp. 61-64. DOI: 10.1016/j.cirp.2014.03.067
1794 1795 1796 1797 1798	28.	Madariaga, A., Esnaola, J. A., Fernandez, E., Arrazola, P. J., Garay, A., and Morel, F., 2014, "Analysis of residual stress and work-hardened profiles on Inconel 718 when face turning with large-nose radius tools," The International Journal of Advanced Manufacturing Technology, 71 (9), pp. 1587-1598. DOI: 10.1007/s00170-013-5585-6
1799 1800 1801	29.	Kortabarri, A., Madariag, A., Fernandez, E., Esnaol, J. A., and Arrazola, P. J., 2011, "A comparative study of residual stress profiles on Inconel 718 induced by dry face turning," Procedia CIRP, 19 , pp. 228-234. DOI: <u>10.1016/j.proeng.2011.11.105</u>
1802 1803 1804	30.	Chen, Z., Surface Integrity of Broached Inconel 718 and Influence of Thermal Exposure, in Department of Management and Engineering. 2014, Linköping University: Digitala Vetenskapliga Arkivet. pp. 44.
1805 1806 1807	31.	Klocke, F., Vogtel, P., Gierlings, S., Lung, D., and Veselovac, D., 2013, "Broaching of Inconel 718 with cemented carbide," Production Engineering, 7 (6), pp. 593-600. DOI: 10.1007/s11740-013-0483-1
1808 1809 1810	32.	Lee, SM., Chow, HM., and Yan, BH., 2007, "Friction Drilling of IN-713LC Cast Superalloy," Materials and Manufacturing Processes, 22 (7-8), pp. 893-897. DOI: 10.1080/10426910701451697
1811 1812 1813	33.	Thakur, A., Gangopadhyay, S., and Maity, K. P., 2014, "Effect of cutting speed and CVD multilayer coating on machinability of Inconel 825," Surface Engineering, 30 (7), pp. 516-523. DOI: 10.1179/1743294414Y.0000000274
1814 1815	34.	Joshi, S. V., Vizhian, S. P., Sridhar, B. R., and Jayaram, K., 2008, "Parametric Study of Machining Effect on Residual Stress and Surface Roughness of Nickel Base Super

1816 1817		Alloy UDIMET 720," Advanced Materials Research, 47-50 , pp. 13-16. DOI: 10.4028/www.scientific.net/AMR.47-50.13
1818 1819 1820 1821	35.	Jin, D., Liu, Z., Yi, W., and Su, G., 2011, "Influence of cutting speed on surface integrity for powder metallurgy nickel-based superalloy FGH95," The International Journal of Advanced Manufacturing Technology, 56 (5-8), pp. 553-559. DOI: 10.1007/s00170-011-3196-7
1822 1823 1824 1825	36.	Veldhuis, S. C., Dosbaeva, G. K., Elfizy, A., Fox-Rabinovich, G. S., and Wagg, T., 2010, "Investigations of White Layer Formation During Machining of Powder Metallurgical Ni-Based ME 16 Superalloy," Journal of Materials Engineering and Performance, 19 (7), pp. 1031-1036. DOI: <u>10.1007/s11665-009-9567-7</u>
1826 1827 1828	37.	Axinte, D. A., Andrews, P., Li, W., Gindy, N., Withers, P. J., and Childs, T. H. C., 2006, "Turning of advanced Ni based alloys obtained via powder metallurgy route," CIRP Annals, 55 (1), pp. 117-120. DOI: <u>10.1016/S0007-8506(07)60379-5</u>
1829 1830 1831 1832	38.	Marinescu, I. and Axinte, D. A., 2011, "An automated monitoring solution for avoiding an increased number of surface anomalies during milling of aerospace alloys," International Journal of Machine Tools and Manufacture, 51 (4), pp. 349-357. DOI: 10.1016/j.ijmachtools.2010.10.005
1833 1834 1835 1836	39.	Soo, S. L., Hood, R., Aspinwall, D. K., Voice, W. E., and Sage, C., 2011, "Machinability and surface integrity of RR1000 nickel based superalloy," CIRP Annals - Manufacturing Technology, 60 (1), pp. 89-92. DOI: 10.1016/j.cirp.2011.03.094
1837 1838 1839 1840	40.	Herbert, C. R. J., Axinte, D. A., Hardy, M. C., and Brown, P. D., 2011, "Investigation into the Characteristics of White Layers Produced in a Nickel-Based Superalloy from Drilling Operations," Procedia Engineering, 19 , pp. 138-143. DOI: 10.1016/j.proeng.2011.11.092
1841 1842 1843 1844	41.	Shi, D., Axinte, D. A., and Gindy, N. N., 2007, "Development of an online machining process monitoring system: a case study of the broaching process," The International Journal of Advanced Manufacturing Technology, 34 (1-2), pp. 34-46. DOI: <u>10.1007/s00170-006-0588-1</u>
1845 1846	42.	Axinte, D. A. and Andrews, P., 2007, "Some considerations on tool wear and workpiece surface quality of holes finished by reaming or milling in a nickel base

1847 1848	superalloy," Proceedings of the Institution of Mechanical Engineers, Part B: Journal of Engineering Manufacture, 221 (4), pp. 591-603. DOI: <u>10.1243/09544054JEM704</u>
1849 43. 1850 1851	Zou, B., Chen, M., Huang, C., and An, Q., 2009, "Study on surface damages caused by turning NiCr20TiAl nickel-based alloy," Journal of Materials Processing Technology, 209 (17), pp. 5802-5809. DOI: <u>10.1016/j.jmatprotec.2009.06.017</u>
1852 44. 1853 1854	Wright, P. K. and Chow, J. G., 1982, "Deformation Characteristics of Nickel Alloys During Machining," Journal of Engineering Materials and Technology, 104 (2), pp. 85-93. DOI: <u>10.1115/1.3225057</u>
1855 45. 1856 1857	Podder, B. and Paul, S., 2012, "Improvement of machinability in end milling of Nimonic C-263 by application of high pressure coolant," International Journal of Machining and Machinability of Materials, 11 (4), pp. 418-433. DOI:
1858 46. 1859 1860	Ezilarasan, C. and Kumar, V. S. S., 2012, "The Effect of the Machining Parameters on the Micro Hardness and Residual Stresses in the Turning of Nimonic C-263 Alloy," International Review of Mechanical Engineering, 6 (3). DOI:
1861 47. 1862 1863 1864 1865	Razak, N. H., Rahman, M. M., and Kadirgama, K., 2012," Response Surface Design Model to Predict Surface Roughness when Machining Hastelloy C2000 using Uncoated Carbide Insert," <i>Proc.</i> 1st International Conference on Mechanical Engineering Research (ICMER2011), Bakar, R. A., eds., Kuantan, Pahang, Malaysia, 36, pp. 012022.
1866 48. 1867 1868	Hood, R., Soo, S. L., Aspinwall, D. K., Andrews, P., and Sage, C., 2011, "Twist Drilling of Haynes 282 Superalloy," Procedia CIRP, 19 , pp. 150-155. DOI: 10.1016/j.proeng.2011.11.094
1869 49 . 1870 1871 1872	Hood, R., Soo, S. L., Aspinwall, D. K., Andrews, P., and Sage, C., 2012, "Radius end milling of Haynes 282 nickel based superalloy," Proceedings of the Institution of Mechanical Engineers, Part B: Journal of Engineering Manufacture, 226 (10), pp. 1745-1753. DOI: 10.1177/0954405412455886
1873 50. 1874 1875	Hoier, P., Malakizadi, A., Stuppa, P., Cedergren, S., and Klement, U., 2018, "Microstructural characteristics of Alloy 718 and Waspaloy and their influence on flank wear during turning," Wear, 400 , pp. 184-193. DOI:

1876 1877 1878	51.	Polvorosa, R., Suárez, A., de Lacalle, L. L., Cerrillo, I., Wretland, A., and Veiga, F., 2017, "Tool wear on nickel alloys with different coolant pressures: Comparison of Alloy 718 and Waspaloy," Journal of Manufacturing Processes, 26 , pp. 44-56. DOI:
1879 1880	52.	Kennedy, R., 2005, "Allvac 718Plus, superalloy for the next forty years," Superalloys, 718 (706), pp. 1-14. DOI:
1881 1882	53.	Klocke, F., Seimann, M., Binder, M., and Doebbeler, B., 2018, "Milling of fir-tree slots in Allvac 718 plus," Procedia CIRP, 77 , pp. 409-412. DOI:
1883 1884	54.	Davis, J. R., <i>ASM Specialty Handbook: Heat-Resistant Materials</i> , 1997, Sanders, B. R., ASM International. ISBN: 0871705966
1885 1886 1887	55.	Ezugwu, E. O., Wang, Z. M., and Machado, A. R., 1999, "The machinability of nickel-based alloys: a review," Journal of Materials Processing Technology, 86 (1-3), pp. 1-16. DOI: 10.1016/S0924-0136(98)00314-8
1888 1889	56.	Davis, J. R., <i>ASM Specialty Handbook: Nickel, Cobalt, and Their Alloys</i> , 2000, Hrivnak, N., ASM International. ISBN: 0871706857
1890 1891 1892	57.	Goodfellow, A. J., 2018, "Strengthening mechanisms in polycrystalline nickel-based superalloys," Materials Science and Technology, 34 (15), pp. 1793-1808. DOI: 10.1080/02670836.2018.1461594
1893 1894 1895	58.	van Foreest, A., Sippel, M., Gülhan, A., Esser, B., Ambrosius, B. A. C., and Sudmeijer, K., 2009, "Transpiration Cooling Using Liquid Water," Journal of Thermophysics and Heat Transfer, 23 (4), pp. 693-702. DOI: <u>10.2514/1.39070</u>
1896 1897	59.	Davies, R. G. and Stoloff, N. S., 1965, "On yield stress of aged Ni-Al alloys," Transactions of the Metallurgical Society of AIME, 233 (4), pp. 714. DOI:
1898 1899	60.	Reed, R. C., <i>The Superalloys: Fundamentals and Applications</i> , 2008, Cambridge University Press. ISBN: 1139458639
1900 1901 1902	61.	Piearcey, B. J., Kear, B. H., and Smashey, R. W., 1967, "Correlation of structure with properties in a directionally solidified nickel-base superalloy," ASM Trans Quart, 60 (4), pp. 634-645. DOI:

1903 1904 1905	62.	Eickemeyer, S. C., Steinkamp, S., Schuster, B., Bodenhage, F., and Nyhuis, P., 2014, "Reliable Capacity Planning Despite Uncertain Disassembly, Regeneration and Reassembly Workloads by Using Statistical and Mathematical Approaches –
1905		Validation in Subsidiaries of a Global MRO Company with Operations in Asia,
1900		Europe and North America," Procedia CIRP, 23 , pp. 252-257. DOI:
1908		10.1016/j.procir.2014.10.097
1700		10.1016/j.p. com.201 1.10.05/
1909	63.	Breeze, P., 2016, Gas-Turbine Power Generation, Breeze, P., Academic Press,
1910		Chapter 4: Gas Turbines. ISBN: 978-0-12-804005-8
1911	64.	Zhao, J. C. and Westbrook, J. H., 2003, "Ultrahigh-Temperature Materials for Jet
1912		Engines," MRS Bulletin, 28 (9), pp. 622-630. DOI: <u>10.1557/mrs2003.189</u>
1913	65.	Soyama, H. and Okura, Y., 2018, "The use of various peening methods to improve
1914		the fatigue strength of titanium alloy Ti6Al4V manufactured by electron beam
1915		melting," AIMS Mater. Sci, 5 (5), pp. 1000-1015. DOI:
1916	66.	Ezugwu, E. O., 2005, "Key improvements in the machining of difficult-to-cut
1917		aerospace superalloys," International Journal of Machine Tools and Manufacture,
1918		45 (12-13), pp. 1353-1367. DOI: <u>10.1016/j.ijmachtools.2005.02.003</u>
1919	67.	Kahles, J. F. and Field, M., 1967, "Paper 4: Surface Integrity—A New Requirement
1920		for Surfaces Generated by Material-Removal Methods," Proceedings of the
1921		Institution of Mechanical Engineers, Conference Proceedings, 182 (11), pp. 31-45.
1922		DOI: 10.1243/pime conf 1967 182 301 02
1022	CO	Yıldırım, Ç. V., Kıvak, T., Sarıkaya, M., and Şirin, Ş., 2020, "Evaluation of tool wear,
1923 1924	68.	surface roughness/topography and chip morphology when machining of Ni-based
1924		alloy 625 under MQL, cryogenic cooling and CryoMQL," Journal of Materials
1926		Research and Technology, 9 (2), pp. 2079-2092. DOI: <u>10.1016/j.jmrt.2019.12.069</u>
1720		10.1010/j.jimt.2015.12.005
1927	69.	Devillez, A., Coz, G. L., Dominiak, S., and Dudzinski, D., 2011, "Dry machining of
1928		Inconel 718, workpiece surface integrity," Journal of Materials Processing
1929		Technology, 211 (10), pp. 1590-1598. DOI: <u>10.1016/j.jmatprotec.2011.04.011</u>
1026		
1930	70.	Wang, B. and Liu, Z., 2018, "Influences of tool structure, tool material and tool
1931		wear on machined surface integrity during turning and milling of titanium and
1932		nickel alloys: a review," The International Journal of Advanced Manufacturing
1933		Technology, 98 (5), pp. 1925-1975. DOI: <u>10.1007/s00170-018-2314-1</u>

1934 1935 1936 1937	71.	Liao, Z., Polyakov, M., Diaz, O. G., Axinte, D., Mohanty, G., Maeder, X., Michler, J., and Hardy, M., 2019, "Grain refinement mechanism of nickel-based superalloy by severe plastic deformation - Mechanical machining case," Acta Materialia, 180 , pp 2-14. DOI: 10.1016/j.actamat.2019.08.059
1938 1939 1940 1941	72.	Pervaiz, S., Rashid, A., Deiab, I., and Nicolescu, M., 2014, "Influence of Tool Materials on Machinability of Titanium- and Nickel-Based Alloys: A Review," Materials and Manufacturing Processes, 29 (3), pp. 219-252. DOI: 10.1080/10426914.2014.880460
1942 1943 1944 1945	73.	Shao, S., Khonsari, M. M., Guo, S., Meng, W. J., and Li, N., 2019, "Overview: Additive Manufacturing Enabled Accelerated Design of Ni-based Alloys for Improved Fatigue Life," Additive Manufacturing, 29 , pp. 100779. DOI: 10.1016/j.addma.2019.100779
1946 1947 1948	74.	Suárez, A., Veiga, F., Lacalle, L. N. L. d., Polvorosa, R., and Wretland, A., 2019, "An investigation of cutting forces and tool wear in turning of Haynes 282," Journal of Manufacturing Processes, 37 , pp. 529-540. DOI: <u>10.1016/j.jmapro.2018.12.025</u>
1949 1950 1951 1952	75.	Wstawska, I. and Ślimak, K., 2016, "The influence of cooling techniques on cutting forces and surface roughness during cryogenic machining of titanium alloys," Archives of Mechanical Technology and Materials, 36 . DOI: 10.1515/amtm-2016-0003
1953 1954 1955	76.	Altin, A., Nalbant, M., and Taskesen, A., 2007, "The effects of cutting speed on too wear and tool life when machining Inconel 718 with ceramic tools," Materials & Design, 28 (9), pp. 2518-2522. DOI: <u>10.1016/j.matdes.2006.09.004</u>
1956 1957 1958 1959	77.	Pusavec, F., Hamdi, H., Kopac, J., and Jawahir, I. S., 2011, "Surface integrity in cryogenic machining of nickel based alloy—Inconel 718," Journal of Materials Processing Technology, 211 (4), pp. 773-783. DOI: 10.1016/j.jmatprotec.2010.12.013
1960 1961 1962	78.	Johnson, G. R., 1983," A constitutive model and data for materials subjected to large strains, high strain rates, and high temperatures," <i>Proc.</i> Proc. 7th Inf. Sympo Ballistics, eds., pp. 541-547.
1963 1964	79.	Melkote, S. N., Grzesik, W., Outeiro, J., Rech, J., Schulze, V., Attia, H., Arrazola, P J., M'Saoubi, R., and Saldana, C., 2017. "Advances in material and friction data for

1965 1966		modelling of metal machining," CIRP Annals - Manufacturing Technology, 66 (2), pp. 731-754. DOI: 10.1016/j.cirp.2017.05.002
1967 1968 1969	80.	Man, X., Ren, D., Usui, S., Johnson, C., and Marusich, T. D., 2012, "Validation of Finite Element Cutting Force Prediction for End Milling," Procedia CIRP, 1 , pp. 663-668. DOI: 10.1016/j.procir.2012.05.019
1970 1971 1972 1973 1974	81.	Sadeghifar, M., Sedaghati, R., Jomaa, W., and Songmene, V., 2018, "A comprehensive review of finite element modeling of orthogonal machining process: chip formation and surface integrity predictions," The International Journal of Advanced Manufacturing Technology, 96 (9-12), pp. 3747-3791. DOI: 10.1007/s00170-018-1759-6
1975 1976 1977 1978	82.	Bollig, P., Faltin, C., Schießl, R., Schneider, J., Maas, U., and Schulze, V., 2015, "Considering the Influence of Minimum Quantity Lubrication for Modelling Changes in Temperature, Forces and Phase Transformations during Machining," Procedia CIRP, 31 , pp. 142-147. DOI: 10.1016/j.procir.2015.03.025
1979 1980	83.	Astakhov, V. P., <i>TRIBOLOGY OF METAL CUTTING</i> , 2006, Briscoe, B. J., Elsevier Ltd. ISBN: 0080466850
1981 1982 1983 1984	84.	Melkote, S. N., Liu, R., Fernandez-Zelaia, P., and Marusich, T., 2015, "A physically based constitutive model for simulation of segmented chip formation in orthogonal cutting of commercially pure titanium," CIRP Annals - Manufacturing Technology, 64 (1), pp. 65-68. DOI: <u>10.1016/j.cirp.2015.04.060</u>
1985 1986 1987 1988	85.	Liu, H., Xu, X., Zhang, J., Liu, Z., He, Y., Zhao, W., and Liu, Z., 2022, "The state of the art on numerical simulation of the effect of microstructure and its evolution in metal-cutting processes," International Journal of Machine Tools and Manufacture, 177 , pp. 103890. DOI: <u>10.1016/j.ijmachtools.2022.103890</u>
1989 1990 1991 1992 1993	86.	Roters, F., Eisenlohr, P., Hantcherli, L., Tjahjanto, D. D., Bieler, T. R., and Raabe, D., 2010, "Overview of constitutive laws, kinematics, homogenization and multiscale methods in crystal plasticity finite-element modeling: Theory, experiments, applications," Acta Materialia, 58 (4), pp. 1152-1211. DOI: 10.1016/j.actamat.2009.10.058
1994 1995	87.	Kwong, J., Axinte, D. A., and Withers, P. J., 2009, "The sensitivity of Ni-based superalloy to hole making operations: Influence of process parameters on

1996 1997		subsurface damage and residual stress," Journal of Materials Processing Technology, 209 (8), pp. 3968-3977. DOI: <u>10.1016/j.jmatprotec.2008.09.014</u>
1998 1999 2000 2001	88.	Zhang, D., Zhang, XM., Nie, GC., Yang, ZY., and Ding, H., 2021, "Characterization of material strain and thermal softening effects in the cutting process," International Journal of Machine Tools and Manufacture, 160 , pp. 103672. DOI: 10.1016/j.ijmachtools.2020.103672
2002 2003 2004 2005	89.	Zhao, Y., Sun, J., Li, J., Yan, Y., and Wang, P., 2017, "A comparative study on Johnson-Cook and modified Johnson-Cook constitutive material model to predict the dynamic behavior laser additive manufacturing FeCr alloy," Journal of Alloys and Compounds, 723 , pp. 179-187. DOI: 10.1016/j.jallcom.2017.06.251
2006 2007 2008	90.	Schoop, J., Hasan, M. M., and Zannoun, H., 2022, "Physics-Informed and Data- Driven Prediction of Residual Stress in Three-Dimensional Machining," Experimental Mechanics, 62 (8), pp. 1461-1474. DOI: <u>10.1007/s11340-022-00880-4</u>
2009 2010 2011 2012	91.	Iturbe, A., Giraud, E., Hormaetxe, E., Garay, A., Germain, G., Ostolaza, K., and Arrazola, P. J., 2017, "Mechanical characterization and modelling of Inconel 718 material behavior for machining process assessment," Materials Science and Engineering: A, 682 , pp. 441-453. DOI: <u>10.1016/j.msea.2016.11.054</u>
2013 2014 2015 2016	92.	Zhang, XM., Zhang, K., Zhang, D., Outeiro, J., and Ding, H., 2019, "New In Situ Imaging-Based Methodology to Identify the Material Constitutive Model Coefficients in Metal Cutting Process," Journal of Manufacturing Science and Engineering, 141 (10). DOI: <u>10.1115/1.4044251</u>
2017 2018	93.	Abouridouane, M., Klocke, F., Lung, D., and Veselovac, D., 2015, "The mechanics of cutting: in-situ measurement and modelling," Procedia CIRP, 31 , pp. 246-251. DOI:
2019 2020	94.	Davis, J. R., <i>ASM Specialty Handbook: Tool Materials</i> , 1995, Reidenbach, F., ASM international. ISBN: 0871705451
2021 2022 2023 2024	95.	DeMange, J. J., Prakash, V., and Pereira, J. M., 2009, "Effects of material microstructure on blunt projectile penetration of a nickel-based super alloy," International Journal of Impact Engineering, 36 (8), pp. 1027-1043. DOI: 10.1016/j.ijimpeng.2009.01.007

2025 2026 2027 2028	96.	Özel, T., Llanos, I., Soriano, J., and Arrazola, PJ., 2011, "3D FINITE ELEMENT MODELLING OF CHIP FORMATION PROCESS FOR MACHINING INCONEL 718: COMPARISON OF FE SOFTWARE PREDICTIONS," Machining Science and Technology, 15 (1), pp. 21-46. DOI: <u>10.1080/10910344.2011.557950</u>
2029 2030 2031 2032 2033	97.	Tian, P., He, L., Zhou, T., Du, F., Zou, Z., Zhou, X., and Jiang, H., 2022, "Reverse identification of constitutive parameters of Inconel 718 alloy based on analytical model and thermo-mechanical loads analysis of machined surface," Journal of Materials Research and Technology, 16 , pp. 1353-1370. DOI: 10.1016/j.jmrt.2021.11.164
2034 2035 2036 2037	98.	Mitrofanov, A. V., Babitsky, V. I., and Silberschmidt, V. V., 2004, "Finite element analysis of ultrasonically assisted turning of Inconel 718," Journal of Materials Processing Technology, 153-154 , pp. 233-239. DOI: 10.1016/j.jmatprotec.2004.04.299
2038 2039 2040	99.	Hao, Z., Li, J., Fan, Y., and Ji, F., 2019, "Study on constitutive model and deformation mechanism in high speed cutting Inconel718," Archives of Civil and Mechanical Engineering, 19 (2), pp. 439-452. DOI: <u>10.1016/j.acme.2018.11.009</u>
2041 2042 2043 2044	100.	Blumm, J., Lindemann, A., and Niedrig, B., 2003," Measurement of the Thermophysical Properties of an NPL Thermal Conductivity Standard Inconel 600," <i>Proc.</i> 17th European Conference on Thermophysical Properties, eds., Bratislava, Slovak Republicpp. 621-626.
2045 2046 2047	101.	Zhang, X., Chen, Z., and Liu, Y., 2017, <i>The Material Point Method: A Continuum-Based Particle Method for Extreme Loading Cases</i> , Elsevier, Inc., Oxford, UK, Chapter 6 - Constitutive Models. ISBN: 978-0-12-407716-4
2048 2049 2050 2051	102.	Guo, Y. B., Wen, Q., and Woodbury, K. A., 2005, "Dynamic Material Behavior Modeling Using Internal State Variable Plasticity and Its Application in Hard Machining Simulations," Journal of Manufacturing Science and Engineering, 128 (3), pp. 749-759. DOI: <u>10.1115/1.2193549</u>
2052 2053 2054 2055	103.	Calamaz, M., Coupard, D., and Girot, F., 2008, "A new material model for 2D numerical simulation of serrated chip formation when machining titanium alloy Ti–6Al–4V," International Journal of Machine Tools and Manufacture, 48 (3-4), pp. 275-288. DOI: <u>10.1016/j.ijmachtools.2007.10.014</u>

2056 2057 2058 2059	104.	Rotella, G. and Umbrello, D., 2014, "Finite element modeling of microstructural changes in dry and cryogenic cutting of Ti6Al4V alloy," CIRP Annals - Manufacturing Technology, 63 (1), pp. 69-72. DOI: http://dx.doi.org/10.1016/j.cirp.2014.03.074
2060 2061 2062 2063	105.	Denguir, L. A., Outeiro, J. C., Fromentin, G., Vignal, V., and Besnard, R., 2017, "A physical-based constitutive model for surface integrity prediction in machining of OFHC copper," Journal of Materials Processing Technology, 248 , pp. 143-160. DOI: 10.1016/j.jmatprotec.2017.05.009
2064 2065 2066 2067	106.	Cheng, W., Outeiro, J., Costes, JP., M'Saoubi, R., Karaouni, H., and Astakhov, V., 2019, "A constitutive model for Ti6Al4V considering the state of stress and strain rate effects," Mechanics of Materials, 137 , pp. 103103. DOI: 10.1016/j.mechmat.2019.103103
2068 2069 2070	107.	Bai, Y. and Wierzbicki, T., 2008, "A new model of metal plasticity and fracture with pressure and Lode dependence," International Journal of Plasticity, 24 (6), pp. 1071-1096. DOI: 10.1016/j.ijplas.2007.09.004
2071 2072 2073 2074	108.	Jaspers, S. P. F. C. and Dautzenberg, J. H., 2002, "Material behaviour in conditions similar to metal cutting: flow stress in the primary shear zone," Journal of Materials Processing Technology, 122 (2), pp. 322-330. DOI: <u>10.1016/S0924-0136(01)01228-6</u>
2075 2076 2077	109.	Childs, T. H. C. and Rahmad, R., 2009, "Modelling orthogonal machining of carbon steels. Part II: Comparisons with experiments," International Journal of Mechanica Sciences, 51 (6), pp. 465-472. DOI: 10.1016/j.ijmecsci.2009.04.001
2078 2079 2080	110.	Lin, Y. C. and Chen, XM., 2010, "A combined Johnson–Cook and Zerilli–Armstrong model for hot compressed typical high-strength alloy steel," Computational Materials Science, 49 (3), pp. 628-633. DOI: <u>10.1016/j.commatsci.2010.06.004</u>
2081 2082 2083	111.	Zerilli, F. J., 2004, "Dislocation mechanics-based constitutive equations," Metallurgical and Materials Transactions A, 35 (9), pp. 2547-2555. DOI: 10.1007/s11661-004-0201-x
2084 2085 2086	112.	Bobbili, R., Ramakrishna, B., and Madhu, V., 2017, "Dynamic compressive behavior and fracture modeling of Titanium alloy IMI 834," Journal of Alloys and Compounds, 714 , pp. 225-231. DOI: 10.1016/j.jallcom.2017.04.228

2087 11 2088 2089 2090	 Kotkunde, N., Deole, A. D., Gupta, A. K., and Singh, S. K., 2014, "Comparative study of constitutive modeling for Ti–6Al–4V alloy at low strain rates and elevated temperatures," Materials & Design, 55, pp. 999-1005. DOI: 10.1016/j.matdes.2013.10.089
2091 11 2092 2093 2094	 Kotkunde, N., Srinivasan, S., Krishna, G., Gupta, A. K., and Singh, S. K., 2016, "Influence of material models on theoretical forming limit diagram prediction for Ti–6Al–4V alloy under warm condition," Transactions of Nonferrous Metals Society of China, 26(3), pp. 736-746. DOI: 10.1016/S1003-6326(16)64140-7
2095 11 2096	5. Oxley, P. L. B., 1963, "Mechanics of Metal Cutting for a Material of Variable Flow Stress," Journal of Engineering for Industry. DOI: <u>10.1115/1.3669887</u>
2097 11 2098 2099	6. Stevenson, M. and Oxley, P., 1969, "An experimental investigation of the influence of speed and scale on the strain-rate in a zone of intense plastic deformation," Proceedings of the Institution of Mechanical Engineers, 184 (1), pp. 561-576. DOI:
2100 11 2101 2102 2103	7. Shi, B. and Attia, H., 2010, "CURRENT STATUS AND FUTURE DIRECTION IN THE NUMERICAL MODELING AND SIMULATION OF MACHINING PROCESSES: A CRITICAL LITERATURE REVIEW," Machining Science and Technology, 14 (2), pp. 149-188. DOI: 10.1080/10910344.2010.503455
2104 11 2105 2106 2107	8. Gurusamy, M. M. and Rao, B. C., 2017, "On the performance of modified Zerilli-Armstrong constitutive model in simulating the metal-cutting process," Journal of Manufacturing Processes, 28 (Part 1), pp. 253-265. DOI: 10.1016/j.jmapro.2017.06.011
2108 11 2109	9. Jaspers, S., Metal Cutting Mechanics and Material Behaviour. 1999, Technische Universiteit Eindhoven.
2110 12 2111 2112 2113	O. Adibi-Sedeh, A. H., Vaziri, M., Pednekar, V., Madhavan, V., and Ivester, R., 2005," Investigation of the Effect of Using Different Material Models on Finite Element Simulations of Machining," <i>Proc.</i> 8th CIRP International Workshop on Modeling of Machining Operations, Neugebauer, R., eds., Chemnitz, Germanypp. 215-224.
2114 12 2115	 Oxley, P. L. B. and Young, HT., 1990," The mechanics of machining: an analytical approach to assessing machinability," <i>Proc.</i> eds., pp.

2116 2117 2118 2119	122.	Maekawa, K., Shirakashi, T., and Usui, E., 1983, "Flow stress of low carbon steel at high temperature and strain rate. II: flow stress under variable temperature and variable strain rate," Bulletin of the Japan Society of Precision Engineering, 17(3), pp. 167-172. DOI:
2120 2121 2122 2123 2124	123.	Liu, C., Goel, S., Llavori, I., Stolf, P., Giusca, C. L., Zabala, A., Kohlscheen, J., Paiva, J. M., Endrino, J. L., and Veldhuis, S. C., 2019, "Benchmarking of several material constitutive models for tribology, wear, and other mechanical deformation simulations of Ti6Al4V," Journal of the Mechanical Behavior of Biomedical Materials, 97 , pp. 126-137. DOI: 10.1016/j.jmbbm.2019.05.013
2125 2126 2127	124.	Styger, G., Laubscher, R. F., and Oosthuizen, G. A., 2014, "Effect of Constitutive Modeling During Finite Element Analysis of Machining-induced Residual Stresses in Ti6Al4 V," Procedia CIRP, 13 , pp. 294-301. DOI: <u>10.1016/j.procir.2014.04.050</u>
2128 2129 2130	125.	Shi, B. and Attia, H., 2009, "MODELING THE THERMAL AND TRIBOLOGICAL PROCESSES AT THE TOOL-CHIP INTERFACE IN MACHINING," Machining Science and Technology, 13 (2), pp. 210-226. DOI: <u>10.1080/10910340903007605</u>
2131 2132 2133	126.	Shirakashi, T. and Usui, E., 1973, "Friction characteristics on tool face in metal machining," Bulletin of the Japan Society of Precision Engineering, 39 (9), pp. 966-972. DOI:
2134 2135 2136 2137	127.	Attia, M. H. and Kops, L., 2004, "A New Approach to Cutting Temperature Prediction Considering the Thermal Constriction Phenomenon in Multi-layer Coated Tools," CIRP Annals, 53 (1), pp. 47-52. DOI: <u>10.1016/S0007-8506(07)60642-8</u>
2138 2139 2140 2141	128.	Sartkulvanich, P., Altan, T., and Göcmen, A., 2005, "EFFECTS OF FLOW STRESS AND FRICTION MODELS IN FINITE ELEMENT SIMULATION OFORTHOGONAL CUTTING—A SENSITIVITY ANALYSIS," Machine Science and Technology, 9 (1), pp. 1-26. DOI: 10.1081/MST-200051211
2142 2143	129.	Schilke, P. W., Advanced Gas Turbine Materials and Coatings. 2004, G.E. Energy: Schenectady, NY.
2144 2145	130.	Warnecke, G., Fertigungstechnische Berichte: Spanbildung bei metallischen Werkstoffen, 1974, Resch.

2146 2147 2148	131.	Muthu, E., Senthamarai, K., and Jayabal, S., 2012, "Finite element simulation in machining of Inconel 718 nickel based super alloy," International Journal of Advanced Engineering Applications, 5 (3), pp. 22-27. DOI:
2149 2150	132.	International, A., Inconel 718 Material Data Sheet. 2021, Alloys International, Inc.: https://alloysintl.com/inventory/nickel-cobalt-alloys/inconel 718/.
2151 2152	133.	India, S. T., Inconel Alloy 600 price per kg. 2019, Steel Tubes India: https://www.stindia.com/inconel-alloy-600-625-718-price-per-kg-india.html .
2153 2154 2155 2156	134.	Jafarian, F., Umbrello, D., and Jabbaripour, B., 2016, "Identification of new material model for machining simulation of Inconel 718 alloy and the effect of tool edge geometry on microstructure changes," Simulation Modelling Practice and Theory, 66 , pp. 273-284. DOI: 10.1016/j.simpat.2016.05.001
2157 2158 2159 2160	135.	Barge, M., Hamdi, H., Rech, J., and Bergheau, JM., 2005, "Numerical modelling of orthogonal cutting: influence of numerical parameters," Journal of Materials Processing Technology, 164 , pp. 1148-1153. DOI: 10.1016/j.jmatprotec.2005.02.118
2161 2162 2163	136.	Carroll III, J. T. and Strenkowski, J. S., 1988, "Finite element models of orthogonal cutting with application to single point diamond turning," International Journal of Mechanical Sciences, 30 (12), pp. 899-920. DOI: <u>10.1016/0020-7403(88)90073-2</u>
2164 2165 2166 2167	137.	Xu, X., Outeiro, J., Zhang, J., Xu, B., Zhao, W., and Astakhov, V., 2021, "Machining simulation of Ti6Al4V using coupled Eulerian-Lagrangian approach and a constitutive model considering the state of stress," Simulation Modelling Practice and Theory, 110 , pp. 102312. DOI: <u>10.1016/j.simpat.2021.102312</u>
2168 2169 2170	138.	Marusich, T. D. and Ortiz, M., 1995, "Modelling and simulation of high-speed machining," International Journal for Numerical Methods in Engineering, 38 (21), pp. 3675-3694. DOI: 10.1002/nme.1620382108
2171 2172 2173	139.	da Silva, F. A. V. and Outeiro, J. C., 2021, "Machining simulation of Inconel 718 using Lagrangian and Coupled Eulerian-Lagrangian approaches," Procedia CIRP, 102 , pp. 453-458. DOI: <u>10.1016/j.procir.2021.09.077</u>

2174 2175 2176	140.	Bergs, T., Abouridouane, M., Meurer, M., and Peng, B., 2021, "Digital image correlation analysis and modelling of the strain rate in metal cutting," CIRP Annals 70 (1), pp. 45-48. DOI: 10.1016/j.cirp.2021.04.055
2177 2178 2179	141.	Ding, H. and Shin, Y. C., 2014, "Dislocation Density-Based Grain Refinement Modeling of Orthogonal Cutting of Titanium," Journal of Manufacturing Science and Engineering, 136 (4), pp. 041003. DOI: <u>10.1115/1.4027207</u>
2180 2181 2182 2183	142.	Silva, F. A. V. d., Denguir, L. A., and Outeiro, J. C., 2020, "Residual stresses prediction in machining of Inconel 718 superalloy using a constitutive model considering the state of stress," Procedia CIRP, 87 , pp. 527-532. DOI: 10.1016/j.procir.2020.02.029
2184 2185 2186 2187	143.	Algarni, M., Bai, Y., and Choi, Y., 2015, "A study of Inconel 718 dependency on stress triaxiality and Lode angle in plastic deformation and ductile fracture," Engineering Fracture Mechanics, 147 , pp. 140-157. DOI: 10.1016/j.engfracmech.2015.08.007
2188 2189 2190 2191	144.	Jafarian, F., Ciaran, M. I., Umbrello, D., Arrazola, P. J., Filice, L., and Amirabadi, H., 2014, "Finite element simulation of machining Inconel 718 alloy including microstructure changes," International Journal of Mechanical Sciences, 88 , pp. 110-121. DOI: 10.1016/j.ijmecsci.2014.08.007
2192 2193 2194 2195	145.	Wang, X., Huang, C., Zou, B., Liu, H., Zhu, H., and Wang, J., 2013, "Dynamic behavior and a modified Johnson–Cook constitutive model of Inconel 718 at high strain rate and elevated temperature," Materials Science and Engineering: A, 580 , pp. 385-390. DOI: <u>10.1016/j.msea.2013.05.062</u>
2196 2197 2198 2199	146.	Pereira, J. M. and Lerch, B. A., 2001, "Effects of heat treatment on the ballistic impact properties of Inconel 718 for jet engine fan containment applications," International Journal of Impact Engineering, 25 (8), pp. 715-733. DOI: 10.1016/S0734-743X(01)00018-5
2200 2201 2202	147.	Lorentzon, J., Järvstråt, N., and Josefson, B. L., 2009, "Modelling chip formation of alloy 718," Journal of Materials Processing Technology, 209 (10), pp. 4645-4653. DOI: <u>10.1016/j.jmatprotec.2008.11.029</u>

2203 2204 2205	148.	Sievert, R., Hamann, A. H., Noack, D., Löwe, P., Singh, K. N., and Künecke, G., 2005, "Simulation of thermal softening, damage and chip segmentation in a nickel superalloy," Hochgeschwindigkeitspannen, 8 , pp. 446-469. DOI:
2206 2207 2208	149.	Prete, A. D., Filice, L., and Umbrello, D., 2013, "Numerical Simulation of Machining Nickel-Based Alloys," Procedia CIRP, 8 , pp. 540-545. DOI: 10.1016/j.procir.2013.06.147
2209 2210 2211	150.	Uhlmann, E., Schulenburg, M. G. v. d., and Zettier, R., 2007, "Finite Element Modeling and Cutting Simulation of Inconel 718," CIRP Annals, 56 (1), pp. 61-64. DOI: 10.1016/j.cirp.2007.05.017
2212 2213 2214 2215 2216	151.	Sievert, R., Noack, HD., Hamann, A., Löwe, P., Singh, K. N., Künecke, G., Clos, R., Schreppel, U., Veit, P., Uhlmann, E., and Zettier, R., 2003, "Simulation der Spansegmentierung beim Hochgeschwindigkeits-zerspanen unter Berücksichtigung duktiler Schädigung," Technische Mechanik - European Journal of Engineering Mechanics, 23 (2-4), pp. 216-233. DOI:
2217 2218 2219 2220	152.	Olschewski, J., Hamann, A., and Noack, H. D., "Werkstoffmechanik einer Nickelbasislegierung beim Hochgeschwindigkeitsspanen-Werkstoffverhalten und Modellierung, Teil III. Report BAM-V. 2 01/6," Bundesanstalt für Materialforschung Und-prüfung. DOI:
2221 2222 2223 2224	153.	Mitrofanov, A. V., Babitsky, V. I., and Silberschmidt, V. V., 2005, "Thermomechanical finite element simulations of ultrasonically assisted turning," Computational Materials Science, 32 (3-4), pp. 463-471. DOI: 10.1016/j.commatsci.2004.09.019
2225 2226 2227	154.	Klocke, F., Lung, D., and Buchkremer, S., 2013, "Inverse Identification of the Constitutive Equation of Inconel 718 and AISI 1045 from FE Machining Simulations," Procedia CIRP, 8 , pp. 212-217. DOI: 10.1016/j.procir.2013.06.091
2228 2229 2230	155.	Puls, H., Klocke, F., and Lung, D., 2012, "A new experimental methodology to analyse the friction behaviour at the tool-chip interface in metal cutting," Production Engineering, 6 (4-5), pp. 349-354. DOI: <u>10.1007/s11740-012-0386-6</u>
2231 2232	156.	Mahalle, G., Kotkunde, N., Gupta, A. K., Sujith, R., Singh, S. K., and Lin, Y. C., 2019, "Microstructure Characteristics and Comparative Analysis of Constitutive Models

2233 2234		for Flow Stress Prediction of Inconel 718 Alloy," Journal of Materials Engineering and Performance, 28 (6), pp. 3320-3331. DOI: <u>10.1007/s11665-019-04116-w</u>
2235 2236 2237 2238	157.	Grzesik, W., Niesłony, P., and Laskowski, P., 2017, "Determination of Material Constitutive Laws for Inconel 718 Superalloy Under Different Strain Rates and Working Temperatures," Journal of Materials Engineering and Performance, 26 (12), pp. 5705-5714. DOI: 10.1007/s11665-017-3017-8
2239 2240 2241 2242	158.	Qiu, X., Cheng, X., Dong, P., Peng, H., Xing, Y., and Zhou, X., 2019, "Sensitivity Analysis of Johnson-Cook Material Constants and Friction Coefficient Influence on Finite Element Simulation of Turning Inconel 718," Materials, 12 (19), pp. 3121. DOI: <u>10.3390/ma12193121</u>
2243 2244 2245	159.	Jafarian, F., 2019, "3D modeling of recrystallized layer depth and residual stress in dry machining of nickel-based alloy," Journal of the Brazilian Society of Mechanical Sciences and Engineering, 41 (4), pp. 1-10. DOI: 10.1007/s40430-019-1707-x
2246 2247 2248 2249	160.	Zhu, Q., Chen, L., Chen, G., Wang, C., Qin, H., and Zhang, P., 2022, "A Two-Stage Constitutive Model and Microstructure Evolution Simulation of a Nickel-Based Superalloy during High Temperature Deformation," Journal of Materials Engineering and Performance, pp. 1-12. DOI: 10.1007/s11665-022-07347-6
2250 2251 2252 2253	161.	Thimm, B., Steden, J., Reuber, M., and Christ, HJ., 2019, "Using Digital Image Correlation Measurements for the Inverse Identification of Constitutive Material Parameters applied in Metal Cutting Simulations," Procedia CIRP, 82 , pp. 95-100. DOI: 10.1016/j.procir.2019.04.156
2254 2255 2256 2257	162.	Demir, E. and Mercan, C., 2018, "A physics-based single crystal plasticity model for crystal orientation and length scale dependence of machining response," International Journal of Machine Tools and Manufacture, 134 , pp. 25-41. DOI: 10.1016/j.ijmachtools.2018.06.004
2258 2259 2260 2261	163.	Rinaldi, S., Umbrello, D., Rotella, G., and Del Prete, A., 2020, "A Physically Based Model to Predict Microstructural Modifications in Inconel 718 High Speed Machining," Procedia Manufacturing, 47 , pp. 487-492. DOI: 10.1016/j.promfg.2020.04.344
2262 2263	164.	Guan, Q., Lu, S., Lu, Y., and Li, J., 2022, "Study on the modified power-law constitutive model for the FEM cutting simulation of Inconel 625 deposited metal

2264 2265		using the electroslag welding process," Journal of Manufacturing Processes, 81 , pp. 881-892. DOI: 10.1016/j.jmapro.2022.07.042
2266 2267 2268	165.	Merchant, M. E., 1945, "Mechanics of the Metal Cutting Process. I. Orthogonal Cutting and a Type 2 Chip," Journal of Applied Physics, 16 (5), pp. 267-275. DOI: 10.1063/1.1707586
2269 2270 2271	166.	Oxley, P. L. B. and Shaw, M. C., 1990, "Mechanics of Machining: An Analytical Approach to Assessing Machinability," Journal of Applied Mechanics. DOI: 10.1115/1.2888318
2272 2273 2274 2275	167.	Samantaray, D., Mandal, S., Borah, U., Bhaduri, A. K., and Sivaprasad, P. V., 2009, "A thermo-viscoplastic constitutive model to predict elevated-temperature flow behaviour in a titanium-modified austenitic stainless steel," Materials Science and Engineering: A, 526 (1-2), pp. 1-6. DOI: <u>10.1016/j.msea.2009.08.009</u>
2276 2277 2278 2279 2280	168.	Liu, Y., Li, M., Ren, Xw., Xiao, Zb., Zhang, Xy., and Huang, Yc., 2020, "Flow stress prediction of Hastelloy C-276 alloy using modified Zerilli–Armstrong, Johnson–Cook and Arrhenius-type constitutive models," Transactions of Nonferrous Metals Society of China, 30 (11), pp. 3031-3042. DOI: 10.1016/S1003-6326(20)65440-1
2281 2282 2283	169.	Follansbee, P. and Kocks, U., 1988, "A constitutive description of the deformation of copper based on the use of the mechanical threshold stress as an internal state variable," Acta Metallurgica, 36 (1), pp. 81-93. DOI:
2284 2285 2286 2287	170.	Feng, Y., Mandal, S., Gockel, B., and Rollett, A. D., 2017, "Extension of the Mechanical Threshold Stress Model to Static and Dynamic Strain Aging: Application to AA5754-O," Metallurgical and Materials Transactions A, 48 (11), pp. 5591-5607. DOI: 10.1007/s11661-017-4276-6
2288 2289 2290	171.	Follansbee, P. S., 2022, "Application of the Mechanical Threshold Stress Model to Large Strain Processing," Materials Sciences and Applications, 13 (5), pp. 300-316. DOI: <u>10.4236/msa.2022.135016</u>
2291 2292 2293 2294	172.	Liu, R., Salahshoor, M., Melkote, S., and Marusich, T., 2015, "A unified material model including dislocation drag and its application to simulation of orthogonal cutting of OFHC Copper," Journal of Materials Processing Technology, 216 , pp. 328-338. DOI: 10.1016/j.jmatprotec.2014.09.021

2295 2296 2297 2298	173.	Rinaldi, S., Umbrello, D., and Melkote, S. N., 2021, "Modelling the effects of twinning and dislocation induced strengthening in orthogonal micro and macro cutting of commercially pure titanium," International Journal of Mechanical Sciences, 190 , pp. 106045. DOI: 10.1016/j.ijmecsci.2020.106045
2299 2300 2301 2302	174.	Atmani, Z., Haddag, B., Nouari, M., and Zenasni, M., 2016, "Combined microstructure-based flow stress and grain size evolution models for multi-physics modelling of metal machining," International Journal of Mechanical Sciences, 118 , pp. 77-90. DOI: 10.1016/j.ijmecsci.2016.09.016
2303 2304 2305	175.	Estrin, Y., Toth, L. S., Molinari, A., and Bréchet, Y., 1998, "A dislocation-based model for all hardening stages in large strain deformation," Acta Materialia, 46 (15), pp. 5509-5522. DOI: <u>10.1016/S1359-6454(98)00196-7</u>
2306 2307 2308	176.	Komanduri, R. and Hou, ZB., 2002, "On thermoplastic shear instability in the machining of a titanium alloy (Ti-6Al-4V)," Metallurgical and Materials Transactions A, 33 (9), pp. 2995-3010. DOI: <u>10.1007/s11661-002-0284-1</u>
2309 2310 2311 2312	177.	Sima, M. and Özel, T., 2010, "Modified material constitutive models for serrated chip formation simulations and experimental validation in machining of titanium alloy Ti–6Al–4V," International Journal of Machine Tools and Manufacture, 50 (11), pp. 943-960. DOI:
2313 2314 2315 2316	178.	Menezes, P. L., Avdeev, I. V., Lovell, M. R., and Higgs III, C. F., 2014, "An explicit finite element model to study the influence of rake angle and friction during orthogonal metal cutting," The International Journal of Advanced Manufacturing Technology, 73 (5), pp. 875-885. DOI: <u>10.1007/s00170-014-5877-5</u>
2317 2318 2319 2320	179.	Daoud, M., Jomaa, W., Chatelain, J. F., and Bouzid, A., 2015, "A machining-based methodology to identify material constitutive law for finite element simulation," The International Journal of Advanced Manufacturing Technology, 77 (9), pp. 2019-2033. DOI: 10.1007/s00170-014-6583-z
2321 2322 2323 2324 2325	180.	Shi, B., Attia, H., and Tounsi, N., 2010, "Identification of Material Constitutive Laws for Machining—Part I: An Analytical Model Describing the Stress, Strain, Strain Rate, and Temperature Fields in the Primary Shear Zone in Orthogonal Metal Cutting," Journal of Manufacturing Science and Engineering, 132 (5), pp. 051008. DOI: 10.1115/1.4002454

2326 2327 2328 2329 2330	181.	Daoud, M., Chatelain, J. F., and Bouzid, A., 2015, "Effect of rake angle on Johnson-Cook material constants and their impact on cutting process parameters of Al2024-T3 alloy machining simulation," The International Journal of Advanced Manufacturing Technology, 81 (9), pp. 1987-1997. DOI: 10.1007/s00170-015-7179
2331 2332 2333	182.	Li, J. L., Liu, G., Zhang, D. J., and Chen, M. W., 2008," A FEM study on chip formation in orthogonal turning Nickel-based superalloy GH80A," <i>Proc.</i> Materials Science Forum,eds.,575, pp. 1370-1375.
2334 2335 2336	183.	Bäker, M., 2006, "Finite element simulation of high-speed cutting forces," Journal of Materials Processing Technology, 176 (1-3), pp. 117-126. DOI: 10.1016/j.jmatprotec.2006.02.019
2337 2338 2339 2340 2341	184.	Jomaa, W., Daoud, M., Songmene, V., Bocher, P., and Châtelain, JF., 2014," Identification and Validation of Marusich's Constitutive Law for Finite Element Modeling of High Speed Machining," <i>Proc.</i> ASME International Mechanical Engineering Congress and Exposition,eds., Montreal, Quebec, Canada,46438, pp. V02AT02A057.
2342 2343 2344 2345	185.	Zhang, D., Zhang, XM., and Ding, H., 2018, "Inverse identification of material plastic constitutive parameters based on the DIC determined workpiece deformation fields in orthogonal cutting," Procedia CIRP, 71 , pp. 134-139. DOI: 10.1016/j.procir.2018.05.085
2346 2347 2348 2349	186.	Majumdar, P., Jayaramachandran, R., and Ganesan, S., 2005, "Finite element analysis of temperature rise in metal cutting processes," Applied Thermal Engineering, 25 (14-15), pp. 2152-2168. DOI: 10.1016/j.applthermaleng.2005.01.006
2350 2351 2352 2353	187.	Özel, T. and Zeren, E., 2007, "Finite element modeling the influence of edge roundness on the stress and temperature fields induced by high-speed machining," The International Journal of Advanced Manufacturing Technology, 35 (3), pp. 255-267. DOI: <u>10.1007/s00170-006-0720-2</u>
2354 2355 2356 2357	188.	Al-Zkeri, I., Rech, J., Altan, T., Hamdi, H., and Valiorgue, F., 2009, "OPTIMIZATION OF THE CUTTING EDGE GEOMETRY OF COATED CARBIDE TOOLS IN DRY TURNING OF STEELS USING A FINITE ELEMENT ANALYSIS," Machining Science and Technology, 13 (1), pp. 36-51. DOI: <u>10.1080/10910340902776051</u>

2358 2359 2360 2361	189.	Ucun, İ. and Aslantas, K., 2011, "Numerical simulation of orthogonal machining process using multilayer and single-layer coated tools," The International Journal of Advanced Manufacturing Technology, 54 (9), pp. 899-910. DOI: <u>10.1007/s00170-010-3012-9</u>
2362 2363 2364	190.	Yen, YC., Jain, A., Chigurupati, P., Wu, WT., and Altan, T., 2004, "Computer Simulation of Orthogonal Cutting Using a Tool with Multiple Coatings," Machining Science and Technology, 8 (2), pp. 305-326. DOI: <u>10.1081/MST-200029230</u>
2365 2366 2367 2368	191.	Yuan, K., Guo, W., Li, D., Li, P., Zhang, Y., and Wang, P., 2021, "Influence of heat treatments on plastic flow of laser deposited Inconel 718: Testing and microstructural based constitutive modeling," International Journal of Plasticity, 136 , pp. 102865. DOI: 10.1016/j.ijplas.2020.102865
2369 2370 2371 2372 2373	192.	Ghorbanpour, S., Zecevic, M., Kumar, A., Jahedi, M., Bicknell, J., Jorgensen, L., Beyerlein, I. J., and Knezevic, M., 2017, "A crystal plasticity model incorporating the effects of precipitates in superalloys: Application to tensile, compressive, and cyclic deformation of Inconel 718," International Journal of Plasticity, 99 , pp. 162-185. DOI: 10.1016/j.ijplas.2017.09.006
2374 2375 2376	193.	Tan, Y. B., Ma, Y. H., and Zhao, F., 2018, "Hot deformation behavior and constitutive modeling of fine grained Inconel 718 superalloy," Journal of Alloys and Compounds, 741 , pp. 85-96. DOI: <u>10.1016/j.jallcom.2017.12.265</u>
2377 2378 2379 2380	194.	Voyiadjis, G. Z. and Song, Y., 2020, "A physically based constitutive model for dynamic strain aging in Inconel 718 alloy at a wide range of temperatures and strain rates," Acta Mechanica, 231 (1), pp. 19-34. DOI: <u>10.1007/s00707-019-02508-6</u>
2381 2382	195.	Springer Handbook of Experimental Solid Mechanics, 2008, Springer Science & Business Media. ISBN: 0387268839
2383 2384 2385 2386	196.	Osorio-Pinzon, J. C., Abolghasem, S., and Casas-Rodriguez, J. P., 2019, "Predicting the Johnson Cook constitutive model constants using temperature rise distribution in plane strain machining," The International Journal of Advanced Manufacturing Technology, 105 (1), pp. 279-294. DOI: <u>10.1007/s00170-019-04225-9</u>
2387 2388	197.	Jomaa, W., Songmene, V., and Bocher, P., 2016, "An hybrid approach based on machining and dynamic tests data for the identification of material constitutive

2389 2390		equations," Journal of Materials Engineering and Performance, 25 (3), pp. 1010-1027. DOI: 10.1007/s11665-016-1950-6
2391 2392 2393 2394	198.	Zouabi, H., Calamaz, M., Wagner, V., Cahuc, O., and Dessein, G., 2021, "Kinematic Fields Measurement during Orthogonal Cutting Using Digital Images Correlation: A Review," Journal of Manufacturing and Materials Processing, 5 (1), pp. 7. DOI: 10.3390/jmmp5010007
2395 2396 2397	199.	Waldorf, D. J., DeVor, R. E., and Kapoor, S. G., 1999, "An evaluation of ploughing models for orthogonal machining," Journal of Manufacturing Science and Engineering, Transactions of the ASME, 121 (4), pp. 550-558. DOI:
2398 2399 2400	200.	Oxley, P. L. B. and Welsh, M. J. M., 1964, "Calculating the shear angle in orthogonal metal cutting from fundamental stress-strain-strain rate properties of the work material." DOI:
2401 2402 2403 2404 2405	201.	Oxley, P. and Hastings, W., 1977, "Predicting the strain rate in the zone of intense shear in which the chip is formed in machining from the dynamic flow stress properties of the work material and the cutting conditions," Proceedings of the Royal Society of London. A. Mathematical and Physical Sciences, 356 (1686), pp. 395-410. DOI:
2406 2407 2408	202.	Loewen, E. G. and Shaw, M. C., 1954, "On the Analysis of Cutting-Tool Temperatures," Transactions of the American Society of Mechanical Engineers, 76 (2), pp. 217-225. DOI: <u>10.1115/1.4014799</u>
2409 2410 2411	203.	Rai, A. K., Trpathy, H., Hajra, R. N., Raju, S., and Saroja, S., 2017, "Thermophysical properties of Ni based super alloy 617," Journal of Alloys and Compounds, 698 , pp. 442-450. DOI: 10.1016/j.jallcom.2016.12.183
2412 2413 2414	204.	Abdel-Aal, H. A., Nouari, M., and Mansori, M. E., 2009, "Influence of thermal conductivity on wear when machining titanium alloys," Tribology International, 42 (2), pp. 359-372. DOI: <u>10.1016/j.triboint.2008.07.005</u>
2415 2416 2417	205.	Louzguine-Luzgin, D. V., Setyawan, A. D., Kato, H., and Inoue, A., 2006, "Influence of thermal conductivity on the glass-forming ability of Ni-based and Cu-based alloys," Applied Physics Letters, 88 (25), pp. 251902. DOI: <u>10.1063/1.2213967</u>

2418 20 2419 2420	 Special Metals INCONEL® Alloy 718. 2021, MatWeb, LLC.: http://www.matweb.com/search/DataSheet.aspx?MatGUID=94950a2d209040a09 <u>b89952d45086134</u>.
2421 20 2422 2423	7. Special Metals INCONEL® Alloy 600. 2021, MatWeb, LLC.: http://www.matweb.com/search/datasheet.aspx?matguid=029d44b293ee41a1926d8de74e6369bc .
2424 20 2425 2426	8. Special Metals MONEL® Alloy K-500. 2021, MatWeb: https://www.matweb.com/search/DataSheet.aspx?MatGUID=13ef71e975a046628e1d033bb17b377c&ckck=1 .
2427 20 2428	9. Data Sheet - René 41. 2011, Rolled Alloys: https://www.rolledalloys.com/shared-content/technical-resources/datasheets/RENE-41 DS US EN.pdf.
2429 21 2430	0. INCONEL 600 TECHNICAL DATA. 2015, High Temp Metals: https://www.hightempmetals.com/techdata/hitempInconel600data.php .
2431 21 2432 2433 2434	 Haynes Hastelloy® B-2 alloy, 6.4 mm thick, as manual gas tungsten arc welded. 2021, MatWeb, LLC.: http://www.matweb.com/search/DataSheet.aspx?MatGUID=6d126a1c146f4063b c0ed82523d4cae3.
2435 21 2436 2437	 MONEL® alloy 400. 2005, Special Metals Corporation: https://www.specialmetals.com/documents/technical-bulletins/monel-alloy-400.pdf.
2438 21 2439 2440	3. Roy, R., Agrawal, D. K., and McKinstry, H. A., 1989, "VERY LOW THERMAL EXPANSION COEFFICIENT MATERIALS," Annual Review of Materials Science, 19 (1), pp. 59-81. DOI: 10.1146/annurev.ms.19.080189.000423
2441 21 2442 2443 2444	 Jablonski, P. D. and Alman, D. E., 2007, "Oxidation resistance and mechanical properties of experimental low coefficient of thermal expansion (CTE) Ni-base alloys," International Journal of Hydrogen Energy, 32(16), pp. 3705-3712. DOI: 10.1016/j.ijhydene.2006.08.019

2445 2446 2447	215.	Monroe, J. A., Gehring, D., Karaman, I., Arroyave, R., Brown, D. W., and Clausen, B., 2016, "Tailored thermal expansion alloys," Acta Materialia, 102 , pp. 333-341. DOI: <u>10.1016/j.actamat.2015.09.012</u>
2448 2449 2450 2451	216.	Karunaratne, M. S. A., Kyaw, S., Jones, A., Morrell, R., and Thomson, R. C., 2016, "Modelling the coefficient of thermal expansion in Ni-based superalloys and bond coatings," Journal of Materials Science, 51 (9), pp. 4213-4226. DOI: 10.1007/s10853-015-9554-3
2452	217.	Valencia, J. J. and Quested, P. N., Thermophysical Properties. 2013.
2453 2454	218.	Salazar, A., 2003, "On thermal diffusivity," European Journal of Physics, 24 (4), pp. 351. DOI: <u>10.1088/0143-0807/24/4/353</u>
2455 2456 2457	219.	Parker, W. J., Jenkins, R. J., Butler, C. P., and Abbott, G. L., 1961, "Flash Method of Determining Thermal Diffusivity, Heat Capacity, and Thermal Conductivity," Journal of Applied Physics, 32 (9), pp. 1679-1684. DOI: 10.1063/1.1728417
2458 2459 2460 2461	220.	Arunachalam, R. M., Mannan, M. A., and Spowage, A. C., 2004, "Residual stress and surface roughness when facing age hardened Inconel 718 with CBN and ceramic cutting tools," International Journal of Machine Tools and Manufacture, 44 (9), pp. 879-887. DOI: <u>10.1016/j.ijmachtools.2004.02.016</u>
2462 2463 2464	221.	Salazar, A., Sánchez-Lavega, A., and Fernandez, J., 1989, "Theory of thermal diffusivity determination by the "mirage" technique in solids," Journal of Applied Physics, 65 (11), pp. 4150-4156. DOI: <u>10.1063/1.343320</u>
2465 2466 2467	222.	Arrazola, P. J. and Özel, T., 2009, "Finite Element Modelling of Machining Processes," Intelligent Machining: Modelling and Optimization of the Machining Processes and Systems. DOI:
2468 2469 2470 2471	223.	Dudzinski, D., Devillez, A., Moufki, A., Larrouquere, D., Zerrouki, V., and Vigneau, J., 2004, "A review of developments towards dry and high speed machining of Inconel 718 alloy," International Journal of Machine Tools and Manufacture, 44 (4), pp. 439-456. DOI:
2472 2473	224.	Nieslony, P., Grzesik, W., Laskowski, P., and Habrat, W., 2013, "FEM-Based Modelling of the Influence of Thermophysical Properties of Work and Cutting Tool

2474 2475		Materials on the Process Performance," Procedia CIRP, 8 , pp. 3-8. DOI: 10.1016/j.procir.2013.06.056
2476 2477	225.	Kalhori, V., Modelling and Simulation of Mechanical Cutting, in Department of Mechanical Engineering. 2001, Luleå Tekniska Universitet. pp. 103.
2478 2479 2480 2481	226.	Hariharan, V. S., Pramod, S., Kesavan, D., Murty, B. S., and Phanikumar, G., 2022, "ICME framework to simulate microstructure evolution during laser powder bed fusion of Haynes 282 nickel-based superalloy," Journal of Materials Science, 57 , pp. 9693-9713. DOI: 10.1007/s10853-022-07170-3
2482 2483 2484	227.	Schoop, J., 2021, "In-Situ Calibrated Modeling of Residual Stresses Induced in Machining under Various Cooling and Lubricating Environments," Lubricants, 9 (3), pp. 28. DOI: 10.3390/lubricants9030028
2485 2486 2487 2488	228.	Schoop, J., Adeniji, D., and Brown, I., 2019, "Computationally efficient, multidomain hybrid modeling of surface integrity in machining and related thermomechanical finishing processes," Procedia CIRP, 82 , pp. 356-361. DOI: 10.1016/j.procir.2019.03.225
2489 2490 2491 2492	229.	Binoj, J. S., Manikandan, N., Thejasree, P., Varaprasad, K. C., Sai, N. P., and Manideep, M., 2021, "Machinability studies on wire electrical discharge machining of Nickel alloys using multiple regression analysis," Materials Today: Proceedings, 39 , pp. 155-159. DOI: 10.1016/j.matpr.2020.06.407
2493 2494 2495	230.	Salcedo, A. T., Arbizu, I. P., and Pérez, C. J. L., 2017, "Analytical Modelling of Energy Density and Optimization of the EDM Machining Parameters of Inconel 600," Metals, 7 (5), pp. 166. DOI: <u>10.3390/met7050166</u>
2496 2497 2498 2499	231.	Dinda, G. P., Dasgupta, A. K., and Mazumder, J., 2009, "Laser aided direct metal deposition of Inconel 625 superalloy: Microstructural evolution and thermal stability," Materials Science and Engineering: A, 509 (1-2), pp. 98-104. DOI: 10.1016/j.msea.2009.01.009
2500 2501 2502 2503	232.	Al-Fadhli, H. Y., Stokes, J., Hashmi, M. S. J., and Yilbas, B. S., 2006, "The erosion—corrosion behaviour of high velocity oxy-fuel (HVOF) thermally sprayed inconel-625 coatings on different metallic surfaces," Surface and Coatings Technology, 200 (20-21), pp. 5782-5788. DOI: <u>10.1016/j.surfcoat.2005.08.143</u>

2504 2505	233.	INCONEL 625 TECHNICAL DATA. 2015, High Temp Metals: https://www.hightempmetals.com/techdata/hitemplnconel625data.php .
2506 2507 2508	234.	Thomas, A., El-Wahabi, M., Cabrera, J. M., and Prado, J. M., 2006, "High temperature deformation of Inconel 718," Journal of Materials Processing Technology, 177 (1-3), pp. 469-472. DOI: <u>10.1016/j.imatprotec.2006.04.072</u>
2509 2510 2511	235.	Ono, Y., Yuri, T., Sumiyoshi, H., Takeuchi, E., Matsuoka, S., and Ogata, T., 2004, "High-cycle fatigue properties at cryogenic temperatures in Inconel 718 nickel-based superalloy," Materials Transactions, 45 (2), pp. 342-345. DOI:
2512 2513 2514 2515 2516	236.	Ramkumar, K. D., Abraham, W. S., Viyash, V., Arivazhagan, N., and Rabel, A. M., 2017, "Investigations on the microstructure, tensile strength and high temperature corrosion behaviour of Inconel 625 and Inconel 718 dissimilar joints," Journal of Manufacturing Processes, 25 , pp. 306-322. DOI: 10.1016/j.jmapro.2016.12.018
2517 2518 2519	237.	Rahman, M., Seah, W. K. H., and Teo, T. T., 1997, "The machinability of Inconel 718," Journal of Materials Processing Technology, 63 (1-3), pp. 199-204. DOI: 10.1016/S0924-0136(96)02624-6
2520 2521 2522	238.	Devillez, A., Schneider, F., Dominiak, S., Dudzinski, D., and Larrouquere, D., 2007, "Cutting forces and wear in dry machining of Inconel 718 with coated carbide tools," Wear, 262 (7-8), pp. 931-942. DOI: <u>10.1016/j.wear.2006.10.009</u>
2523 2524	239.	INCONEL 718 TECHNICAL DATA. 2015, High Temp Metals: https://www.hightempmetals.com/techdata/hitemplnconel718data.php .
2525 2526	240.	Aytekin, H. and Akcin, Y., 2013, "Characterization of borided Incoloy 825 alloy," Materials & Design, 50 , pp. 515-521. DOI: <u>10.1016/j.matdes.2013.03.015</u>
2527 2528 2529 2530 2531	241.	Kangazian, J. and Shamanian, M., 2019, "Microstructure and mechanical characterization of Incoloy 825 Ni-based alloy welded to 2507 super duplex stainless steel through dissimilar friction stir welding," Transactions of Nonferrous Metals Society of China, 29 (8), pp. 1677-1688. DOI: <u>10.1016/S1003-6326(19)65074-0</u>

2532 2533 2534 2535	242.	Bellezze, T., Roventi, G., and Fratesi, R., 2004, "Electrochemical characterization of three corrosion-resistant alloys after processing for heating-element sheathing," Electrochimica Acta, 49 (17-18), pp. 3005-3014. DOI: 10.1016/j.electacta.2004.01.060
2536 2537	243.	ALLOY 825 TECHNICAL DATA. 2015, High Temp Metals: https://www.hightempmetals.com/techdata/hitempIncoloy825data.php .
2538 2539 2540 2541	244.	Gangloff, R. P., Ha, H. M., Burns, J. T., and Scully, J. R., 2014, "Measurement and Modeling of Hydrogen Environment-Assisted Cracking in Monel K-500," Metallurgical and Materials Transactions A, 45 (9), pp. 3814-3834. DOI: 10.1007/s11661-014-2324-z
2542 2543 2544 2545 2546	245.	Scully, J. R., Gangloff, R. P., and Moreno, F. P., Mechanism-Based Modeling of Hydrogen Environment Assisted Cracking (HEAC) in High Strength Alloys for Marine Applications: Prediction of Monel K-500 HEAC for Select Environmental and Mechanical Conditions. 2012, Virginia University Charottesville Department of Materials Science and Engineering. pp. 142.
2547 2548 2549 2550	246.	Zahrani, E. G. and Sedghi, A., 2014, "Experimental investigation of precision turning of Monel K-500 under dry conditions," The International Journal of Advanced Manufacturing Technology, 73 (9), pp. 1265-1272. DOI: 10.1007/s00170-014-5911-7
2551 2552 2553 2554	247.	Atabay, S. E., Sanchez-Mata, O., Muñiz-Lerma, J. A., Gauvin, R., and Brochu, M., 2020, "Microstructure and mechanical properties of rene 41 alloy manufactured by laser powder bed fusion," Materials Science and Engineering: A, 773 , pp. 138849. DOI: 10.1016/j.msea.2019.138849
2555 2556 2557 2558	248.	Kayacan, R., Varol, R., and Kimilli, O., 2004, "The effects of pre- and post-weld heat treatment variables on the strain-age cracking in welded Rene 41 components," Materials Research Bulletin, 39 (14-15), pp. 2171-2186. DOI: 10.1016/j.materresbull.2004.08.003
2559 2560 2561	249.	Hack, H. P., Mechanical, Corrosion, and Fatigue Properties of 15-5 PH, Inconel 718, and Rene 41 Weldments. 1975, David W. Taylor Naval Ship Research and Development Center. pp. 44.

2562 2563 2564 2565	250.	Maurer, J. J., Mallett, J. J., Hudson, J. L., Fick, S. E., Moffat, T. P., and Shaw, G. A., 2010, "Electrochemical micromachining of Hastelloy B-2 with ultrashort voltage pulses," Electrochimica Acta, 55 (3), pp. 952-958. DOI: 10.1016/j.electacta.2009.09.004
2566 2567 2568	251.	Brooks, C. R. and Wang, Y. M., 1990, "Tensile properties and fractography of aged hastelloy B2 (550–850° C for up to 1200 H)," Materials Characterization, 25 (2), pp. 185-197. DOI: 10.1016/1044-5803(90)90009-9
2569 2570 2571 2572	252.	Chen, J., Zhou, X., Wang, W., Liu, B., Lv, Y., Yang, W., Xu, D., and Liu, Y., 2018, "A review on fundamental of high entropy alloys with promising high—temperature properties," Journal of Alloys and Compounds, 760 , pp. 15-30. DOI: 10.1016/j.jallcom.2018.05.067
2573 2574 2575	253.	Cao, S., Brooks, C. R., and Whittaker, G., 1994, "The structure of the heat-affected zone in welds of a Ni-29 wt.% Mo commercial alloy (Hastelloy B2)," Materials Characterization, 33 (1), pp. 21-32. DOI: <u>10.1016/1044-5803(94)90054-X</u>
2576 2577	254.	HASTELLOY® B-2 ALLOY. 1997, Haynes International, Inc.: http://specialmetals.ir/images/technical info/nickel%20base/hastelloy%20B2.pdf.
2578 2579 2580 2581 2582	255.	Manoj, I. V., Joy, R., Narendranath, S., and Nedelcu, D., 2019," Investigation of machining parameters on corner accuracies for slant type taper triangle shaped profiles using WEDM on Hastelloy X," <i>Proc.</i> Modern Technologies in Industrial Engineering VII (ModTech2019),Ravale, H. K. e. a., eds., lasi, Romania,591, pp. 012022.
2583 2584 2585 2586 2587	256.	Swaminathan, B., Lambros, J., and Sehitoglu, H., 2014, "Digital image correlation study of mechanical response of nickel superalloy Hastelloy X under thermal and mechanical cycling: Uniaxial and biaxial stress states," The Journal of Strain Analysis for Engineering Design, 49 (4), pp. 233-243. DOI: 10.1177/0309324713503959
2588 2589 2590 2591	257.	Sathishkumar, M. and Manikandan, M., 2020, "Development of Pulsed Current Arc Welding to Preclude Carbide Precipitates in Hastelloy X Weldment Using ERNiCr-3," Journal of Materials Engineering and Performance, 29 (8), pp. 5395-5408. DOI: 10.1007/s11665-020-05010-6

2592 2593	258.	HASTELLOY X TECHNICAL DATA. 2015, High Temp Metals: https://www.hightempmetals.com/techdata/hitempHastXdata.php .
2594 2595 2596 2597	259.	Yang, B., Shang, Z., Ding, J., Lopez, J., Jarosinski, W., Sun, T., Richter, N., Zhang, Y., Wang, H., and Zhang, X., 2022, "Investigation of strengthening mechanisms in an additively manufactured Haynes 230 alloy," Acta Materialia, 222 , pp. 117404. DOI 10.1016/j.actamat.2021.117404
2598 2599 2600 2601	260.	Haack, M., Kuczyk, M., Seidel, A., López, E., Brückner, F., and Leyens, C., 2020, "Investigation on the formation of grain boundary serrations in additively manufactured superalloy Haynes 230," Journal of Laser Applications, 32 (3), pp. 032014. DOI: 10.2351/7.0000112
2602 2603 2604 2605 2606	261.	Lu, Y. L., Chen, L. J., Wang, G. Y., Benson, M. L., Liaw, P. K., Thompson, S. A., Blust, J. W., Browning, P. F., Bhattacharya, A. K., Aurrecoechea, J. M., and Klarstrom, D. L., 2005, "Hold time effects on low cycle fatigue behavior of HAYNES 230® superalloy at high temperatures," Materials Science and Engineering: A, 409(1-2), pp. 282-291. DOI: 10.1016/j.msea.2005.05.120
2607 2608	262.	HAYNES 230 TECHNICAL DATA. 2015, High Temp Metals: https://www.hightempmetals.com/techdata/hitempHaynes230data.php .
2609 2610 2611 2612	263.	Zuo, Q., Liu, F., Wang, L., Chen, C., and Zhang, Z., 2015, "Prediction of hot deformation behavior in Ni-based alloy considering the effect of initial microstructure," Progress in Natural Science: Materials International, 25 (1), pp. 66-77. DOI: <u>10.1016/j.pnsc.2015.01.007</u>
2613 2614 2615	264.	Lin, Y. C., Chen, MS., and Zhong, J., 2008, "Prediction of 42CrMo steel flow stress at high temperature and strain rate," Mechanics Research Communications, 35 (3) pp. 142-150. DOI: 10.1016/j.mechrescom.2007.10.002
2616 2617 2618 2619	265.	Garofalo, F., 1965, "Fundamentals of creep and creep-rupture in metals (Creep and creep rupture in metals and alloys, fundamental information for instruction and reference)," NEW YORK, MACMILLAN CO., LONDON, COLLIER- MACMILLAN, LTD., 1965. 258 P. DOI:
2620 2621	266.	Zener, C. and Hollomon, J. H., 1944, "Effect of strain rate upon plastic flow of steel," Journal of Applied physics, 15 (1), pp. 22-32. DOI:

Journal of Manufacturing Science and Engineering

2622 2623 2624	267.	Agatonovic-Kustrin, S. and Beresford, R., 2000, "Basic concepts of artificial neural network (ANN) modeling and its application in pharmaceutical research," Journal of pharmaceutical and biomedical analysis, 22 (5), pp. 717-727. DOI:
2625	268.	Liu, J., Chang, H., Hsu, T. Y., and Ruan, X., 2000, "Prediction of the flow stress of
2626		high-speed steel during hot deformation using a BP artificial neural network,"
2627		Journal of Materials Processing Technology, 103 (2), pp. 200-205. DOI:
2628		<u>10.1016/S0924-0136(99)00444-6</u>
2629	269.	Amin, S., 2020, "Backpropagation–Artificial Neural Network (BP-ANN):
2630		Understanding gender characteristics of older driver accidents in West Midlands of
2631		United Kingdom," Safety science, 122 , pp. 104539. DOI:
2632		